Extending the application range of optical nanoscopy

Robin Diekmann

Dissertation

Extending the application range of optical nanoscopy

Robin Diekmann

October 2017

Biomolecular Photonics
Department of Physics
Bielefeld University

Referees:
Prof. Dr. Thomas Huser
Prof. Dr. Andreas Hütten

Printed on non-ageing paper °° ISO 9706

Summary

Fluorescence microscopy has established itself as a versatile tool in the life sciences. The spatial resolution of traditional light microscopes is restricted by the diffraction limit to about 200 nm but many subcellular structures are significantly smaller. Single molecule localization microscopy is one of the most widespread approaches to nanoscopy, allowing for imaging at superior resolution. This work demonstrates advances in this field, extending the range of applications by a considerable increase in throughput, super-resolution imaging of non-adherent samples, and cost-efficient setup designs.

The use of planar waveguides as sample substrates enables evanescent field excitation over large areas that are only limited by the waveguide layout. Accordingly, the excitation is decoupled from the imaging path and arbitrary objective lenses can be used. The use of conventional high numerical aperture and high magnification objective lenses in waveguide-based localization microscopy shows comparable performance to imaging on an established setup of inverted geometry, where a resolution of about 40 nm is obtained. Switching to a low numerical aperture and low magnification objective lens allows for imaging over a field-of-view of 0.5 mm $\times$ 0.5 mm where more than 50 cells can be simultaneously observed at a resolution better than 140 nm. Alternatively, images can be reconstructed at a resolution of approximately 150 nm from only about 200 raw frames recorded with a high numerical aperture objective lens. This is possible due to intrinsic multi-mode waveguide excitation patterns which induce fluctuations that are exploited for entropy-based super-resolution imaging. The combination of these approaches with diffraction limited fluorescence makes it possible to choose the tradeoff between spatial resolution and throughput in waveguide-based microscopy. Besides the experimental demonstration, modeling the relation between these two aspects confirms that different modalities yield the optimum resolution when the throughput is successively decreased. The according techniques range from diffraction limited imaging over fluctuation-based to localization-based super-resolution imaging at different numerical apertures and magnifications.

Nanoscopy of non-adherent cells becomes possible by the combination of an inverted widefield fluorescence microscope and holographic optical tweezers. These allow for holding objects at multiple points and in arbitrary orientations above the coverslip. Due to such immobilization of the samples, multiple thousand raw data frames can be recorded for *direct* stochastic optical reconstruction microscopy. The remaining position fluctuations owing to Brownian motion are compensated via deconvolution of the super-resolved images with an experimentally obtained position distribution function. This enables imaging of the chromosomal DNA in individual optically trapped bacteria at a resolution better than 100 nm. The optical tweezers introduce the flexibility to rotate the sample between multiple acquisition sequences, which is used for imaging the same sample from different directions. In this manner, information about the three-dimensional structure can be gathered at the isotropic uncompromised resolution of two-dimensional localization microscopy. Besides its application to nanoscopy, this setup is used to study the dynamic process of DNA-repair on a single-molecule level.

The use of industry-grade cameras instead of scientific-grade cameras can significantly reduce the cost of setups for high- and super-resolution microscopy. An industry-grade CMOS camera is characterized for its use in single emitter localization microscopy. The direct experimental comparison to a well-established scientific-grade CMOS camera shows a better localization precision for the latter, but no significant difference with respect to the resolution is observed for super-resolution imaging of the cytoskeleton in U2OS cells. Simulations considering the different camera properties confirm the difference in the localization precision and are furthermore used to demonstrate a simple approach to correct for pixel-to-pixel variations in terms of offset and gain. Additionally, the industry-grade CMOS camera is experimentally tested in typical imaging scenarios. Its maximum frame rate of up to 894 fps enables direct stochastic optical reconstruction microscopy at a resolution better than 40 nm from data recorded in 11.2 s or, alternatively, at a localization precision of about 3 nm. The low cost makes it economically viable to use two cameras for multi-color imaging in a custom-built setup. This microscope is applied to studying membrane fenestrations in liver sinusoidal endothelial cells.

Contents

1. Introduction

Fluorescence microscopy has evolved into one of the most powerful tools for the life sciences by its ability to selectively observe biomolecules of interest in their native environment [119]. Already the pioneer of light microscopy Ernst Abbe discovered that the wave-like property of light limits the obtainable resolution [1]. Accordingly, objects that are spaced by less than the diffraction limit of about 200 nm apart cannot be discerned by traditional light microscopes.

A majority of sub-cellular structures is considerably smaller than this scale, giving a strong motivation to enhance the resolution of fluorescence microscopy beyond the diffraction limit. This has led to the development of multiple concepts within the last decades and constituted the field of *super-resolution microscopy* [176], also termed optical *nanoscopy* [171]. One highlight in the history of this relatively young discipline was the 2014 Nobel prize in Chemistry being awarded to three of the main contributors.

Most methods developed so far make use of dynamics in the fluorescent signal, for instance generated by temporally varying illumination as in structured illumination microscopy (SIM) [80, 87], selective read-out using doughnut-shaped profiles as in stimulated emission depletion (STED) [88, 216], or stochastic photoswitching of fluorescent probes as in (fluorescent) photo-activated localization microscopy ((f)PALM) [17, 18, 92] and (*direct*) stochastic optical reconstruction microscopy ((*d*)STORM) [85, 168]. The combination of these three concepts has recently led to almost molecular resolution [13], a regime that was formerly reserved for microscopes which use particles of much smaller wavelengths such as electrons [163].

A big advantage of fluorescence microscopy over other techniques is its compatibility with physiological conditions, also enabling live-cell imaging [195]. Nevertheless, some approaches to super-resolution require extremely high light doses that can interfere notably with cellular processes or even lead to cell death [212]. Other approaches are more gentle in this aspect but are limited in their spatial or temporal resolution [157]. To answer specific biological questions, it is therefore necessary to choose the technique for the best trade-off between spatial resolution, temporal resolution and phototoxicity [171]. For instance, single molecule localiza-

tion microscopy (SMLM) relies on the localization of individual molecules at high spatial precision [45], but comes at the cost of rather long acquisition times. Hence, it is a good choice for structural imaging at resolutions as small as 20 nm [176], but usually an inferior choice for live-cell imaging at high temporal resolution and low phototoxicity. Spatial resolution, temporal resolution and phototoxicity belong to the major boundaries that researchers recently try to push by improving existing or developing new approaches to nanoscopy. Nevertheless, these are not the only relevant parameters that might lead to the preference of one technique over another, but others tend to be overlooked in the methods development.

One of such parameters is throughput [8], i.e. the number of samples that can be imaged per time, an aspect that is particularly important for techniques investigating fixed cells at high spatial resolution but long imaging times, such as SMLM. It is one topic of this thesis to investigate waveguide-chip based *d*STORM as an approach to high throughput SMLM. This is enabled by the unprecedented large field-of-view (FOV) offered by waveguide-based fluorescence excitation [3] in combination with low magnification objective lenses. Furthermore, it makes not only SMLM [85], but multiple approaches to high- and super-resolution [222] in one microscope possible, where the spatial resolution can be scaled approximately with the acquisition time. Thus, waveguide-based imaging potentially offers the flexibility to choose the required spatial resolution while benefiting from the highest possible throughput or temporal resolution.

Flexibility can also be highly desired with respect to the sample positioning. A majority of the approaches to SMLM feature an anisotropic spatial resolution that is worse in the direction of the optical axis [176], if no information about the third dimension at all [18, 92, 168]. Aligning the sample in a way that positions the structure of interest in the focal plane can be very helpful in gathering relevant information. Additionally, the long acquisition time in SMLM [121] puts high demands on the spatial stability and so far limits its application to samples mechanically attached to the coverslip. Overcoming both limitations of SMLM by its combination with steerable optical tweezers [67] is another topic of this thesis. The use of a spatial light modulator (SLM) [227] as a beam-shaping device in combination with optical trapping [78] allows for holding samples at multiple points above the coverslip and positioning them at will during the image acquisition [218].

Cost efficiency is a further aspect that can lead to the decision for a particular nanoscopy technique. It is therefore another topic of this thesis to evaluate cost-efficient solutions for SMLM. Its relatively low technical complexity has encouraged developments of entire cost-efficient setups before [96, 118, 131]. However,

the motivation of this work is primarily to characterize an industry-grade camera without further compromising the microscopes performance. A direct comparison to a scientific-grade device [99] of much higher cost allows for assessing its potential.

This work contributes to the flourishing field of nanoscopy with the focus on SMLM, especially *d*STORM. It aims at providing new insights, particularly related to the aspects of throughput, flexibility and cost-efficiency, and discusses the findings in the greater context of different approaches to high- and super-resolution microscopy.

After reviewing the relevant theoretical background in chapter 2, the chapters 3 to 5 present the results of this work with respect to waveguide-based nanoscopy, the combination of holographic optical trapping with *d*STORM, and cost-efficient solutions for SMLM. A comprehensive outlook is given in chapter 6.

2. Theoretical background

2.1. Widefield fluorescence microscopy

2.1.1. Fluorescence and phosphorescence

Fluorescence microscopy uses the specific labeling of biomolecules with fluorescent probes. By absorption of a photon, the quantum system of a fluorescent molecule is excited, whereby the photon energy is transferred as described by Planck's relation

$$E = h\nu = \frac{hc}{\lambda}, \tag{2.1}$$

where E is the energy, h is Planck's constant, c is the speed of light, ν is the photon frequency and λ is the photon wavelength in vacuum. While only higher electronic states may be occupied in atoms, rotational and vibrational states can also become excited in molecules due to the Franck-Condon principle [63, 36]. Their excitational energy usually dissipates quickly by non-radiative relaxation to the vibrational ground-state, leaving only an electronical excitation. From this state, the remaining energy can be released by transition back to the electronic ground-state under the emission of a photon. As the energy difference is lower than the energy of the originally absorbed photon, the emission wavelength is higher than the absorption wavelength due to the reciprocal relation between the photon energy and the wavelength in equation (2.1). This is known as the Stokes shift. [119]

These and further relevant processes are typically illustrated by the Jablonski diagram [108], as shown in Figure 2.1. By the absorption of a photon, the dye molecule is transferred from the ground-state S_0 to the first excited singlet state S_1 where vibrational relaxation takes place on short time-scales [119]. From there, the molecule can either be further excited or return to the singlet ground-state S_0 in a radiationless way via internal conversion. However, the commonly desired pathway is the fluorescent return to the ground-state under the emission of a red-shifted photon. The boxes represent the highest occupied molecular orbital

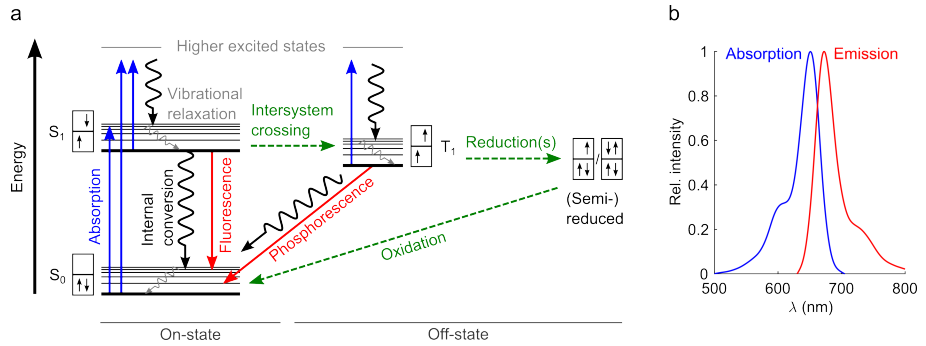

Figure 2.1.: a, The extended Jablonski diagram shows fluorescence, phosphorescence, and non-radiative pathways relevant for photoswitching of organic dyes. The boxes represent the HOMO and the LUMO orbitals and the arrows indicate the electron spin. **b**, The absorption and emission spectra of the organic dye Alexa 647 illustrate the Stokes shift, i.e. the shift to longer wavelengths between photon absorption and emission. Spectrum digitized from [199].

(HOMO) and the lowest unoccupied molecular orbital (LUMO) of the unexcited state and their electron configurations including the spin [173]. Accordingly, one electron is transferred from the HOMO to the LUMO and back during the cycle of photon absorption and emission.

The spin of one of the relevant electrons can flip when in the S_1 state, transferring the molecule to the triplet state T_1 which is a competing pathway to the fluorescence emission. Pauli's principle forbids the return of the excited electron to the HOMO which leads to a usually prolonged lifetime of this state in comparison to S_1. The return back to S_0 under photon emission is called phosphorescence.

2.1.2. Photoswitching of organic dyes

When viewed in the context of photoswitching of organic dyes, the Jablonski diagram can be extended to consider further processes [229]. For instance, rhodamines (e.g. the dyes Atto 488 and Alexa 488) and oxazines (e.g. Atto 655) [203] as well as cyanines [210] (e.g. Alexa 647) can be reduced from the triplet state in the presence of a thiol to form a longer lived state. As the molecule does not undergo fluorescence during this time, this can be interpreted as a dark off-state. Oxazines can be further reduced [203] and cyanines can form a longer lived dark state via the reversible adduction of a thiol [39]. However, these processes are reversible such that the dyes can return to the S_0 state and can again fluoresce.

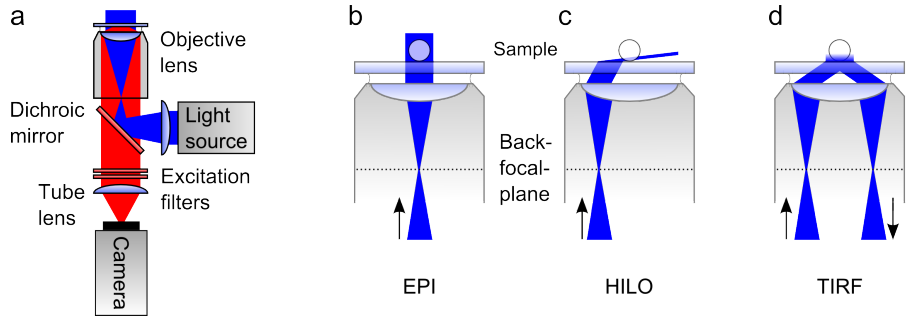

Figure 2.2.: **a**, Sketch of a common widefield fluorescence microscope. In epi-illumination, the excitation light (e.g. from a laser source) is supplied to the sample through the same objective lens that is used for fluorescence detection. A dichroic mirror allows for spectral separation of the excitation and emission light. The latter can be additionally filtered before reaching the camera detector to where it is focused via a tube lens. **b**, A collimated beam at the sample is used for widefield epi-illumination, **c**, while tilting the beam with respect to the coverslip interface results in HILO illumination of the sample. **d**, The angle is further increased for TIRF excitation where the intensity decays exponentially away from the coverslip.

The understanding of the transitions between the different states allows for controlling the dye behavior to some extend. For instance, the triplet state of Alexa 647 is quenched in the presence of cyclooctatetraene [147] which increases the apparent brightness. The competing pathway of reduction is influenced by the addition of reducing agents such as β-mercaptoethylamine (MEA) [84], β-mercaptoethanol (BME) [127] or ascorbic acid [209] to the imaging buffer. From the reduced state, molecules can be returned back to the S_0 state by the addition of an oxidizing agent such as methyl-viologen [209] or alternatively by the illumination with UV-light [204]. Molecular oxygen can interfere with many of these processes and can furthermore lead to permanent photodestruction of excited dyes, wherefore enzymatic oxygen removal is frequently used in imaging buffers [7, 57, 139].

2.1.3. Microscope setup

Due to the Stokes shift, excitation and emission light can be spectrally separated by the use of suitable filters. Together with the ability to attach fluorescent labels to targets of interest, e.g. proteins, DNA, or lipids, subcellular components can be specifically observed by the use of fluorescence microscopy.

A widefield fluorescence microscope typically features a light source that is matched to the absorption spectrum of the fluorescent probes or vice versa, one

or multiple filters to separate the excitation and the emission light, an infinity-corrected objective lens in combination with a tube lens, and a camera detector. Such a setup is depicted in Figure 2.2a.

2.1.4. Illumination schemes

Many fluorescence microscopes illuminate the sample through the objective lens that is also used for signal detection. However, this epi-illumination is not the only way of delivering the excitation to the sample. For instance, orthogonal illumination is supplied to selective planes in light-sheet microscopy [157].

Focusing the excitation beam to the center of the back-focal-plane of the objective lens results in a collimated excitation beam (Figure 2.2b). The excitation light propagates through the entire volume of the sample above and below the focus. The imaging depth is therefore not limited, but fluorescence is excited in this entire volume. This comes with the drawback of background fluorescence impairing the signal to background ratio and photobleaching in the whole volume.

Translating the focus of the excitation beam towards the edge of the objective back-focal-plane tilts the illumination at the sample. If the objective lens supports a sufficiently high angle of illumination, the excitation beam can be adjusted to form a highly inclined and laminated optical sheet (HILO) crossing the focal plane [201] (Figure 2.2c). This has the advantage that less fluorescence in planes above and below the focus is excited and, thus, achieving better signal to background ratios.

Tilting the angle of the illumination further enables total internal reflection fluorescence (TIRF) excitation [132] (Figure 2.2d). Coverslips supporting the sample are usually made from glass featuring a refractive index of about $n = 1.518$, while the refractive index of water is $n = 1.33$ and the refractive index of cellular samples is approximately $n = 1.4$ [23]. Total internal reflection occurs at the interface between the glass and the water or the sample when the angle of the illumination is adjusted equal to or higher than the critical angle

$$\theta_c = \arcsin\left(\frac{n_2}{n_1}\right), \tag{2.2}$$

where n_1 is the refractive index of the coverslip and n_2 is the refractive index of the sample or water, respectively.

However, the electromagnetic field is not completely stopped, but follows an exponential decay away from the interface. Accordingly, also the excitation inten-

sity I decays exponentially as

$$I(z) = I_0 \exp\left(-\frac{z}{l}\right), \tag{2.3}$$

where z is the height above the coverslip, l is the characteristic penetration depth and I_0 is the intensity at the interface. The penetration depth l can be calculated following

$$l = \frac{\lambda}{4\pi\sqrt{n_1^2 \sin^2(\theta) - n_2^2}}, \tag{2.4}$$

where λ is the wavelength in vacuum. [132]

Typical penetration depths are on the order of 100 nm to 200 nm, restricting the fluorescence excitation to this height over the coverslip [61]. Therefore, TIRF microscopy features a very good signal to background ratio because almost no fluorescence outside of the focal plane is excited.

2.1.5. Resolution limit

Ernst Abbe discovered already in 1873 the limited resolution of optical microscopes [1]. He considered a periodic grating being both illuminated with coherent light under the angle θ and observed through an objective lens with the half opening angle θ. This has led to the equation describing the diffraction limit

$$d = \frac{\lambda}{2\, n \sin\theta}, \tag{2.5}$$

which gives the grating constant d that can just be resolved with the optical system. In this equation, λ is the wavelength of the light and n is the refractive index of the medium between the object and the objective lens. Practical terms lead to the definition of the numerical aperture as $\mathrm{NA} = n \sin\theta$.

However, when looking at fluorescence from a single emitter perspective, such as individual dye molecules, these should be considered as incoherent point sources. Due to the limited bandwidth of the optical system, not all spatial frequencies can be transferred equally. Hence, the image of a point becomes spread out and the resulting detected intensity distribution is called point spread function (PSF), which can be mathematically described by a two- or three-dimensional function. If a point emitter, which is positioned in the focus of an imaging system, is observed through

a circular aperture with limited size, the resulting image is the Airy diffraction disc (Figure 2.3a)

$$I = I_0 \left(\frac{2\ \mathrm{J}_1\left(\frac{2\pi r}{\lambda} \sin\alpha\right)}{\frac{2\pi r}{\lambda} \sin\alpha} \right)^2, \tag{2.6}$$

where I_0 is the peak intensity, J_1 denotes the first kind Bessel function of first order, and r is the radius. Its first minimum is at $\sin\alpha \approx 1.22\frac{\lambda}{d}$, which has led Lord Rayleigh to the definition of the Rayleigh criterion

$$d = 1.22\frac{\lambda}{2\,\mathrm{NA}}. \tag{2.7}$$

This is motivated by the fact that the maximum of the Airy pattern of one point emitter coincides with the first minimum of the Airy pattern of a second point emitter, if they are separated by this distance d (Figure 2.3b). The sum of their intensities will show a dip at $\frac{d}{2}$ of about 26% from the maximum signal which makes it possible to discriminate the two points in the diffraction limited image. In a similar manner, resolution in axial direction can be approximated by

$$d_z = \frac{2\,\lambda\,n}{\mathrm{NA}^2}, \tag{2.8}$$

but this work only deals with two-dimensional imaging approaches. [107]

A Gaussian function approximates well the central part of the Airy disc (Figure 2.3c) and its full-width-at-half-maximum (FWHM) matched approximately the Rayleigh criterion. Measuring the PSF of a sub-diffraction sized emitter that is in focus of the microscope [35] and fitting a Gaussian function to it allows for a simple estimation of the resolving power of the system. Furthermore, the center of the Gaussian function can be used to approximate the position of the emitter [45].

It should be noted that besides Abbe's view in considering spatial frequencies and Rayleigh's view in considering the first minimum of the theoretical PSF, there are more definitions of optical resolution. For instance, Sparrow investigated the image of two emitters that are moved together and defined resolution as the distance where the dip in the intensity distribution just vanishes [193]. Noise and other parameters can also influence the resolution of experimentally acquired images. Hence, many aspects might need to be taken into account and different metrics can report different values [124].

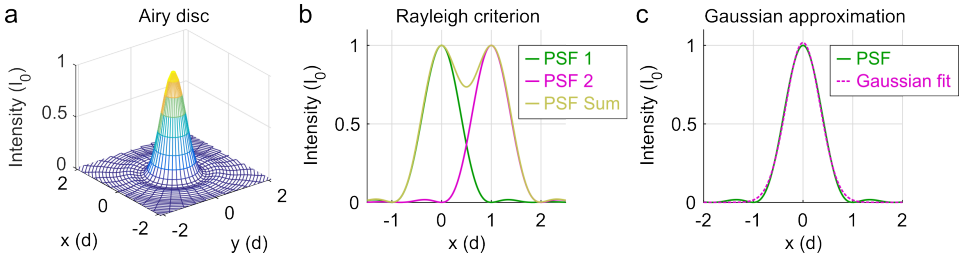

Figure 2.3.: **a**, The image of a point like emitter in the focus of a diffraction limited imaging system is the Airy disc. **b**, The Rayleigh criterion defines the resolution as the distance where the maxium of one Airy disc coincides with the first minimum of another, here shown for the line profile. **c**, The Airy disc can be well approximated by a Gaussian function of which the FWHW gives an estimate for the resolution.

To be able to visualize a certain resolution when an image is recorded with a pixelated detector, i.e. a camera, the Nyquist(-Shannon) sampling theorem demands sampling of at least twice the resolution [145, 180]. Accordingly, the pixel width must be chosen as at most one half of the resolution when being projected through the optical system. Diagonal features are also desired to be resolved with detectors of usually squared pixels, which leads to an additional factor of $\sqrt{2}$. Smaller effective pixel sizes usually do not yield additional information, but decrease the signal-to-noise ratio (SNR). Hence, the backprojected pixel width a can be chosen as

$$a = \frac{d}{2\sqrt{2}}. \tag{2.9}$$

Consideration of the microscope's PSF allows for an analytical expression of the image formation process. A distribution f of fluorescing labels is convolved with the PSF when observed through a microscope. Accordingly, the measured image g is

$$g = f \otimes \mathrm{PSF}, \tag{2.10}$$

where $\otimes$ denotes the convolution operator [172]. Transformation to Fourier space yields

$$\mathcal{F}\{g\} \propto \mathcal{F}\{f\}\ \mathrm{OTF}, \tag{2.11}$$

where $\mathcal{F}$ denotes the Fourier-transformation and OTF is the optical transfer function, i.e. the Fourier-transform of the PSF. Hence, the convolution operation becomes a multiplication in Fourier space. By knowledge of the PSF or OTF, respectively, this process can partially be reversed by division in Fourier space, e.g. by Wiener-filtering [215]. However, the OTF drops to zero at the spatial frequency corresponding to the resolution limit. As no information of higher frequencies is being transferred through the optical system, Wiener filtering cannot increase the resolution. In contrast, Richardson-Lucy deconvolution [130, 164] uses a maximum-likelihood approach to retrieve information beyond the resolution limit by exploiting knowledge of the PSF or OTF, respectively [86].

2.2. Approaches to super-resolution fluorescence microscopy

Multiple methods have been developed for imaging at resolutions better than the diffraction limit [65, 171, 176]. Four families belonging to the most widely used approaches are introduced in the following.

2.2.1. Stimulated emission depletion

Stimulated emission depletion uses a point scanning approach where the diffraction limited, scanned spot is overlaid with an optical vortex [88, 216]. The latter is termed STED-beam. Its doughnut-shaped profile forces the dye molecules in the proximity of the focus to their ground-state, narrowing the effective region from where fluorescence is recorded. A similar principle is also used in the microscopy technique of reversible saturable/switchable optical linear fluorescence transitions (RESOLFT) [95]. In STED, the reachable resolution follows

$$d \approx \frac{\lambda}{2\,\mathrm{NA}\sqrt{1+\frac{I}{I_{\mathrm{sat}}}}}, \tag{2.12}$$

where I is the maximal focal intensity applied for STED and I_{sat} is a characteristic value at which the fluorescence probability is reduced to $\frac{1}{e}$ [216]. Accordingly, the resolution can be increased by increasing I, thus the resolution enhancement is in principle not limited, but depends on the intensity of the depletion beam, limiting the applicability in live-cell imaging due to phototoxicity [105, 212].

2.2.2. Structured illumination microscopy

Gustafsson/Heintzmann structured illumination microscopy [80, 87] exploits the effect of Moiré fringes when illuminating the sample with sinusoidal patterns at different angles and phases. The resolution enhancement of this approach is limited to a factor of two, while 9 (in 2D-SIM) or 15 (in 3D-SIM) [81] raw widefield images need to be recorded for the reconstruction of one super-resolved image plane. As a big advantage, low intensities can be used because no nonlinear effects in terms of the relation between illumination intensity and fluorescence signal are necessary. Hence, SIM is usually considered a good choice for live-cell super-resolution imaging [117]. Combination with photoswitching also enables a resolution enhancement beyond a factor of two that is in principle unlimited [162].

2.2.3. Fluctuation-based super-resolution microscopy

Fluctuation-based approaches use time traces of fluorescent labels that stochastically fluctuate in their intensity [41, 222].

Super-resolution optical fluctuation imaging (SOFI) [41, 42] calculates cumulants on each pixel. The effect of this statistical analysis is the nonlinear suppression of the intensity from emitters that are not located in this pixel. Accordingly, the PSF becomes effectively narrowed, leading to enhanced resolution. By choosing the cumulant order, it is possible to influence the narrowing of the PSF, though this results in nonlinear intensity amplification, complicating quantitative analysis of the resulting image. However, an extension of the theory based on the analysis of multiple orders aims at canceling out nonlinear effects [68].

Entropy-based super-resolution imaging (ESI) [222] relies on pixelwise computation of the Shannon-Entropy weighted with higher-order moments. Just like in SOFI, this leads to a narrowing of the PSF which improves the resolution. As it exploits entropy values, this technique benefits from multiple intensity levels for each emitter. Hence, blinking is not a necessary requirement, but the resolution enhancement can for example be generated from slowly bleaching fluorescent beads. Comparable to the original implementation of SOFI, ESI suffers from nonlinearities in the super-resolved reconstruction that might need to be corrected in the resulting image [2].

Both SOFI and ESI feature the advantage that the individual emitters do not need to be spatially well-separated in each frame. They can therefore be applied to data with a high number of simultaneously active emitters. Furthermore, a high

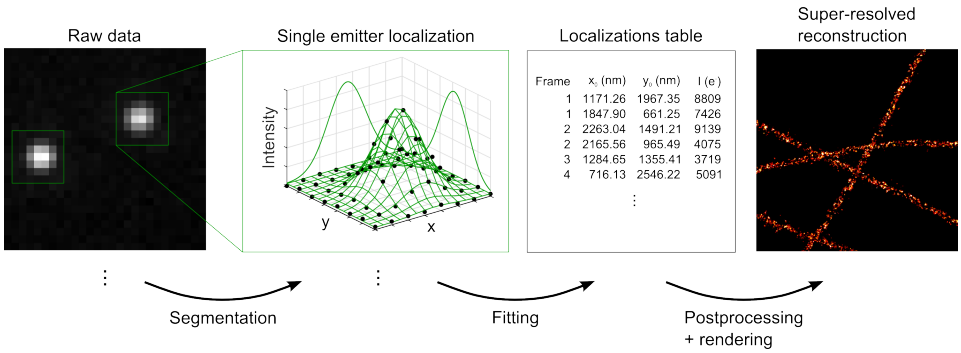

Figure 2.4.: The principle of single molecule localization microscopy. Individual emitters are segmented and their position is found with high precision, e.g. via fitting the PSF to the recorded intensity distribution. Iterating this procedure for all identified emitters and all frames results in a localizations table that includes the individual emitters' positions and further information. This can be used for postprocessing, e.g. filtering for specific values, before a super-resolved image is reconstructed from the table.

temporal resolution can be achieved as not all labels within a diffraction limited region need to be localized subsequently. An advantage over SIM and STED is its low technical complexity as it can be performed on common widefield microscopes without the additional need for beam shaping. The main requirement is made with respect to the probes that need to exhibit at least two states, e.g. one on-state and one off-state. Accordingly, fluctuation-based nanoscopy has been demonstrated for organic dyes [42], quantum dots [41] and fluorescent proteins [38].

2.2.4. Single molecule localization microscopy

Single molecule localization microscopy techniques use photochemistry or -physics for preparing the majority of fluorescent emitters in their off-state, leaving only a small fraction in the on-state. Preferably, the central parts of their PSFs do not overlap. In this case, the individual emitters can be segmented. Explicitly using the knowledge about the PSF shape allows for finding the emitter coordinates with high precision, e.g. via fitting of a two-dimensional Gaussian function to the intensity distribution [146, 149, 220]. This is typically performed in up to thousands of frames of raw widefield data. A new subset of emitters is desired to be active in each frame and each emitter is desired to be localized once during the experiment.

The algorithmic localization results in a table of the individual emitters' 2D or 3D [98] positions. Each emitter can be assigned additional information as for instance the number of detected photoelectrons, the width of the PSF, the background offset, the background noise, or the localization precision. Such information allows for filtering the data in a postprocessing routine before the super-resolved image is rendered from the localizations table [144]. This workflow is depicted in Figure 2.4.

Photoswitching is a key to successively localize emitters that lie closer together than the diffraction limit. Multiple techniques have been developed that rely on different mechanisms for photoswitching. The technique of *d*STORM [85] allows for using a variety of organic dyes [40] and exploits the pathways described in section 2.1.2. This is the technique mainly used in this work.

While direct switching is used in *d*STORM, pairs of different organic dyes in close proximity can also be used for switching which is the approach of STORM [168]. In contrast, (F)PALM uses photoactivatable [18, 92] or photoswitchable [134] fluorescent proteins. Though often suffering from a lower number of detected photoelectrons per localization, fluorescent proteins can be used for live-cell SMLM more easily due to cellular expression [185]. However, organic dyes also allow for live-cell imaging, e.g. demonstrated for high-density, environment-sensitive (HIDE) membrane probes [196]. In HIDE, a reversible chemical reaction switches the dyes between fluorescent and non-fluorescent states. Labels which show only remarkable fluorescence when bound to their target structure can also be used to generate sparse blinking due to binding and unbinding. This is the principle of points accumulation for imaging in nanoscale topography (PAINT) [182] which has for instance been demonstrated for lipids and DNA [179]. The combination with the dynamical binding and unbinding of short complementary DNA fragments that are conjugated to antibodies and dyes has led to the development of DNA-PAINT [113, 178]. A big advantage of this approach is that the dye blinking kinetics and therefore, the number of detected photoelectrons per localization, do not mainly depend on the dye photophysics but on the DNA binding kinetics. Other approaches to blinking labels include the use of caged fluorophores [206] and quantum dots [97].

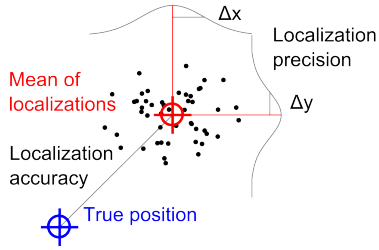

Figure 2.5.: The difference between the mean coordinate of multiple emitter localizations and the true coordinate corresponds to the localization accuracy, while the spread around the mean position corresponds to the localization precision.

2.3. Single emitter localization accuracy

It is the aim of SMLM localization routines to find the position of each emitter as accurately and precisely as possible. If one emitter could be localized multiple times, the spread around the mean position corresponds to the localization precision, while the deviation to the true position corresponds to the localization accuracy (Figure 2.5) [45]. While it is possible to measure the localization precision in a SMLM experiment (cf. section 2.4), the localization accuracy cannot easily be measured because the true molecule position is typically not known.

Multiple effects decrease the localization accuracy such as optical aberrations [29] or detector inhomogeneities [126]. Additionally, the dipole orientation of single molecules causes an anisotropy in the photon emission that can severely decrease the accuracy in case of spatially fixed emitters when using 2D Gaussian fitting for position determination [55]. However, emitters are often free to rotate such that the dipole orientation can be neglected due to an averaging effect [33].

2.4. Single emitter localization precision

2.4.1. Estimation from photon statistics

The localization precision strongly depends on the signal statistics. Due to the discrete nature of photon detection, the signal follows a Poisson distribution which results in shot-noise. If only photon shot-noise is taken into account, the one-

dimensional localization precision Δx can be approximated [18] as

$$\Delta x \approx \frac{\sigma}{\sqrt{N}}, \tag{2.13}$$

where σ denotes the PSF width given as the standard deviation when the PSF is approximated by a Gaussian function and N denotes the number of detected photons, or photoelectrons, respectively. Thompson et. al [200] have demonstrated that the localization precision is further determined by the standard deviation of the background noise b, the backprojected pixel width and height a and find that

$$\Delta x = \sqrt{\frac{\sigma^2 + \frac{a^2}{12}}{N} + \frac{8\pi\sigma^4 b^2}{a^2 N^2}}. \tag{2.14}$$

This model for the localization precision was later refined by Mortensen et al. [138] and is given as

$$\Delta x = \sqrt{u\frac{\sigma^2 + \frac{a^2}{12}}{N}\left(\frac{16}{9} + \frac{8\pi\left(\sigma^2 + \frac{a^2}{12}\right)b^2}{N\,a^2}\right)}, \tag{2.15}$$

where u is a camera-specific parameter accounting for excess noise if necessary, thus $u = 2$ in case of an EM-CCD detector, and $u = 1$ else, e.g. in case of a (s)CMOS detector.

Estimating the signal statistics from the fit to the individual emitter events in the raw data allows for a calculation of the localization precision for each localization separately, e.g. implemented in the localization and reconstruction software packages *rapid*STORM [219] and ThunderSTORM [149] that are used in this work. Besides the models of Thompson et al. and Mortensen et al., the localization precision can be assessed in alternative ways in 2D and 3D SMLM [45], while the best theoretically possible localization precision can be calculated using the Cramer-Rao lower bound [146].

2.4.2. Estimation from localized positions via standard deviation

The repeated localization of the same emitter in multiple frames allows for the measurement of the localization precision Δx as it describes the standard deviation of the localized positions around a mean position $\bar{x}$ [45]. Accordingly, the

localization precision for each lateral direction is given as

$$\Delta x = \sqrt{\frac{1}{\mathrm{n}-1}\sum_{i=1}^{\mathrm{n}}(x_i - \bar{x})^2}, \tag{2.16}$$

where n is the number of repeated localizations and x_i is the coordinate in one spatial direction.

For application of this method, it must be ensured that the localizations arise from the same emitter. Hence, it can for instance be used on sparsely distributed, constantly fluorescing emitters such as sub-diffraction sized beads. In contrast, multiple localizations of the same emitter are usually not desired in SMLM experiments as they unnecessarily increase the number of frames.

2.4.3. Estimation from localized positions via nearest neighbors in adjacent frames

Though undesired, the repeated localization of the same emitter in adjacent frames cannot be completely avoided due to the stochastic nature of the photoswitching process. Endesfelder et al. have discussed how this property can be used to estimate the localization precision [56]. Taken two localized coordinates $\boldsymbol{x}_i$ and $\boldsymbol{x}_j$ of the same emitter that follow the statistics of a Gaussian distribution with the standard deviation Δx, their relative pair-wise distances $|\boldsymbol{x}_j - \boldsymbol{x}_i|$ follow the probability distribution

$$\mathrm{PPD}(|\boldsymbol{x}_j - \boldsymbol{x}_i|) = \frac{|\boldsymbol{x}_j - \boldsymbol{x}_i|}{2(\Delta x)^2}\exp\left(-\frac{|\boldsymbol{x}_j - \boldsymbol{x}_i|^2}{4(\Delta x)^2}\right). \tag{2.17}$$

When an emitter is localized multiple times, the relative pair-wise distances could be binned and fitting the PPD with Δx as the free parameter allows for finding the localization precision as an alternative way to using equation (2.16). Nevertheless, this procedure is unnecessary because the direct computation of the standard deviation can easily be applied when the mean position can be calculated.

In contrast, many emitters are localized at different positions in a SMLM experiment of which some emit in adjacent frames while others do not. Taking only those emitters that have been localized multiple times allows for finding the localization precision Δx by fitting the PPD. In this manner, the average localization precision can be estimated from multiple emitters while equation (2.16) only gives

the localization precision for a single emitter which is required to be localized in many frames as $\bar{x}$ needs to be calculated. This is not necessary when using the PPD.

It is not easily possible to find exactly the localizations that belong to emitters which have been localized in multiple frames. Thus, Endesfelder et al. suggest to search for the nearest neighbor for each emitter in the adjacent frame and use these distances as $|\boldsymbol{x}_j - \boldsymbol{x}_i|$ each. If one emitter has been localized in both frames, it will give the desired contribution to the probability distribution. However, many nearest neighboring localizations in adjacent frames will stem from different emitters and the probability distribution will therefore not follow the form of equation (2.17). Therefore, correction terms are introduced that account for correcting those effects in the short and long spatial range. The resulting function

$$\begin{aligned} \mathrm{PPD}_{\mathrm{corr}}(|\boldsymbol{x}_j - \boldsymbol{x}_i|) = \quad & A_1 \, \frac{|\boldsymbol{x}_j - \boldsymbol{x}_i|}{2(\Delta x)^2} \exp\left(-\frac{|\boldsymbol{x}_j - \boldsymbol{x}_i|^2}{4(\Delta x)^2}\right) \\ + \quad & A_2 \, \frac{1}{2\pi\omega^2} \exp\left(-\frac{\left(|\boldsymbol{x}_j - \boldsymbol{x}_i| - x_{\mathrm{c}}\right)^2}{2\omega^2}\right) \\ + \quad & A_3 \, |\boldsymbol{x}_j - \boldsymbol{x}_i| \end{aligned} \tag{2.18}$$

is fit to the distribution of nearest neighbors in adjacent frames calculated from the localizations table in order to find the localization precision Δx. In the fitting procedure, Δx, A_1, A_2, A_3, ω, and x_c are free parameters.

2.4.4. Comparison of different methods

As a drawback of the method using nearest neighbors, the correction terms in equation (2.18) have not been derived analytically but have been been introduced from heuristic arguments [56]. Furthermore, many parameters need to be determined from the fit which leaves some freedom and might lead to an error in the determination of Δx.

The alternative estimation from the photon statistics requires a precise camera characterization to correctly calculate the photon statistics. Hence, fitting the nearest neighbor distribution might be considered to more robustly state the achieved localization precision because it is calculated from the emitter position list used to render the SMLM image. The same holds for the computation of the localization precision directly from the standard deviation, though this is only possible for emitters localized in many frames which is usually not given for SMLM data.

Deviations in the mean or average localiation precision determined from different methods can indicate deviations from the underlying assumptions. For instance, a moving sample can distort the PPD or interpreting the emission from multiple emitters as the emission from a single emitter can lead to an overestimation of the single emitter photon count.

2.5. Resolution estimation in SMLM

Multiple parameters influence the resolution in SMLM [56]. While the localization precision determines how precisely individual labels can be localized, the localization density determines how well structures are spatially sampled [121, 185]. Furthermore, spatial drift of the sample during the raw data acquisition affects the resolution [136].

2.5.1. Line profile measurements

Following Sparrow's definition [193], an easy way to measure the obtained resolution is the analysis of line profiles measured in the reconstructed image. If a dip is visible in the intensity profile between two structures, these can be assumed to be resolved [51, 85] and the distance between the peaks gives an estimate for the resolution that was at least achieved. This approach is generally applicable to different microscopy approaches [42].

It is also common practice to measure the profile orthogonal to a narrow structure and fit a Gaussian function to this distribution [165, 179, 217]. In this case, the corresponding FWHM can be assumed as the obtained resolution. A similar value can in theory also be found when multiplying the localization precision Δx with a factor of $2\sqrt{2\ln 2} \approx 2.355$, because

$$\mathrm{FWHM} = 2\sqrt{2\ln 2}\,\Delta x \approx 2.355\,\Delta x. \tag{2.19}$$

Though it can provide a simple indication of the obtained resolution, this approach has multiple drawbacks. For example, localization density is not considered. Furthermore, the resolution might not be homogeneous in the entire image and this method only reports on the resolution at one selected position in the image.

2.5.2. Localization density

As discussed in section 2.1.5, the Nyquist theorem requires at least two samples per resolution. Shroff et al. have transferred this concept to SMLM [185] where it demands at least two localizations per resolved distance and per dimension. Accordingly, the Nyquist resolution limit L in 2D SMLM is

$$L = \frac{2}{\sqrt{M}}, \tag{2.20}$$

where M denotes the localization density.

It is one drawback of this approach that it does not take localization precision into account. Additionally, the effective density can be wrongly estimated, e.g. when imaging samples with sparse structures or structures of lower dimensionality such as isolated spots or filaments.

2.5.3. Combining localization density and localization precision

Legant et al. [121] suggested to use a combination of the Nyquist resolution limit L that depends on the localization density and of the localization precision Δx as a lower bound for the resolution R. The suggested definition of the two-dimensional resolution is similar to

$$\mathrm{R} \geq \sqrt{(L)^2 + \left(2\sqrt{2\ln 2}\Delta x\right)^2}, \tag{2.21}$$

when following the definition of [185] to calculate the Nyquist resolution limit L according to equation (2.20).

The factor $2\sqrt{2\ln 2} \approx 2.355$ was left out in the form originally suggested by Legant et al. If infinite localization density M could be achieved (resulting in $L = 0$), the image would show the labeled structure convolved with the Gaussian function that accounts for the limited localization precision. In this case, the FWHM of this distribution is a good approximation for the resolution, hence, it is reasonable to consider this additional factor to translate to the FWHM from the localization precision that is defined as the standard deviation.

2.5.4. Fourier ring correlation

A different approach to the estimation of the resolution is the cutoff frequency of the Fourier ring correlation (FRC). While it has first been applied to electron microscopy [175], Banterle et al. [14] and Nieuwhuizen et al. [143] have introduced this concept to SMLM. It relies on two independent images of the same structure. Their similarity is compared in frequency space and the spatial frequency is determined up to which both images are consistent. The achieved resolution is the inverse of this characteristic frequency.

Two images of the same structure can easily be generated in SMLM by randomly dividing the localizations table into two parts before rendering the two independent images. Additionally, this concepts is generally applicable to approaches that can image the same structure twice, e.g. STED [202].

Computing the image correlation in the frequency space, the FRC is defined [14, 143] as

$$\mathrm{FRC}(k) = \frac{\sum_{\boldsymbol{k}\in\mathrm{circle}} \mathcal{F}\{g_1\}(\boldsymbol{k})\, \mathcal{F}\{g_2\}^*(\boldsymbol{k})}{\sqrt{\sum_{\boldsymbol{k}\in\mathrm{circle}} |\mathcal{F}\{g_1\}(\boldsymbol{k})|^2}\ \sqrt{\sum_{\boldsymbol{k}\in\mathrm{circle}} |\mathcal{F}\{g_2\}(\boldsymbol{k})|^2}}, \tag{2.22}$$

where g_1 and g_2 are the individual images, $\mathcal{F}$ denotes the Fourier-transformation, and the sums are calculated over the pixels on the circles of constant spatial frequency with magnitude $k = |\boldsymbol{k}|$.

Banterle et. al defined the FRC resolution as the crossing of $\mathrm{FRC}(k)$ and the 2σ-curve defined as $\frac{2}{\sqrt{0.5\,\mathrm{N_P}(k)}}$, where $\mathrm{N_P}$ denotes the number of pixels on the circles of constant spatial frequency with magnitude k. Nieuwenhuizen et al. have evaluated different parameters and suggest to use the crossing of $\mathrm{FRC}(k)$ and the constant value of $\frac{1}{7}$, which is the parameter used in this work.

Though FRC aims at combining all parameters that distribute to the image resolution in one metric, it measures a combination of technique-dependent parameters and the spatial frequencies in the sample as pointed out by Nieuwenhuizen et al. [143]. Legant et al. [121] have shown by simulation that keeping the localization precision as well as localization density constant but altering the sample geometry, the FRC resolution can differ in about a factor of two.

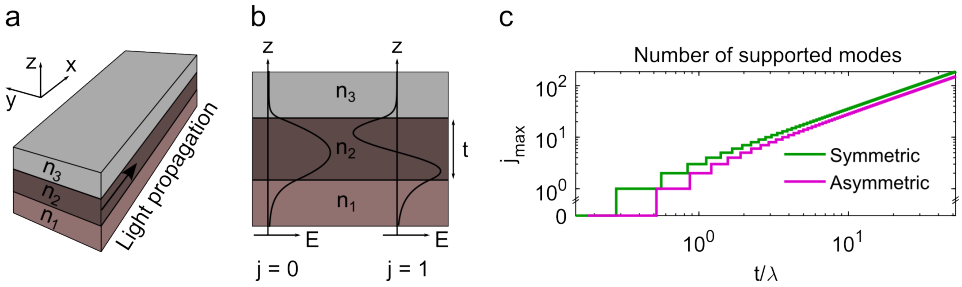

Figure 2.6.: **a**, A waveguide structure can be formed by a region featuring a refractive index n_2 that is higher than the surrounding refractive indices n_1 and n_3. **b**, Exemplary electric field distributions for the 0^{th} and 1^{st} order guided modes. **c**, The maximum number of modes that can be excited is a function of the refractive indices, the width t of the middle layer, and the wavelength λ. The plots show the maximum number of modes as a function of $\frac{t}{\lambda}$ for $n_2 = 2.1$ and the symmetric case of $n_1 = n_3 = 1.33$ as well as the asymmetric case of $n_1 \ll n_3 = 1.518$. The 0^{th} order can be excited for all ratios $\frac{t}{\lambda}$ in the symmetric case, while no excitation, and, hence, no light guiding is possible for $\frac{t}{\lambda} < 0.17$ in the asymmetric case.

2.6. Planar optical waveguides

Optical waveguides confine light by a guiding region that is of higher refractive index than the surrounding media. While waveguides of radial symmetry are commonly used in the popular case of optical fibers [114], planar waveguides can for instance be prepared on waveguide chips in the case of integrated optics [59]. Depending on the layout of the planar waveguide, different modes can be excited, where a mode describes the spatial distribution of optical energy [104].

2.6.1. Mode distribution

Figure 2.6a shows the case where a layer of higher refractive index n_2 is sandwiched by media of lower refractive indices n_1 and n_3 while the light propagation direction is in parallel to the interfaces. The spatial distribution of the electromagnetic field $\boldsymbol{E}(\boldsymbol{x})$ for monochromatic waves is determined according to Maxwell's wave equation

$$\nabla^2 \boldsymbol{E}(\boldsymbol{x}) + k^2 n^2(\boldsymbol{x}) \boldsymbol{E}(\boldsymbol{x}) = 0, \tag{2.23}$$

where k is the wavenumber and $\boldsymbol{x} = (x, y, z)$ denotes the position. Assuming a plane wave propagating in x-direction, the field can be written in the form of

$\boldsymbol{E}(\boldsymbol{x}) = \boldsymbol{E}(y,z)\exp(-i\beta x)$, where β is a propagation constant. Furthermore, no dependence of $\boldsymbol{E}(\boldsymbol{x})$ on the y direction is assumed for simplicity. In this case, equation (2.23) becomes for each of the three regions

$$\frac{\partial^2}{\partial z^2}E(z) + (k^2n^2 - \beta^2)E(z) = 0, \tag{2.24}$$

where $n \in \{n_1, n_2, n_3\}$ describes the according region and $E(z)$ is a cartesian component of the field. Analyzing the components of $\boldsymbol{E}(\boldsymbol{x})$ leads to distinct conditions, e.g. TE and TM-modes. Both $E(z)$ and $\frac{\partial}{\partial z}E(z)$ must be continuous at the interfaces. Depending on the sign of $(k^2n^2 - \beta^2)$, the solutions for $E(z)$ are either sinusoidal or exponential for the three different regions. For guided modes without radiative energy loss, exponential decay is required in the regions of n_1 and n_3 and a sinusoidal solution follows for the region of n_2. [197]

Figure 2.6b shows the electric field in z-direction for the 0^{th} and 1^{st} order modes that obey the above conditions. As the electric field decays exponentially in the regions of n_1 and n_3, also the intensity, that can for instance be used for fluorescence excitation, decays exponentially. This is similar to the intensity distribution in objective-based TIRF excitation.

2.6.2. Number of excited modes

The number of the highest order mode $j_{\max}$ that can be excited depends on the light vacuum wavelength λ, the width t of the n_2 region, and the three refractive indices, assuming that the n_1 and n_3 regions are of infinite extend. In case of a symmetric waveguide, i.e. $n_1 = n_3$,

$$j_{\max} = \left\lfloor \sqrt{8(n_2 - n_3)n_2}\ \frac{t}{\lambda} \right\rfloor \tag{2.25}$$

is the highest order mode that can be excited. For asymmetric waveguides where $n_3 \gg n1$,

$$j_{\max} = \left\lfloor \sqrt{4(n_2 - n_3)(n_2 + n_3)}\ \frac{t}{\lambda} - \frac{1}{2} \right\rfloor \tag{2.26}$$

is the highest order mode that can be excited. [104]

These theoretical considerations are not completely applicable to real waveguides, as for instance the n_2 region is usually restricted in both dimensions or-

thogonal to the light propagation direction, i.e. in y and z direction. In this case, the waveguide properties, e.g. the mode distribution, can be effectively found by numeric modeling [53]. However, handling both directions independently is a good approximation that reveals relevant effects in an analytical way. Equation (2.25) shows that the 0^{th} order mode can always be excited in symmetric waveguides if the refractive index in the center is higher than the refractive indices of the surroundings. In contrast, equation (2.26) shows that there is a cutoff condition for the width of the central region in asymmetric waveguides where the 0^{th} mode, and, accordingly, higher order modes, cannot be excited.

2.6.3. Effective refractive index

Similar expressions can also be found when using a ray optics approach. In this case, straight rays can be assumed to be confined in the layer of n_2 by internal total reflection at the interfaces. For constructive interference, the phase change for a point on the wavefront traveling from one interface to the other and back needs to be a multiple of 2π. This leads to the condition

$$j = \frac{ktn_2}{\pi} \sin\theta_j - \frac{1}{\pi}(\varphi_{12} + \varphi_{23}), \tag{2.27}$$

where $(\varphi_{12} + \varphi_{23})$ is the sum of the Goos-Hänchen shifts [75] at the interfaces and θ_j is the angle of reflection with respect to the x-direction for the j^{th} guided mode. [191]

Again, only discrete values for the mode order j are allowed by the demand for constructive interference and total internal reflection is necessary. This leads to the limited number of angles θ_j defining the guided modes.

Under consideration of the optical path length for the rays traveling back and forth between the interfaces, the velocity v_j for the propagation of the j^{th} order mode in x-direction is

$$v_j = \frac{c}{n_2 \cos\theta_j} \tag{2.28}$$

From this, the effective refractive index $n_{\text{eff},j}$ of the waveguide can be defined [104] by

$$n_{\text{eff},j} = \frac{c}{v_j} = n_2 \cos\theta_j. \tag{2.29}$$

2.6.4. Coupling efficiency

When providing the light to the input facet of the waveguide, e.g. by laser focusing, the coupling efficiency Γ_j to the j^{th} mode is given by the overlap integral of the incident beam at the input facet and the waveguide mode [31, 225], i.e.

$$\Gamma_j = \frac{\left(\iint E_{\text{in}}(y,z) E^*_{\text{wg},j}(y,z)\,\mathrm{d}y\,\mathrm{d}z\right)^2}{\iint |E_{\text{in}}(y,z)|^2\,\mathrm{d}y\,\mathrm{d}z \iint |E_{\text{wg},j}(y,z)|^2\,\mathrm{d}y\,\mathrm{d}z}, \tag{2.30}$$

where $E_{\text{in}}(y,z)$ is the field distribution of the input beam and $E_{\text{wg},j}(y,z)$ is the field distribution of the j^{th} guided mode. While equation (2.30) describes the excitation of the modes, conversion between different modes is also possible during light guiding, especially in case of imperfect or irregularly shaped waveguides [223].

2.7. Holographic optical trapping

2.7.1. Optical trapping

Optical trapping gives the opportunity of manipulating microscopic objects by making use of the photon momentum

$$\mathbf{p} = \hbar \boldsymbol{k}, \tag{2.31}$$

where $\hbar$ is the reduced Planck's constant and $\boldsymbol{k}$ is the wavevector with $|\boldsymbol{k}| = \frac{2\pi}{\lambda}$.

An object of higher refractive index than the surrounding medium that is placed in an intensity gradient experiences a force towards the point of the highest intensity. This effect is used in optical tweezers where a tightly focused laser beam enables stable, three-dimensional trapping of samples at the approximate position of the laser focus. [26]

Though a full decription of this process requires the consideration of Rayleigh and Mie scattering [26], a simple ray optics model together with consideration of the photon momentum is sufficient to explain the basic principles [11]. When the laser focus is placed directly at the center of a fully transparent sphere, symmetry demands that the light cone is not altered. The momentum flux $\boldsymbol{p}_{\text{out}}$ of the light after passing the sphere is therefore equal to the momentum flux $\boldsymbol{p}_{\text{in}}$ before passing the sphere, i.e. $\boldsymbol{p}_{\text{in}} = \boldsymbol{p}_{\text{out}}$. If the sphere is displaced from the focus, it will deflect the light that passes through it [11]. Accordingly, the momentum flux of the light

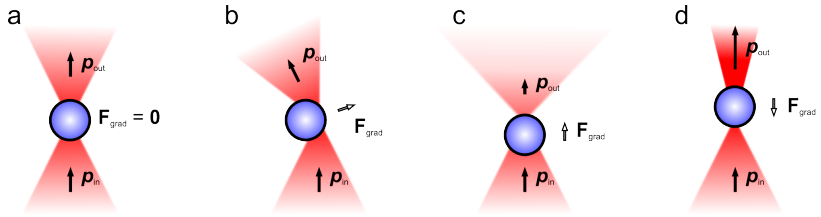

Figure 2.7.: The gradient force is responsible for stable optical trapping. **a**, If a spherical object is placed in the center of a focused beam, the momentum flux of the light is not changed, resulting in a gradient force of $\boldsymbol{F}_{\text{grad}} = \boldsymbol{0}$. Displacement from the center deflects the light, resulting in a gradient force which is proportional to the change in the momentum flux, pulling the sphere back towards the center. As this holds for lateral (**b**) and axial (**c**,**d**) displacements, stable trapping in 3D can be achieved.

is changed by the sphere, yielding a force on the sphere that is proportional to the change in the momentum flux, i.e. $\boldsymbol{F}_{\text{grad}} \propto \boldsymbol{p}_{\text{out}} - \boldsymbol{p}_{\text{in}}$.

In the vicinity of a laser focus, the sphere acts similar to a lens. A lateral displacement deflects the light in the displacement direction, while an axial displacement changes the divergence of the beam (Figure 2.7). In any case, the according force, termed gradient force, pulls it towards the center of the focus [26], while the gradient force is approximately proportional to the displacement, provided the displacement is sufficiently small [62].

However, this is not the only force to consider. Absorption is often neglected in this process, but backscattered light can significantly contribute to the overall force on the sphere. As backscattering also change the momentum flux, the according scattering force $\boldsymbol{F}_{\text{scat}}$ tends to push the particle in the light propagation direction [26]. For stable trapping, it is necessary that the gradient force can overcome the scattering force, wherefore high NA beams are required for stable trapping in all three dimensions. Further relevant forces are the gravitational force $\boldsymbol{F}_{\text{G}}$ and buoyancy $\boldsymbol{F}_{\text{buoy}}$. The mean trapping position $\boldsymbol{x}_0$ is the point where the equilibrium is given, i.e.

$$\boldsymbol{F}_{\text{grad}} + \boldsymbol{F}_{\text{scat}} + \boldsymbol{F}_{\text{G}} + \boldsymbol{F}_{\text{buoy}} = \boldsymbol{0}. \tag{2.32}$$

Besides the light exerting forces on the trapped object, it experiences Brownian motion from the surrounding medium. Though this does not change the equilibrium position, it leads to thermal fluctuations around it [221]. In the vicinity of the focus, only $\boldsymbol{F}_{\text{grad}}$ depends strongly on the particle position $\boldsymbol{x}$ and the trapping potential

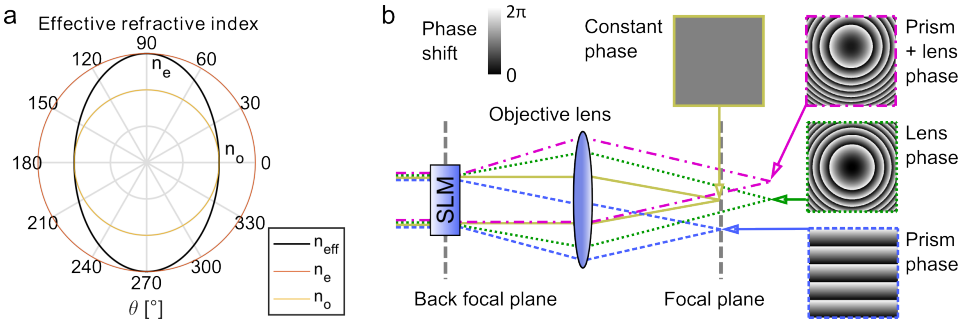

Figure 2.8.: a, The effective refractive index of a birefringent liquid crystal display can be switched between its ordinary and extraordinary refractive indices. This effect is used in a SLM on a 2D grid where the change in the refractive index translates to a phase shift of a transmitted or reflected light wave. **b**, When placed in a plane conjugate to the back focal plane of an objective lens, the SLM can be used to display phase holograms corresponding to the phase shifts of optical elements such as a prism, or a lens, or its combination. This gives control over the position of the light focus in a volume around the focal plane. Adapted from [26].

can be assumed as a harmonic potential [49], thus

$$\boldsymbol{F}(\boldsymbol{x}) = -\boldsymbol{\kappa}(\boldsymbol{x} - \boldsymbol{x}_0), \tag{2.33}$$

where $\boldsymbol{\kappa}$ is the trap stiffness matrix.

The trap stiffness is connected to thermal fluctuations via the equipartition theorem. This relates the thermal energy $k_B T$ to the optical potential energy [142] by

$$\frac{1}{2} k_B T = \frac{1}{2} \kappa \langle (\boldsymbol{x} - \boldsymbol{x}_0)^2 \rangle, \tag{2.34}$$

where κ is the scalar trap stiffness. Accordingly, a lower trap stiffness leads to higher fluctuations in the particle position $\boldsymbol{x}$ around the equilibrium position $\boldsymbol{x}_0$.

2.7.2. Spatial light modulator principles

A spatial light modulator (SLM) offers the ability to change the properties of light which is transmitted or reflected by it. For this purpose, pixels arranged on a two-dimensional grid are independently controlled to change the phase, polarization, or amplitude of a light wavefront. In this work, a reflective SLM is used to display

phase patterns for beam steering, so the remainder of this section will focus on this purpose.

The SLM display can be constructed of liquid crystals (LCs) that consist of rod-shaped molecules in a nematic phase. Hence, these align their axes along a common spatial direction resulting in optical anisotropy. The refractive index for light that is polarized in parallel to the crystal axes (the extraordinary refractive index n_e) is different than the refractive index for light that is polarized perpendicular (the ordinary refractive index n_o). This birefringence is exploited by modifying the tilt of the molecules to alter the effective refractive index for light traveling through the LC layer. When the propagation direction is at an angle α relative to the crystal axes alignment, the effective refractive index n_eff is

$$n_\mathrm{eff} = \frac{n_\mathrm{e} n_\mathrm{o}}{\sqrt{\left(n_\mathrm{e}\,\cos\left(\alpha\right)\right)^2 + \left(n_\mathrm{o}\,\sin\left(\alpha\right)\right)^2}}, \tag{2.35}$$

which is depicted in Figure 2.8a. [115, 152]

If the propagation direction is orthogonal to the crystal axes, the effective refractive index is equal to the extraordinary refractive index. Tilting the molecules into the light propagation direction changes the relative angle α and allows for controlling the effective refractive index. Therefore, the polarization vector of the light needs to be parallel to the plane in which the molecule axes are tilted. Otherwise, only the component of the polarization in this direction will experience the change in the refractive index and the polarization state will be changed. Though this is a desired operation mode for polarization modulation, it is undesired for phase-only modulation. Therefore, specifically linearly polarized light is preferable when SLMs are used for phase modulation. [60]

To control the refractive index, the LC molecules can be sandwiched between a back and a front layer. Applying a voltage over the LC layer [224] or optical addressing [111] allows for tilting of the molecules resulting in the desired change of the refractive index. This translates to a phase shift for a reflected or transmitted light wave due to the change in the optical pathlength. The light passes the LC layer twice in reflective SLMs such that the phase shift ϕ is given by

$$\phi = \frac{4\pi}{\lambda}\left(n_\mathrm{eff} - n_\mathrm{o}\right) l, \tag{2.36}$$

where l denotes the thickness of the LC layer [58]. Individual control for each pixel in a SLM display allows for wavefront shaping on a 2D grid, encoded in phase maps.

The refractive index is a function of the wavelength and, additionally, many SLMs feature a nonlinear relationship between the applied voltage and the resulting phase shift [58]. Therefore, the response of the LC display in terms of its phase shift as a function of the applied voltage needs to be characterized. Inverting this relation gives the look-up-table that is applied to all phase maps before applying these to the SLM. The phase response can be measured in an interferometric way [208], using crossed polarizers and imaging the SLM to a camera [60], or via a diffractive approach [58]. The latter is used to characterize the SLM in this work.

2.7.3. Holographic beam shaping

The wavefront of a plane wave can be modulated by applying position dependent phase shifts to it, e.g. on a 2D pixel grid by the use of a SLM. The effect of such a phase hologram is shaping the wavefront whereupon constructive interference follows for specific angles. It is possible to design holograms by considering the effect of common optical elements such as prisms and lenses on the wavefront (Figure 2.8b).

A prism shifts the phase such that constructive interference appears under an angle relative to the propagation direction of the incoming wave but a plane wavefront is maintained. Hence, the according hologram is wedge-shaped. When being imaged, e.g. by a 4f-telescope, to the back focal plane of an objective lens, the position of the beam entering this plane is not changed but the angle is. This causes the focus to be shifted in the focal plane of the objective lens. The corresponding hologram, i.e. the spatially dependent phase shift $\phi_{\text{prism}}(x, y)$ in the plane of the prism, can be calculated [47] as

$$\phi_{\text{prism}}(x, y) = \frac{2\pi}{\lambda f}(u\,x + v\,y), \tag{2.37}$$

where (x, y) denote the coordinates in the prism plane, (u, v) denote the coordinates in the focal plane, λ is the wavelength, and f is the focal length of the objective lens.

A lens causes a plane wavefront to be shaped concavely or convexly, leading to beam convergence or divergence, respectively. When imaged to an objective lens back focal plane, the focus position will be shifted in the propagation direction. The corresponding hologram has a quadratic curvature, and the spatially dependent

phase shift $\phi_{\text{prism}}(x, y)$ can be calculated [122] as

$$\phi_{\text{lens}}(x, y) = \frac{\pi}{\lambda f^2}(x^2 + y^2)\, w, \tag{2.38}$$

where w denotes the shift in the axial direction.

2.7.4. Lens-and-prism method for hologram computation

The prism or lens, respectively, can be replaced with an SLM that displays the spatially dependent phase shifts as holograms. This gives dynamic control over the focus coordinates (u, v, w) and the effect of both elements can be combined by the sum of the functions modulo 2π via the so-called lens-and-prism method, i.e.

$$\phi(x, y) = \left(\frac{2\pi}{\lambda f}(u\, x + v\, y) + \frac{\pi}{\lambda f^2}(x^2 + y^2)\, w\right) \bmod 2\pi. \tag{2.39}$$

The $\bmod 2\pi$-operation in equation (2.39) is usually applied because of the limited phase-shift of SLMs that are often operated using phase shifts in the range of 0 to 2π only. However, SLM operation in a greater space of phase shifts can be desirable for different reasons such as speeding up their operation [198] or multi-color applications [83].

Besides controlling one focus position only, holograms can be designed for spatial multiplexing that results in multiple foci. The according hologram can in principle be achieved in a non-iterative way [123] following

$$\phi(x, y) = \arg\left(\sum_{j=1}^{\mathrm{n}} A_j \exp\left(i\phi_j(x, y)\right)\right) \bmod 2\pi, \tag{2.40}$$

where n is the number of different foci, $\phi_j(x, y)$ is the hologram corresponding to the j^{th} focus position, A_j is the relative amplitude of the j^{th} focus position and i is the complex unit.

2.7.5. Gerchberg-Saxton algorithm improves hologram computation

The lens-and-prism method usually causes additional spots in the volume around the objective focal plane, referred to as ghost orders [66, 70]. Therefore, the

Gerchberg-Saxton-algorithm [71] is often applied as it uses an iterative procedure to find a hologram that results in a good approximation to the desired intensity distribution in the focal plane of the objective lens [26]. The algorithm uses the fact that the objective lens effectively performs a Fourier-transform of the field in the SLM plane [74], as the SLM is positioned in a conjugate plane to the objective lens back-focal-plane.

The Gerchberg-Saxton-algorithm assumes an input amplitude $A_{\mathrm{in}}(x, y)$ at the SLM, e.g. a constant or a Gaussian laser beam profile, and an initial hologram $\phi_t(x, y)$, forming the field $E_t(x, y) = A_{\mathrm{in}}(x, y) \exp(i\phi_t(x, y))$. This is numerically propagated to Fourier space, resulting in

$$\mathcal{F}\{E(x, y)\} = E'_t(u, v, w) = A'_t(u, v, w) \exp(i\phi'_t(u, v, w)) . \tag{2.41}$$

The obtained amplitude in Fourier space is replaced with the desired amplitude $A'_{\mathrm{desired}}(u, v, w)$ while the phase is kept unchanged, and the field is propagated back to real space, resulting in

$$\mathcal{F}\{A'_{\mathrm{desired}}(u, v, w) \exp(i\phi'_t(u, v, w))\} = E(x, y) = A_{t+1}(x, y) \exp(i\phi_{t+1}(x, y)) . \tag{2.42}$$

Here, the obtained amplitude is replaced with the input amplitude $A_{\mathrm{in}}(x, y)$ while, again, the phase is kept unchanged. The resulting field is used as the starting condition for the next iteration, i.e. $E_{t+1}(x, y) = A_{\mathrm{in}}(x, y) \exp(i\phi_{t+1}(x, y))$.

Accordingly, this procedure propagates the field through successive Fourier-transforms, while making no restrictions with respect to the phase, but restricting the amplitude in each step. The error in $A'_{\mathrm{desired}}(u, v, w)$ decreases monotonically over the iterations [71]. Several modifications can improve the performance, of which restricting the phase change in each step and using amplitude weighting for faster convergence are implemented in the software used in this work [153].

2.7.6. Combination of holographic beam shaping and optical trapping

The combination of holographic beam shaping and optical trapping in one instrument enables the use of holographic optical tweezers. The introduction of a trapping laser in combination with a SLM into a microscope setup together with a camera for optical feedback allows for dynamic positioning of multiple traps. Ac-

cordingly, the user can effectively catch objects, e.g. cells, and manipulate them under the microscope [48, 73, 79]. Though cells cannot always be well approximated by spheres of constant refractive index, the cellular refractive index is usually higher than the surrounding aqueous buffer such that stable optical trapping is also possible in this case.

2.8. Camera detectors

2.8.1. Digital cameras for widefield microscopy

Scanning approaches to microscopy such as confocal imaging or STED often utilize point-detectors and therefore rely on multiplexing for image acquisition. In contrast, the projection of the image in the focal plane of a microscope onto a camera detector allows for simultaneous widefield imaging of a certain sample area. [183]

Digital cameras feature a two-dimensional grid of pixels that individually convert detected photons into photoelectrons via the inner photoelectric effect. The charge is accumulated over the exposure time of one frame and then read out by conversion to a digital signal. Afterwards, the charge is being reset such that new photons can be detected in the next frame. [140]

2.8.2. EM-CCD architecture

Charge coupled device (CCD) cameras of frame transfer architecture possess two pixel arrays. The first features light sensitive pixels that accumulate the charge during the exposure time. After the exposure, the distribution of charges is transferred in a column-wise manner to a second storage array of the same size that is not light sensitive. For conversion to a digital signal, the charges are shifted from the second array row-wise into a shift register, from where they are read pixel-by-pixel through one analog-to-digital converter. As one element is used to read all pixels subsequently, CCD cameras can reach high detector uniformities. The second array is used to store the charges before readout such that the light sensitive pixels in the first array are again ready for charge accumulation as soon as the charge distribution has been transferred to the second array. [10] Optimized detector designs have enabled CDD detectors with quantum efficiencies up to 95% [99], i.e. almost all photons reaching the camera chip contribute to the image.

In electron multiplying charge coupled device (EM-CCD) cameras, the charges are transferred through an additional serial multiplication register. A high volt-

age applied to it leads to impact ionization that effectively multiplies the original charge. This can significantly amplify the detected signal, leading to a high ratio of the signal relative to the noise introduced in the analog-to-digital conversion. Accordingly, even single photons can be detected [166]. The drawback of the electron multiplication is the introduction of excess noise, effectively halving the quantum efficiency [138]. The combination of these properties makes EM-CCD cameras particularly suited for for imaging at very low signal levels [99].

2.8.3. CMOS architecture

In contrast to EM-CCDs, cameras of complementary metal-oxide semiconductor (CMOS) architecture posses a separate readout amplifier for each pixel. This allows for significantly higher readout rates in comparison to EM-CCD cameras [140]. Furthermore, scientific-grade CMOS (sCMOS) cameras often feature a larger chip size that translates to a larger FOV for imaging, provided a matched magnification.

As a drawback, the parallel amplification for all pixels leads to notable inhomogeneities of the camera chip [16], resulting in pixel-to-pixel variations in terms of amplification gain, read noise, and offset [128]. The best quantum efficiencies of sCMOS detectors have not yet reached that of EM-CCDs, but as no excess noise occurs, the effective quantum efficiency can be higher than 50%. However, the lack of EM gain amplification before readout makes sCMOS cameras better suited for imaging of higher signal levels in comparison to EM-CCD cameras [131].

3. Waveguide chip-based nanoscopy

This chapter is based in major parts on the peer-reviewed publication

R. Diekmann*, Ø.I. Helle*, C.I. Øie, P. McCourt, T. Huser, M. Schüttpelz, and B.S. Ahluwalia. Chip-based wide field-of-view nanoscopy. *Nature Photonics*, **11**(5):322–328, 2017, (* equal contribution)

and the invited articles

R. Diekmann and M. Schüttpelz. Nanoscopy On-a-Chip: Ultra large field-of-view super-resolution microscopy. *Imaging and Microscopy*, in print, 2017,

R. Diekmann and M. Schüttpelz. Nanoskopie in HD-Qualität. *GIT Labor-Fachzeitschrift*, in print, 2017,

R. Diekmann and M. Schüttpelz. Chip-based nanoscopy in HD quality. *G.I.T. Laboratory Journal Europe*, in print, 2017.

Common implementations of SMLM deliver the light for fluorescence excitation through objective lenses, imposing constraints on the simultaneously illuminated area or optical sectioning capability. The use of planar waveguides for fluorescence excitation in their near field overcomes both bottlenecks. The excellent optical sectioning capability of TIRF is combined with an almost arbitrarily large concurrently illuminated area. The use of standard high magnification/ high NA detection optics yields comparable results to conventional objective-based TIRF *d*STORM. However, waveguides also enable the utilization of low magnification/ low NA objective lenses for diffraction limited as well as for super-resolution imaging that is demonstrated for FOV sizes up to $0.5\,\mathrm{mm} \times 0.5\,\mathrm{mm}$. Accordingly, more than 50 cells can be captured in one image at super-resolution. Bio-compatability of the waveguide chips allows for live-cell imaging and intrinsic multi-mode interference patterns also render fluctuation-based super-resolution imaging with high temporal resolution possible. Hence, using waveguides allows to flexibly choose the tradeoff between temporal resolution or throughput, respectively, and spatial resolution. This is possible for a wide range of conditions as well as unprecedented FOV sizes in TIRF illumination.

3.1. Introduction

Waveguides of fiber geometry are a frequent tool in fluorescence microscopy to guide the excitation light from the laser source to free-space optics. These are used to shape the beam for the sample excitation that is often delivered through an objective lens to the sample. Besides the technical demands, using a high NA objective lens with a high magnification consequently limits the FOV. This makes simultaneous super-resolution imaging of several to many cells difficult.

In contrast, the utilization of planar waveguides allows to directly excite fluorescence in their near-field by the evanescent part of the guided light without the need for additional free-space optics. This reduces the complexity of the entire optical setup, enabling miniaturization by completely removing the excitation light path from the microscope. Instead, waveguides which tightly confine the guided light are used to deliver the illumination light to the sample. The evanescent field on top of the waveguide can be utilized for TIRF excitation over an almost arbitrarily wide FOV that is intrinsically independent of the detection objective lens and in principle only limited by the waveguide design. Evanescent field excitation using waveguides was introduced by Grandin et al. [76], where a slab waveguide was used to generate an evanescent field over the large stretch of the waveguide chip. Slab waveguides (Figure 3.1b) have later been used for both fixed and live cell fluorescence imaging [3, 4, 184] as well as for label free imaging [5]. In another work [161], a coverslip was used to support guided modes of light, providing an evanescent field across the entire coverslip. Although these previous approaches to waveguide-based illumination have been used for fluorescence microscopy for some time, none of these techniques have yet demonstrated imaging with a resolution beyond the diffraction limit. This chapter presents nanoscopy at different modalities using chip-based waveguides, including fluctuation-based and single emitter localization-based image reconstruction.

The large FOV of this illumination scheme renders high throughout SMLM possible and makes efficient use of the big detector sizes of modern sCMOS cameras [99]. Other researchers have demonstrated large FOV *d*STORM imaging in epi-illumination over areas of $100\,\mu m \times 100\,\mu m$ by free-space beamshaping [51] or $221\,\mu m \times 221\,\mu m$ by fiber-based beamshaping [228]. The waveguide-based illumination extends large FOV *d*STORM to TIRF and further increases the possible throughput of SMLM. However, extending the FOV by using low magnification/ low NA objective lenses for detection increases the probability of overlapping point-spread-functions (PSFs) as their width depends on the NA. This imposes con-

straints on the number of simultaneously active emitters. Accordingly, more raw frames need to be recorded to achieve a similar localization density as this restricts the resolution [121, 169]. The interplay between the throughput and the achievable resolution depends on different parameters. Finding the optimum includes the consideration of different techniques and is evaluated in detail in this chapter after the implementation and characterization of the different waveguide-based imaging modalities.

3.2. Waveguide characterization for near-field excitation in fluorescence microscopy

3.2.1. Waveguide layout and optical setup

Planar waveguides made from tantalum pentoxide (Ta_2O_5) or silicon nitride (Si_3N_4) are prepared on silicon dioxide (SiO_2) substrate (Figure 3.1a,b). These materials are chosen because of their high refractive indices, low propagation losses, low absorption, and low auto-fluorescence at visible wavelengths [6]. To achieve high intensities in the evanescent field, channel-like waveguides of rib or strip geometry are used (Figure 3.1c). These transversely confine the guided light in contrast to the slab geometry used in other waveguide-imaging approaches [76, 3, 4, 5]. Channel widths (i.e. the waveguide extend orthogonal to the wave propagation direction) range from 25 µm to 500 µm in order to span the appropriate length scale for imaging many samples simultaneously, e.g. several cells.

Light can be coupled into the waveguide either by focusing a collimated laser beam via an objective lens to the input facet or by coupling from a lensed or cleaved fiber (Figure 3.1d). Calculation of the absolute coupling efficiency requires extensive knowledge of the waveguide mode distribution (cf. equation (2.30)) which was not available, so the relative coupling efficiencies were measured instead. Using fluorescent beads as intensity sensors, coupling from different objective lenses was characterized (Figure 3.2). The most efficient lens type was chosen for the experiments presented here. The illumination unit consists of four solid state lasers of different wavelengths or an Argon-Krypton-ion laser whose wavelengths are selected via an acousto-optical tuneable filter. When the light is coupled into the waveguide, its evanescent field excites fluorescence in samples on top of the waveguide that is collected through an upright microscope in orthogonal direction (Figure 3.1b). This is optionally equipped with a z-piezo for focus correction during the experiment

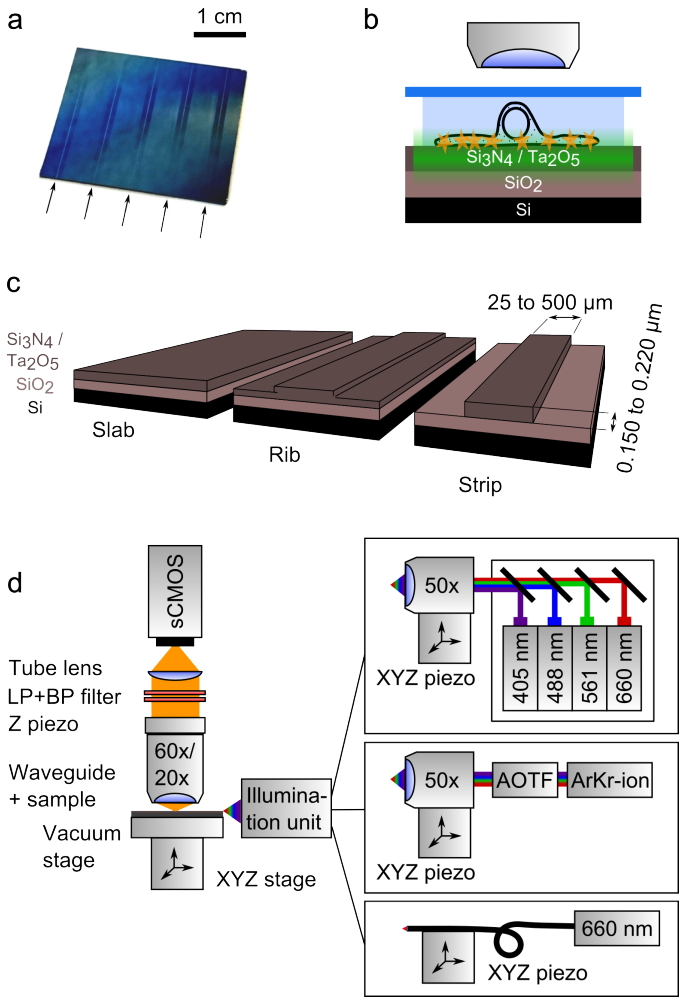

Figure 3.1.: The principle of waveguide-based fluorescence imaging. **a**, Photo of a Ta_2O_5 strip waveguide chip. Five channels can easily be seen, marked by the arrows. **b**, Light guided inside the waveguide is the source of the evanescent field illuminating samples on top of the surface. **c**, Channel-like waveguide geometries are realized by etching the slab waveguide either partially or completely down to the SiO_2 substrate. In either case, the light is mainly guided by the channels of $25\,\mu m$ to $500\,\mu m$ width. **d**, The optical setup consists of an upright microscope for fluorescence detection and an illumination unit to provide coupling to the input facet of the waveguides either through an objective lens or via a (lensed) fiber. Different solid-state lasers are combined or an Argon-Krypton-ion laser is used as the illumination source.

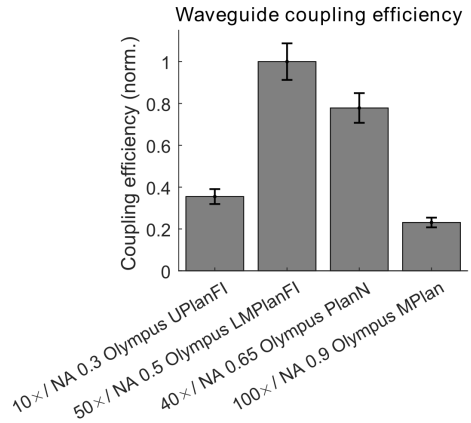

Figure 3.2.: The coupling efficiency for objective-based coupling strongly depends on the utilized objective lens for focusing the collimated laser beam to the input facet of the waveguide.

and a whitelight-source for epi-illumination which enables observation of the chip during the task of establishing coupling.

3.2.2. Optical sectioning

The fluorescence excited by the evanescent field of the waveguide provides optical sectioning. Typical penetration depths range from (172 ± 54) nm when using illumination of 488 nm vacuum wavelength and (190 ± 59) nm when using illumination of 660 nm vacuum wavelength. The strength of the evanescent field was measured using beads of 8.18 µm diameter whose surface was fluorescently labeled. Measuring the individual bead diameter and finding its center allows for calculating the height of its surface over the waveguide [133, 194]. The spatially dependent strength of the evanescent field was then measured by the fluorescence intensity. Figure 3.3 shows a typical result of the evanescent field measurement for a vacuum wavelength of 660 nm.

3.2.3. Simultaneous coupling for multi-color imaging and photoswitching

Different wavelengths can be combined by simultaneous coupling. This allows for multi-color imaging as shown in Figure 3.4a for a mixture of fluorescent beads la-

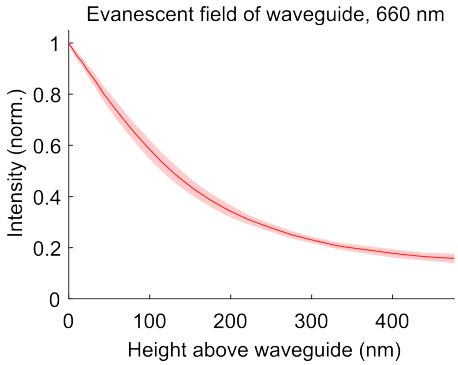

Figure 3.3.: The evanescent field of the waveguide decays at penetration depths of about $200\,\mathrm{nm}$, here exemplary shown for a vacuum wavelength of $660\,\mathrm{nm}$.

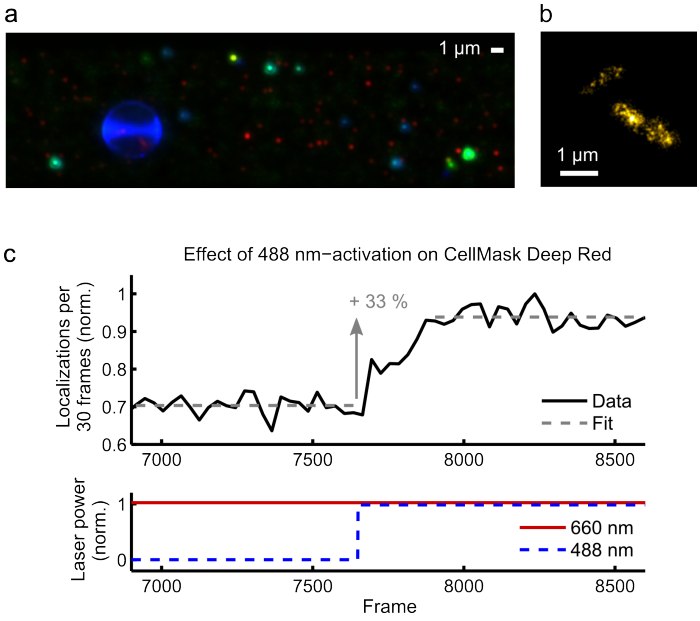

Figure 3.4.: Different wavelengths can be coupled either simultaneously or sequentially into the waveguide. **a**, This allows for multi-color imaging as shown for fluorescently labeled beads with four different dyes. **b**, Furthermore, dyes can be effectively photoswitched and read out for PALM imaging of pamCherry1-labeled RNA-polymerase in *E. coli* or, **c**, photoswitched in *d*STORM experiments.

beled with four different dyes. These were excited using four different wavelengths emitted by an Argon-Krypton laser. Furthermore, fluorescent proteins and organic dyes can be photoswitched and simultaneously read out for PALM or *d*STORM: Using a 405 nm laser for subsequent photoswitching and a 561 nm laser for excitation of pamCherry1-labeled RNA-polymerase in *E. coli* on the waveguide can be used to reconstruct a super-resolved PALM image (Figure 3.4b). Furthermore, Figure 3.4c shows that activation of the 488 nm laser line helps switching the membrane dye CellMask Deep Red back to its fluorescent state that is excited by a 660 nm laser in a *d*STORM experiment.

3.2.4. Multi-modal behavior of wide waveguides

The wide waveguides are highly multi-modal as their widths considerably exceed the wavelengths of the guided light. For instance, about 184 modes can be excited in theory in a 25 µm wide strip waveguide for light of a vacuum wavelength of 488 nm (Figure 2.6c). Back reflections and multi-mode interference cause a spatially stable distribution of laterally non-uniform evanescent fields, which strongly depends on the coupling into the waveguide. Accordingly, fluorescence excitation is inhomogeneous and, hence, impairs the fluorescence images (Figure 3.5a,b). To counteract this problem, a piezo stage is used to oscillate the coupling objective lens or fiber back and forth along the input facet of the waveguide during the measurement. This maintains continuous coupling but shifts the mode pattern to obtain an average distribution which shows significantly less modulation over larger length scales as compared to conventional TIRF setups. Diffraction limited images can thus be generated by acquiring multiple frames while the input is oscillated and subsequent temporally averaging multiple frames (Figure 3.5c). Similarly, oscillating the input during a *d*STORM measurement averages the pattern (Figure 3.5d). In contrast, keeping the pattern static and using *d*STORM to image a dye surface allows to measure the pattern. Figure 3.6 shows the result of this measurement. The pattern contains many coarse structures which widths is above the diffraction limit. However, the FWHM of the finest structures is as small as 140 nm and therefore well below the diffraction limit.

However, oscillating the input is not the only possibility to attenuate the effect of the multi-mode excitation. The use of a rotating diffuser in combination with a telescope creates a partially coherent illumination source of adjustable extend [51]. The diffuser is rotated at considerably higher frequency than the single frame exposure time which creates a fast changing speckle pattern. This is propagated along

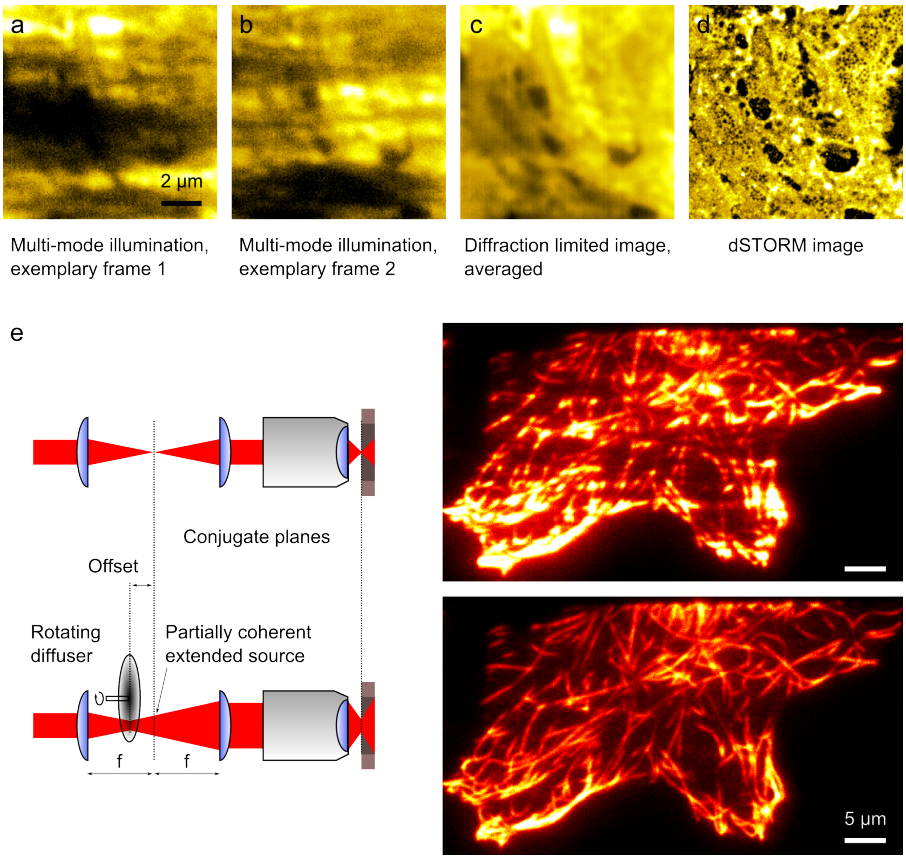

Figure 3.5.: **a**, **b**, The use of wide waveguides ($25\,\mu m$ to $500\,\mu m$) results in multi-mode excitation patterns that cause a laterally inhomogeneous evanescent field. Consequently, fluorescence excitation is non-uniform and the shape of the multimode pattern masks the imaged structures. Oscillating the coupling objective in ranges that still maintain coupling leads to a movement of the multimode pattern, allowing to correct for the non-uniform excitation by averaging over multiple frames. Subfigure **c** shows the result from averaging over 61 frames and represents a diffraction limited image of the labeled structure. **d**, During *d*STORM imaging, the coupling objective lens is also oscillated. Accordingly, the pattern is not visible in the super-resolved reconstruction of an LSEC membrane. **e**, Adding a rotating diffuser in combination with a telescope to the illumination unit creates a virtual light source of partial coherence that is imaged to the input facet. As the diffuser is rotated at considerable higher rate than the single frame exposure time, effectively flat illumination can be achieved. Hence, the visibility of the multi-mode pattern vanishes. This is shown for single frames without (upper row) and with (lower row) the use of the rotating diffuser for immunostained tubulin in U2OS cells.

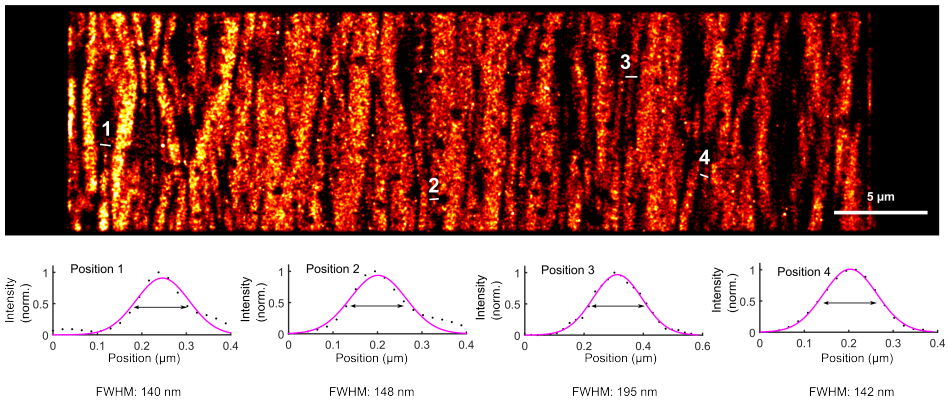

Figure 3.6.: The multi-mode interference pattern of a strip waveguide running in vertical direction is imaged using *d*STORM. A surface of Alexa 647 dye molecules was prepared on top of the waveguide and a *d*STORM image was acquired visualizing the instant lateral field-distribution of the evanescent field. Interference fringes show structures of FWHM as small as 140 nm as seen in the line profiles.

the offset distance between the diffuser and the shared focal planes of the telescope lenses and then imaged by the second telescope lens and the coupling objective onto the input facet. Figure 3.5e illustrates the principle and shows a comparison of single frames without and with the use of the rotating diffuser, respectively. The effect of the multi-mode pattern is not noticeable in the latter case.

When using the diffuser, it is not necessary to average over multiple frames to create one image with effective flat illumination in contrast to oscillating the input. This can increase the temporal resolution to the exposure time of a single camera frame. Thus, the bound for the temporal resolution, e.g. for live-cell imaging, is not defined by the use of (multi-modal) waveguides, but the detector. Therefore, it does not differ from other approaches to widefield fluorescence microscopy in this aspect.

The diffuser creates an extended virtual light-source remarkably bigger than a diffraction limited spot when imaged to the input facet. As the height of the waveguides used in this work is 150 nm to 220 nm, a major part of the light is not coupled into the waveguide in this case which decreases the coupling efficiency. In turn, a lower intensity in the evanescent field can be achieved which can be disadvantageous for the photoswitching process, e.g. in *d*STORM. For this reason, the diffuser was not used, but the input was oscillated for the experiments presented in the following.

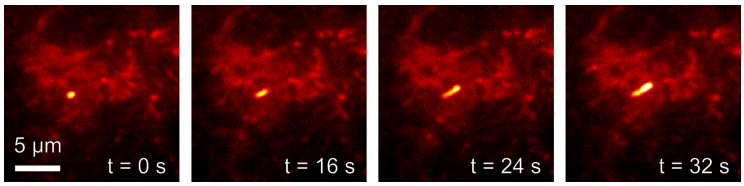

Figure 3.7.: A time series of mitochondrial dynamics in MCC13 cells on the waveguide demonstrates the live-cell imaging feasability.

3.2.5. Live-cell imaging capability

As the chips are made from glass, high biocompatibility is provided and established protocols for cell seeding onto common coverslips can be used [189]. Accordingly, cells can be grown on the waveguide and then fixed as has been done for most of the examples presented here. Nevertheless, it is also possible to perform live-cell imaging as shown in Figure 3.7. MCC13 cells were given time to attach to the chip and then incubated for 30 minutes with MitoTracker Deep Red directly before imaging. Mitochondrial dynamics can be observed in a series of images. In order to average the multi-mode pattern, a relatively long single frame exposure time of 2 s was chosen while the input was continuously oscillated. Furthermore, low intensity ($I \leq 0.01\ \frac{\mathrm{kW}}{\mathrm{cm}^2}$) was used for fluorescence excitation in order not to perturb the live cells. Accordingly, the multi-mode excitation pattern is not visible in the images, but this resulted in a low signal-to-noise ratio (SNR) and the temporal resolution is not better than 2 s. As discussed above, higher temporal resolution could be achieved using the diffuser instead of oscillating the input.

3.3. Chip-based dSTORM

Though waveguide chips have been used for fluorescence microscopy earlier [3, 4, 76, 184], this has so far been restricted to the diffraction limited case. The extension to super-resolution imaging is presented and characterized in the following.

3.3.1. Imaging with high magnification/ high NA

The feasibility of waveguide-based *d*STORM is demonstrated by the imaging of immunostained microtubules in rat LSECs on the waveguide chip as shown in Figure 3.8. In general, microtubules show a cylindrical structure of about 25 nm

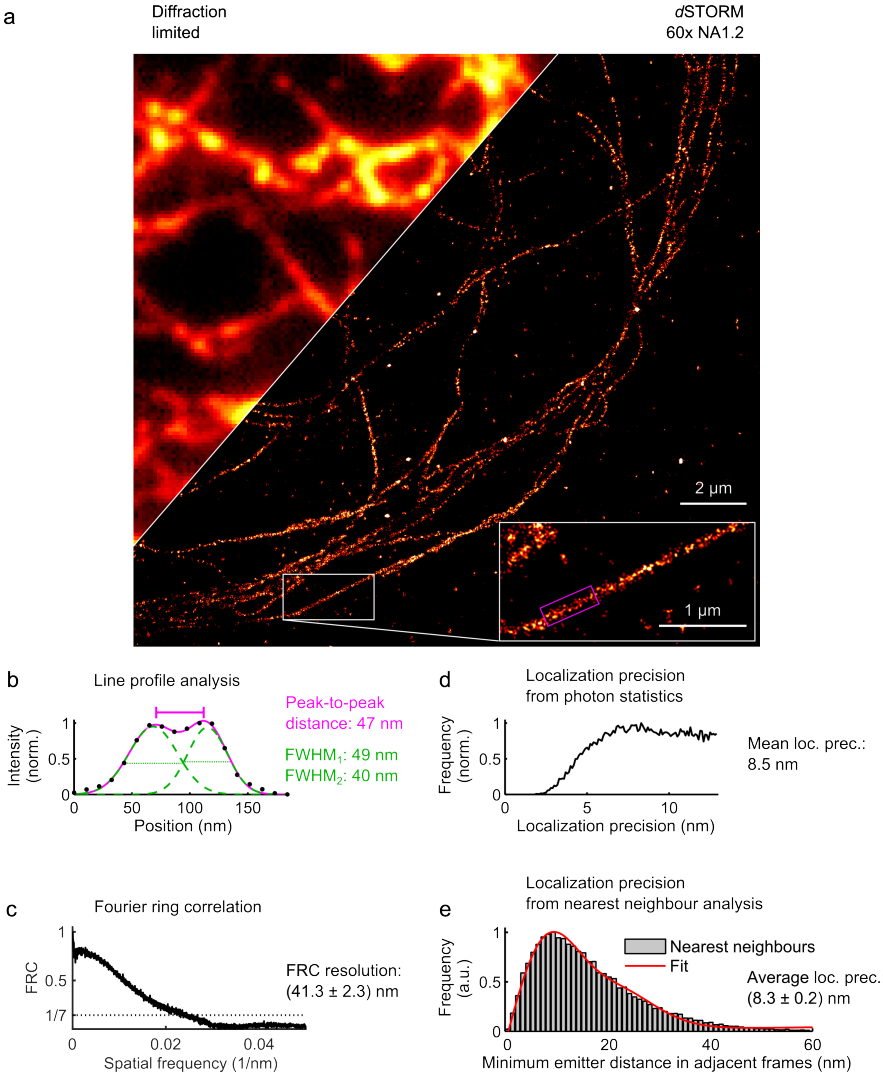

Figure 3.8.: Imaging immunostained tubulin in LSECs on the waveguide chip. **a**, The comparison between the diffraction limited image and the *d*STORM reconstruction shows the enhanced resolution. **b**, The line profile across a straight microtubule filament reveals that a resolution of better than $50\,\mathrm{nm}$ was obtained. This is also confirmed by fitting the sum of two Gaussian functions with FHWM values below $50\,\mathrm{nm}$ each to the cross section. **c**, In agreement with this result, the FRC resolution of the *d*STORM image is on the order of $40\,\mathrm{nm}$. **d**,**e**, The use of two different methods to estimate the localization precision reports a value of about $9\,\mathrm{nm}$. Note that the localizations were filtered for values better than $13\,\mathrm{nm}$.

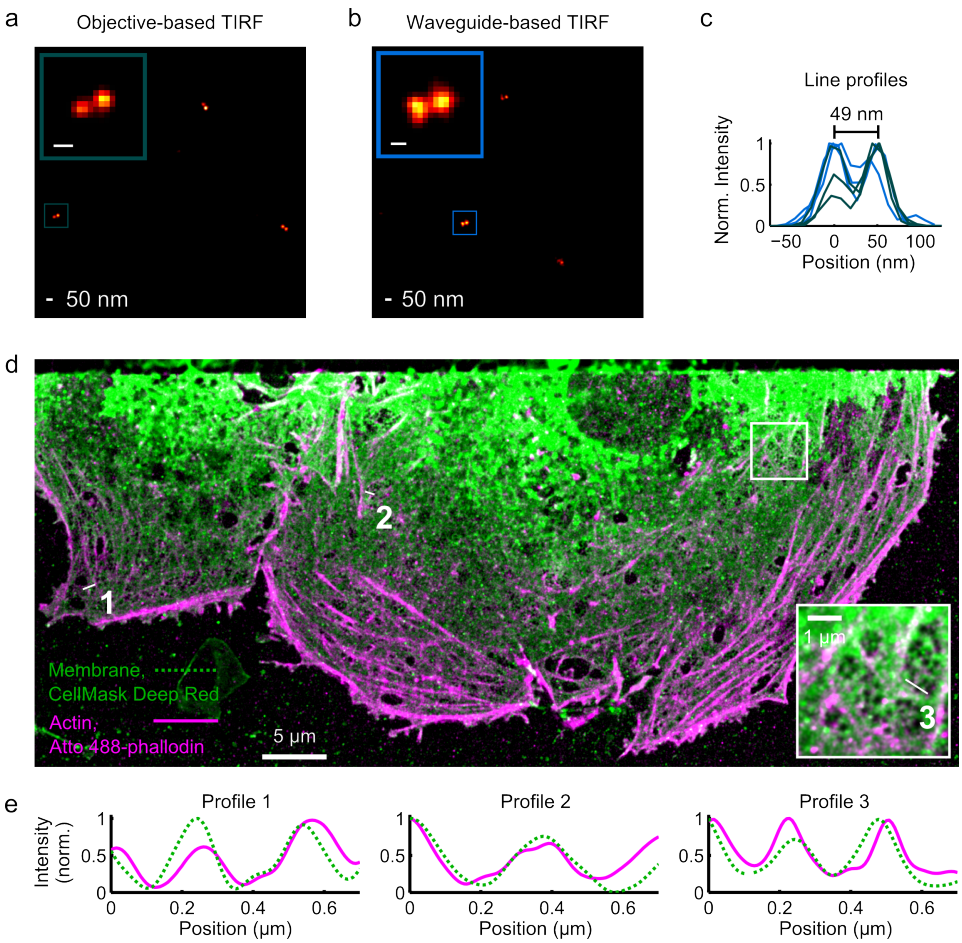

Figure 3.9.: **a**,**b**, The resolution capability of waveguide-based *d*STORM is investigated by imaging DNA-origami nanorulers of $(50 \pm 5)\,\mathrm{nm}$ specified length that can be clearly resolved similar to objective-based TIRF *d*STORM. **c**, Analyzing their line profiles, a mean nanoruler length of $49\,\mathrm{nm}$ is found in both cases affirming that the waveguide-based implementation shows comparable performance to a conventional inverted setup at a resolution of at least $50\,\mathrm{nm}$. **d**, Multi-color waveguide-based *d*STORM reveals the interplay between actin (magenta) and the membrane (green) in LSECs. Groups of fenestrations form sieve plate superstructures which are surrounded by thicker actin bundles. As can be seen in the inset, actin is present between neighboring fenestrations where it colocalizes with the plasma membrane. **e**, The line profiles taken at different positions in the liver cell underline the visual impressions of colocalization.

diameter [214, 77] that is extended by twice the effective length of the primary and secondary antibodies that decorate this cytoskeleton component by respective immunostaining [147]. Revealing this hollow structure in line profiles across a length along a straight microtubule filament has evolved into a resolution benchmark in localization microscopy [147, 206, 56, 25, 148]. Two-dimensional *d*STORM images show a projection of the three-dimensional emitter positions in a volume around the focal plane. A circular structure perpendicular to the focal plane will therefore show two distinct features provided sufficiently high resolution [25]. In case of the presented waveguide-based *d*STORM image, the two features at 47 nm distance are resolved, indicating an obtained resolution better than 50 nm. This is confirmed by an FRC resolution of (41.3 ± 2.3) nm. Estimates of the localization precision either directly from the individual localizations' photon statistics [149] or from the coordinates table [56] give a mean localization precision of 8.5 nm and an average localization precision of (8.3 ± 0.2) nm.

The resolution capability of waveguide-based *d*STORM is further investigated by comparing it to the widely used architecture of an objective-based TIRF setup. Commercially available DNA-origami-based [167] nanorulers that provide dyes spaced at a specified distance of (50 ± 5) nm were imaged. Figure 3.9a-c shows that those can be resolved and a mean distance of 49 nm was found for both microscopes.

High magnification/ high NA *d*STORM imaging on the waveguide was applied to visualize the interplay between the cytoskeleton component actin and membrane fenestrations in liver sinusoidal endothelial cells (LSECs) (Figure 3.9d). These cells contain multiple trans-cytoplasmic pores, termed fenestrations, of about 50 nm to 200 nm diameter, just below the resolution limit of traditional light microscopes. Fenestrations typically form superstructures of so-called sieve plates, refering to the cells' function as a molecular sieve in the liver between the blood vessels and the hepatocytes. Multi-color waveguide-based *d*STORM shows that small actin filaments colocalize with the membrane supporting the individual fenestrations (Figure 3.9e), reinforcing earlier findings with different methods [27, 137]. Thicker actin bundles surround multiple fenestrations forming sieve plates. It has been demonstrated that sieve plates are also surrounded by tubulin [137]. This suggests that sieve plates might have a combined actin and tubulin outer framework.

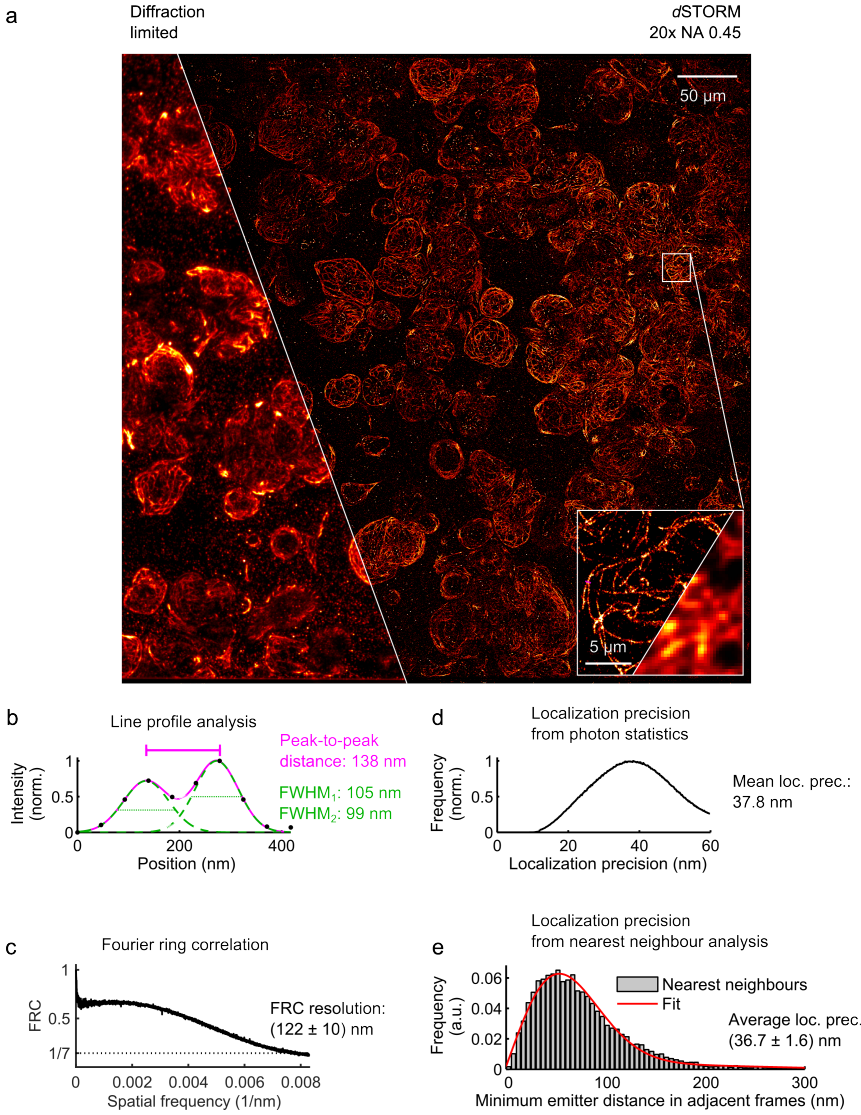

Figure 3.10.: **a**, Waveguide chip-based illumination allows for using a $20\times/$ NA 0.45 objective lens enabling *d*STORM imaging over a FOV of $500\,\mu\mathrm{m} \times 500\,\mu\mathrm{m}$. **b**, The profile over adjacent tubulin filaments reveals their separation by $138\,\mathrm{nm}$. **c**, The resolution better than $140\,\mathrm{nm}$ is confirmed by the FWHM values of two fitted Gaussian functions as well as a FRC resolution of about $122\,\mathrm{nm}$. **d**,**e**, This is further verified by the mean precision estimations. The nearest neighbor analysis was conducted on a ROI of $90\,\mu\mathrm{m} \times 72\,\mu\mathrm{m}$ size including the line profile of (**b**). Note that the localizations were filtered for localization precisions better than $60\,\mathrm{nm}$.

3.3.2. Imaging with low magnification/ low NA

The results presented in the previous section confirm the applicability of waveguides to provide TIRF-like excitation for *d*STORM imaging with comparable quality to conventional objective-based TIRF. However, it is a great advantage that the fluorescence excitation is independent of the detection objective lens in waveguide-based imaging. Hence, the geometry of the excited region is not restricted by the objective lens and can be made almost arbitrarily wide by adjusting the waveguide design.

Objective-based TIRF is restricted to high NA lenses that usually feature a high magnification and therefore restrict the field-of-view (FOV) size. In contrast, waveguide-based *d*STORM can be performed also with low NA/ low magnification lenses. For epi-illumination, *d*STORM imaging over a FOV of 100 µm side length has recently been demonstrated by free-space beam shaping [51] and of 221 µm side length by fiber-based shaping [228], but still utilizing high-NA lenses. Using a 20×/ NA 0.45 objective lens and waveguide-based excitation, *d*STORM imaging over a FOV of 500 µm side length can be demonstrated (Figure 3.10), outperforming the recently demonstrated FOV areas by more than a factor of four. However, the achieved localization precision under these imaging conditions of about 37 nm (Figure 3.10d,e) is notably worse than in high NA imaging (Figure 3.8). Consequently, the FRC resolution of 122 nm is worse by about a factor of three. Hence, a low NA/ low magnification lens means that FOV size is traded for resolution.

3.4. Fluctuation-based imaging

3.4.1. Dynamic multi-mode excitation enables resolution enhancement

The presented *d*STORM images on the waveguide are taken while oscillating the coupling beam along the input facet in order to average the illumination pattern. However, fluctuations induced by the shifted mode pattern can be explicitly harnessed for chip-based fluctuation super-resolution imaging, a different approach to resolution enhancement. Although original implementations of the fluctuation-based approaches SOFI [41] and ESI [222] use intrinsic quantum dot or fluorophore temporal intensity fluctuations (e.g. due to blinking and bleaching), it has been shown that speckle pattern illumination [207] can also invoke temporal emission fluctuations allowing for super-resolved fluctuation imaging [116].

Intrinsic intensity fluctuations originate from single emitters and therefore spatially tightly confined sources. On the contrary, the spatial frequencies of the waveguide illumination pattern will presumably define the length scales on which the fluctuations occur, and, hence, the obtainable resolution. By theory, the lowest bound for possible fringe sizes resulting from mode interference is found for counterpropagating coherent waves. This results in an intensity pattern in the form of a standing wave with half of the wavelength of the light wave. If the fringe size is expressed by a FWHM value, it is half of the wavelength of the wave forming the intensity pattern, i.e. one quarter of the wavelength of the interfering light. Related to the waveguide, the smallest possible value for the structure FWHM of the interference fringes is given by $\mathrm{FWHM}_{\mathrm{min}} = \frac{\lambda}{4n_{\mathrm{eff}}}$, which results in 97 nm assuming a vacuum wavelength of $\lambda = 660\,\mathrm{nm}$ and an effective refractive index of $n_{\mathrm{eff}} = 1.7$ inside the waveguide. The dSTORM measurement of the pattern (Figure 3.6) shows fringe sizes as small as 140 nm, which is about 44% higher than the theoretically possible minimum fringe size. It is reasonable that the fringe size does not go down to the lowest possible value as the pattern results from the interference between multiple modes which are propagating in the same direction inside the waveguide and not from counterpropagating waves.

3.4.2. Simulation predicts increased resolution in waveguide-based ESI

The measured fringe sizes were used to model the image formation in waveguide-based ESI for emitter pairs at different distances. Their subsequent illumination was simulated by sinusoidal patterns with random phases and random FHWM fringe sizes equally distributed between the experimentally obtained lowest value of 140 nm and an upper value of 420 nm. The fluorescent response of emitter pairs at different distances was modeled by assuming a linear response to the illumination, i.e. taking the respective illumination intensity at the emitters' positions as the fluorescent response in each frame. This signal was convolved with a Gaussian-shaped PSF and afterwards scaled down to a grid with pixel widths and heights of 75.9 nm. Shot noise was modeled as Poisson noise and the signal was converted from counts to photoelectrons at 0.42 photoelectrons per count at a maximum of 500 photoelectrons per pixel. To consider additional camera noise and inhomogeneities in terms of noise and offset pixel-to-pixel variations, 200 frames were recorded using the sCMOS camera with no illumination on the detector and these were added to the modeled frames.

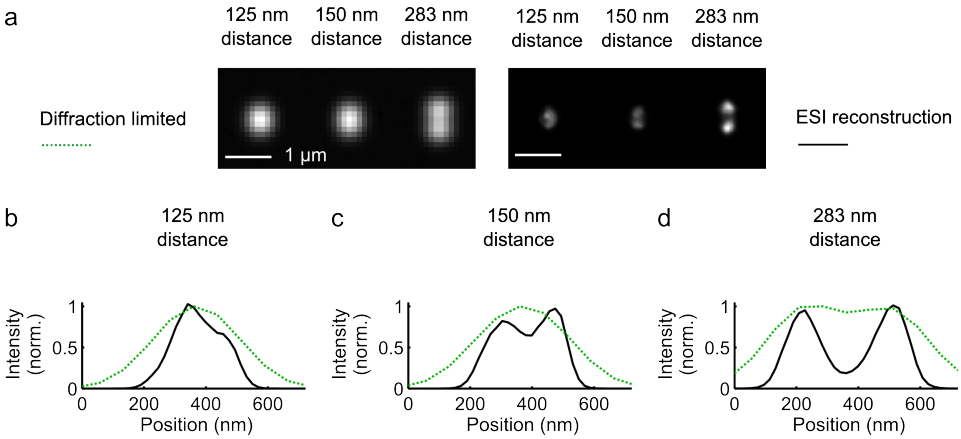

Figure 3.11.: Simulation of chip-based ESI. Random phase sinusoidal illumination patterns were modeled with random fringe widths comparable to the measured values exciting emitter pairs at different distances. **a**, The average signal over 200 frames shows that two emitters at the diffraction limit of 283 nm distance are just resolved (**d**), while emitters at 150 nm (**c**) and 125 nm (**b**) are not resolved. The ESI reconstruction results in a separation of the emitters at 150 nm distance (**c**), while the emitters at 125 nm distance are not separated (**b**), but the emitters at 283 nm distance become more clearly separated (**d**).

Analyzing the simulated data from 200 frames with ESI shows that two emitters spaced by the diffraction limit are easily resolved (Figure 3.11). This also applies to emitters spaced by 150 nm which is well below the diffraction limit while closer emitters at 125 nm spacing are not resolved. This gives a ratio of about 1.3 between the smallest possible illumination pattern fringe spacing from 660 nm vacuum wavelength of $\frac{\lambda}{2n_{\text{eff}}} = \frac{660\,\text{nm}}{3.4} = 194\,\text{nm}$ and the achieved resolution of 150 nm.

3.4.3. Experimental validation

Alexa 488-immunostained tubulin in rat LSECs plated on the waveguide was used to experimentally evaluate the obtainable resolution with waveguide-based ESI. A stack of 202 frames was recorded while oscillating the input. Taking the temporal average yields the diffraction limited image of the structure (Figure 3.12b), but analyzing the stack with the ESI algorithm leads to a super-resolved reconstruction (Figure 3.12a). As random intensity fluctuations are desired, there is no need to further control the illumination pattern besides changing it from frame to frame.

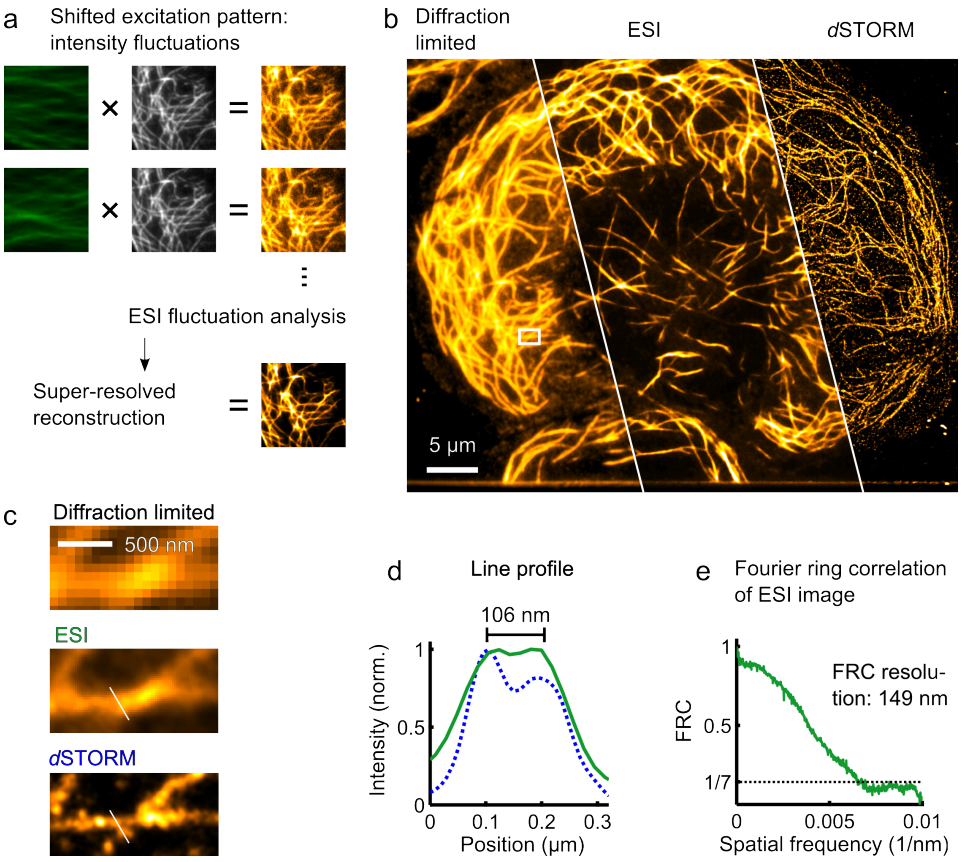

Figure 3.12.: **a**, Fluorescence intensity fluctuations are induced by changing the mode pattern of the waveguide during image acquisition. Accordingly, these measurements show diffraction limited images of the labeled structure multiplied by the mode pattern. A stack of about 200 frames is used as input data for the fluctuation analysis reconstruction algorithm, resulting in one super-resolved image. **b**, Imaging tubulin in an LSEC. The comparison of the diffraction limited image, the corresponding ESI reconstruction, and the *d*STORM image shows the gradually increasing resolution. Subfigure **c** shows a magnification of the same region (indicated by the rectangle in **b**) for the three different imaging modalities. The *d*STORM image of the same structure verifies the applicability of chip-based ESI: the line profiles reveal a distance of $106\,\mathrm{nm}$ that is just resolved for chip-based ESI (green line) by imaging two adjacent microtubules, simultaneously observed in the *d*STORM image (blue dashed line) (**d**). **e**, Fourier ring correlation of the entire ESI image reports a resolution of $149\,\mathrm{nm}$.

Low input power was used, keeping the intensity under the threshold of undesired single molecule switching, contrary to the *d*STORM acquisition procedure where single molecule switching is required. Afterwards, the illumination intensity was significantly increased which led to photoswitching of the dye under the employed buffer conditions and raw data of the blinking was recorded over 30 041 frames. A *d*STORM reconstruction of this data leads to further increased resolution and can be used to verify that the structures observed in the ESI reconstruction are not artifacts.

Analyzing the line profile of adjacent tubulin filaments (Figure 3.12c) shows that structures at 106 nm can still be resolved in the ESI image. This fits the prediction of a 1.3 resolution enhancement compared to the smallest pattern fringe spacing of $\frac{\lambda}{2n_{\text{eff}}} = \frac{488\,\text{nm}}{3.4} = 144\,\text{nm}$.

Splitting the stack into two halves before reconstructing it allows to run an FRC analysis on the ESI data similar to localization microscopy data. The reported FRC resolution is 149 nm. This corresponds to a resolution enhancement by a factor of 1.47. Anyway, the value found by FRC is about 41% higher than the maximally observed resolution of 106 nm.

The deviation between the FRC resolution for the entire image and the smallest observed structures gives rise to the assumption that the resolution in waveguide-based ESI is either not isotropic or not homogeneous or both. It seems reasonable to assume anisotropy because the multi-mode interference mostly occurs perpendicular to the propagation direction (Figure 3.6). Thus, fluctuations on smallest length scales only occur in one direction and will lead to the biggest resolution enhancement in this direction. Furthermore, the shape of the mode pattern depends on the waveguide quality. Irregularities, e.g. by varying sidewall roughness, can lead to patterns with inhomogeneous properties. This problem could be circumvented by manufacturing waveguides of different layout that lead to periodic interference patterns. For instance, structures could be used that result in counterpropagating waves. If only the fundamental mode of the waveguide would be excited and interference could be realized subsequently under different angles, a quasi-isotropic and homogeneous resolution enhancement might be achieved. Such a defined illumination could also enable different approaches to resolution enhancement, for instance structured illumination microscopy [87, 80]. However, manufacturing such waveguide structures can be a challenging task.

In contrast, a big advantage of the presented chip-based ESI is that the fluctuations do not need to be controlled and the multi-mode interference is an intrinsic property of the utilized waveguides. Compared to *d*STORM, ESI needs signifi-

cantly less frames for the reconstruction of a super-resolved image as well as lower illumination intensities, thus, it might also enable live-cell imaging.

3.5. High throughput localization microscopy

3.5.1. Waveguide-based imaging compared to mosaic stitching

Waveguide chip-based imaging has the potential to increase the throughput not only for fluctuation-based imaging, but also in SMLM by its almost arbitrarily large FOV. Comparing it to what has been experimentally achieved via mosaic stitching, it is possible to find a dramatic increase in throughput: Figure 3.10 shows *d*STORM imaging at approximately 140 nm resolution over a FOV of 500 µm × 500 µm that has been reconstructed from 21 716 raw frames recorded in approximately 18 minutes.

Circumventing the need for modifying the illumination scheme, the FOV in SMLM can also be extended via stitching of multiple areas as it has recently been demonstrated by Nahidiazar et al. [139]. The authors show that the stitching of eight regions resulted in the *d*STORM image of an almost entire HUVEC cell. For each region, 20 000 raw frames at 100 frames per second (fps) had been recorded on a commercial setup. Hence, 160 000 raw frames recorded in approximately 26 minutes and subsequent stitching were necessary for the *d*STORM reconstruction of the entire cell. Though the authors do not give an estimated resolution for this example, it should be assumed that the obtained resolution is much better than 140 nm. Nevertheless, using the waveguide-based approach and accepting a worse resolution that is still well beyond the diffraction limit, more than 50 cells compared to one cell could be imaged in approximately 18 minutes compared to 26 minutes, corresponding to a 72-fold increase in throughput.

3.5.2. Tradeoff between high localization density and low emitter density

However, it needs to be considered that the increase in throughput does not scale linearly with the FOV size, but additional effects need to be taken into account: The Nyquist sampling theorem demands a high localization density to achieve a certain resolution in SMLM [121, 169] that will be discussed in detail in section 3.7. In contrast, the density of active emitters during data acquisition needs to be low enough such that the overlap of their central PSF is prevented, i.e. there is only

little chance for the central PSF of one emitter to overlap with another due to the stochastic process of blinking, respectively. Overlapping of the central PSF renders the fitting algorithm unable to correctly localize the the individual emitters' positions and, thus, leads to false localizations.

3.5.3. Tolerable emitter density upper bound

The upper bound for simultaneously active emitters can be estimated by assuming the PSF as circles with a radius r that are hexagonally close packed on a 2D lattice [30]. Hence, the packing density is $\eta = \frac{\pi}{2\sqrt{3}} = 0.9069$. Choosing the radius as the distance defined by the Rayleigh criterion, i.e. $r = \frac{1.22\lambda}{2\mathrm{NA}}$, ensures that the individual emitters can be spatially separated, though the exact distance depends on multiple factors such as the signal to noise ratio of the particular measurement, or the ability of the localization algorithm to segment individual emitters. For instance, high density reconstruction algorithms have been demonstrated, e.g. based on compressive sensing [230] or machine learning [15], but suffer from limited localization precision and accuracy.

The maximum density ρ of simultaneously active emitters is

$$\rho = \frac{\eta}{\pi r^2}, \tag{3.1}$$

which becomes

$$\rho = \frac{1}{2\sqrt{3}} \frac{4\,\mathrm{NA}^2}{1.22^2\,\lambda^2} = 0.776\,\frac{\mathrm{NA}^2}{\lambda^2}, \tag{3.2}$$

when using Rayleigh's criterion. If a localization density M is desired (cf. section 3.7), at least $\frac{M}{\rho} \propto \mathrm{NA}^{-2}$ single frames of raw data need to be recorded. Hence, the number of frames to achieve a particular localization density scales with NA^{-2}, provided only the blinking density changes and other factors are constant. When changing from NA = 1.2 (cf. Figure 3.8) to NA = 0.45 (cf. Figure 3.10), the necessary number of frames increases by a factor of about 7.1 in order to keep the localization density constant. At the same time, the optical magnification in this example has changed from 60× to 20×, leading to a nine-fold increase in the FOV when using the same camera detector. Hence, the throughput in this case is only increased by 27%, comparing single FOV imaging to 3 × 3 mosaic stitching for the same effective FOV.

3.5.4. Overlap probability in stochastic photoswitching

This consideration assumes closely packed emitters on a periodic grid. As the locations of active emitters are independent of each other and randomly distributed, dense packing without overlap is unlikely to occur in a localization microscopy experiment, but overlap of active emitters by their PSF will occur at a certain probability depending on the labeling density, photoswitching properties, and PSF size [205]. Assuming the area of a diffraction limited spot as $D = \pi r^2$ and the overall imaged area A, the probability for one specific emitter to overlap with a second emitter is given by $\frac{D}{A}$. Hence the probability for no overlap with a second emitter follows as $1 - \frac{D}{A}$ and for no overlap with k other emitters as $\left(1 - \frac{D}{A}\right)^k$. Consequently, the probability p for one specific emitter to overlap with any other emitter in case of $m = k + 1$ simultaneously active emitters is given by

$$p = 1 - \left(1 - \frac{D}{A}\right)^{m-1} = 1 - \left(1 - \frac{\pi}{A}\left(\frac{1.22\,\lambda}{2\,\mathrm{NA}}\right)^2\right)^{m-1}, \tag{3.3}$$

when again taking Rayleigh's criterion into account.

Overlapping PSFs can lead to false localizations, and therefore affect the quality of the reconstructed image. For experiments, it is usually $p > 0$, because PSFs are of finite extend ($D > 0$) and two or more emitters are simultaneously active ($m > 1$). Accordingly, overlap of PSFs cannot be prevented. The design of the experiment must thus be made in the way to find an acceptable tradeoff between the emitter density and the necessary number of frames to achieve a certain localization density. For instance, the illumination intensity of the excitation and photoswitching lasers, the buffer conditions, and the single frame exposure time can be varied, but the interplay between these parameters and their impact on the resulting image is not trivial [127].

3.5.5. Using high NA favors high throughput

The overlap probability as a function of the numerical aperture and the emitter density on a FOV area of $500\,\mu\mathrm{m} \times 500\,\mu\mathrm{m}$ and for an emission wavelength of 670 nm is plotted in Figure 3.13a. Despite the nonlinear relation, the ratio between the emitter density that guarantees a specific overlap probability is almost constant between the different values of NA = 1.2 and NA = 0.45 for different emitter densities (Figure 3.13b). Similar to the rough estimation based on close packing,

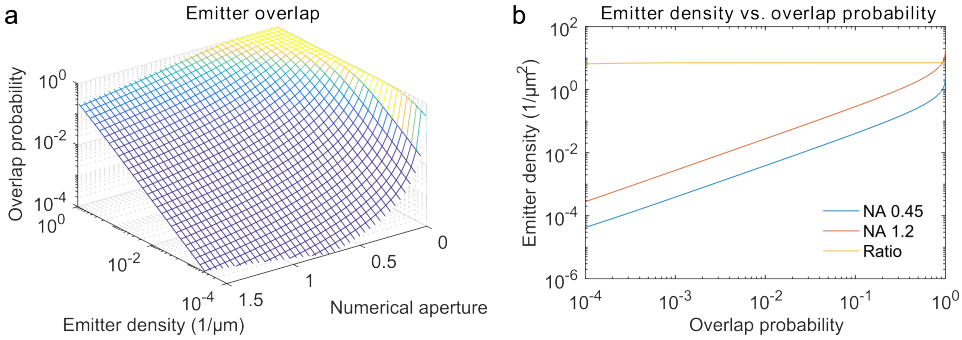

Figure 3.13.: a, The relationship between the density of simultaneously active emitters, the numerical aperture, and the probability of one emitter to overlap with another. **b**, Though the emitter density to achieve a particular probability differs significantly between NA 1.2 and NA 0.45, the ratio is almost constant about 7.1 for all probabilities.

this ratio is about 7.1, i.e. the number of necessary frames to achieve a certain resolution increases by this value.

These results reveal that when looking at the aspect of localization density from a theoretical perspective, the throughput can only be increased by about 27% by waveguide-based imaging when changing from a 60×/ NA 1.2 to a 20×/ NA 0.45 lens. However, there are also lenses with 20× magnification and higher NA commercially available, e.g. NA 0.7. Using such a lens, the emitter density would only need to be decreased by a factor of approximately 2.9 in comparison to 60×/ NA 1.2. Taken together with the FOV increase by a factor of 9, the throughput with this lens could be increased by about 210% provided the blinking density can be controlled accordingly. Nevertheless, it needs to be taken into account that the localization precision decreases significantly when imaging with a lower NA. This relaxes the demands on the localization density as it also restricts the achievable resolution which will be evaluated in the following.

3.6. NA-dependent localization precision

3.6.1. Influence on PSF width and light collection efficiency

The obtainable localization precision strongly depends on the NA of the utilized objective lens due to mainly two factors (cf. section 2.4): The light collecting capability decreases as the NA decreases because light emitted into a smaller solid

angle is collected by the lens. Furthermore, the NA determines the width σ of the PSF. A wider PSF also leads to a decreased localization precision.

The dependence of σ on the utilized NA can be easily found by approximating the Airy-Function of an in-focus PSF by a Gaussian function. In this case, the Rayleigh distance corresponds well to the FWHM of the Gaussian function. Hence, the standard deviation characterizing the PSF width can be written as

$$\sigma = \frac{1}{2\sqrt{2\ln 2}}\mathrm{FWHM} \approx \frac{1}{2\sqrt{2\ln 2}}\frac{1.22\,\lambda}{2\,\mathrm{NA}} \approx 0.259\,\frac{\lambda}{\mathrm{NA}}. \tag{3.4}$$

The relative light collection efficiency for different NAs can be derived via the relation between the NA and the corresponding solid angle. The numerical aperture is defined as $\mathrm{NA} = n_{\mathrm{med}} \sin\theta$, where n_{med} denotes the refractive index of the immersion medium or mounting medium, respectively, and θ denotes the half opening angle of the collected light cone. The solid angle Ω depends on θ by $\Omega = 4\pi \sin^2\left(\frac{\theta}{2}\right)$. Thus, the dependence of the light collection efficiency is given by

$$N \propto \Omega = 4\pi \sin^2\left(\frac{1}{2}\arcsin\left(\frac{\mathrm{NA}}{n_{\mathrm{med}}}\right)\right), \tag{3.5}$$

where N denotes the number of detected photons.

Both the original model of Thompson et al. [200] (equation (2.14)) and its updated version by Mortensen et al. [138] (equation (2.15)) for the localization precision depending on the statistics of the captured image of an emitter are widely used. A slightly adapted version of the latter is also implemented in ThunderSTORM [149], the software that is used for image reconstruction.

3.6.2. Model-based estimation

Utilizing the relations derived above, Figure 3.14a shows the theoretical prediction for the localization precision using either a high NA 1.2 water immersion lens or a low NA 0.4 air lens, calculated from both models. To compare the theory to experimental results, Atto 488-phalloidin stained Actin in LSECs was subsequently imaged with different objective lenses via *d*STORM on the waveguide chip (Figure 3.16). Crops of the reconstructed super-resolution images are shown in Figure 3.14d,e.

For calculations, experimentally achieved parameters for Atto 488 are used. These are a mean count of $N = 352$ photoelectrons per localization and a mean

standard deviation of the background of $b = 3.7$ photoelectrons for the NA 1.2 lens, and a mean count of $N = 135$ photoelectrons per localization and a mean standard deviation of the background of $b = 4.2$ photoelectrons for the NA 0.4 lens. Note that different photon count values might stem from different sources, e.g. a different single frame exposure time that was used for the measurements (40 ms for NA 1.2 and 160.84 ms for NA 0.4). The photon count values were extrapolated to other NA values by taking the light collection efficiency of the objective lens into account following equation (3.5). Assuming an emission wavelength of $\lambda = 523$ nm for Atto 488, the standard deviation σ of the fitted Gaussian-shaped PSF was calculated following equation (3.4). The backprojected pixel widths a were calculated by assuming a perfect match between the Nyquist sampling capacity of the camera and the resolution of the optical system considering the Abbe limit, i.e. $a = \frac{\lambda}{2\,\mathrm{NA}}\frac{1}{2\sqrt{2}}$.

Note that while this match is highly appreciated in diffraction-limited imaging, it is often not fulfilled for setups that only serve for SMLM imaging as adjusted backprojected pixel sizes may lead to better fitting results of single molecule emissions. However, this match is almost given for the waveguide setup: utilizing the NA 1.2 objective lens for Atto 488 imaging, the backprojected pixel width is $a = 75.9$ nm, while the Nyquist-optimal value is $a = 77.0$ nm. In case of NA 0.4, the used backprojected pixel width is $a = 228.3$ nm, while the Nyquist-optimal value is $a = 231.1$ nm. Thus, it is valid to extrapolate from the experimentally achieved results to other NA values under the assumption of Nyquist-sampling-matched projected pixel widths.

3.6.3. Different approaches estimate experimentally achieved precision

To compare to the theory, the experimentally achieved localization precisions are estimated in two different ways:

- Using the signal statistics of the captured image of each emitter in the raw data, the reconstruction software [149] assigns an estimated localization precision to all localizations. The mean value over all localizations for NA 1.2 and for NA 0.4 is drawn in grey in Figure 3.14a, considering the standard deviation as error intervals.
- Another approach to estimating the experimentally achieved average localization precision relies on computations on the distance to nearest neighbors of localizations in adjacent frames of the raw data as these possibly stem from the same molecule [56]. Because this assumption is not always fulfilled,

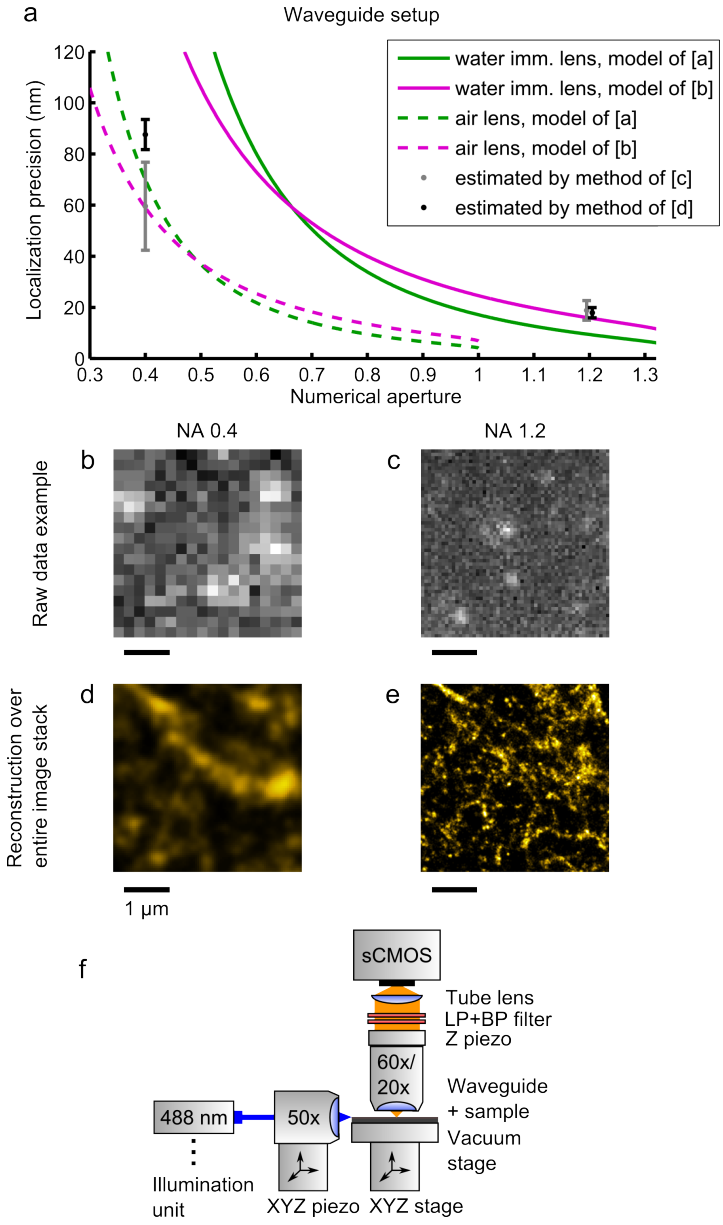

Figure 3.14.: **a**, Comparison of the experimentally achieved localization precision and the theoretical predictions for Atto 488 on the waveguide setup (**f**). **b**,**c**, show example raw data taken under different conditions and **d**,**e** show the corresponding reconstructed images for the entire stack of raw data. In this figure, the references are [a] = [200], [b] = [138], [c] = [149], [d] = [56].

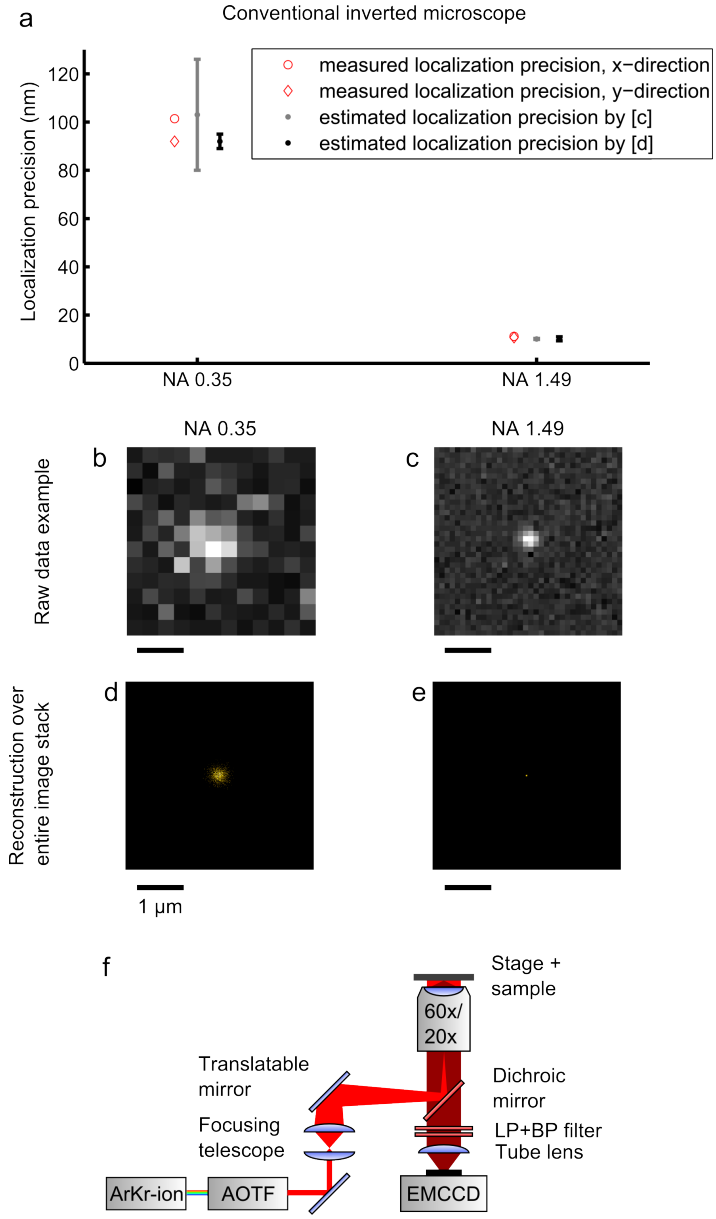

Figure 3.15.: a, Comparison of the experimentally achieved localization precision and the theoretical predictions for fluorescent beads on an conventional inverted microscope (**f**). **b**,**c**, show example raw data taken under different conditions and **d**,**e** show the corresponding reconstructed images for the entire stack of raw data. In this figure, the references are [c] = [149], [d] = [56].

correction terms are considered in the computation. Using the set of localizations from the entire image stack, the findings for the localization precision are drawn in black in Figure 3.14a. Please note that this methods is based solely on the localization coordinates and that it ignores the statistics on the raw data, i.e. photoelectron count, background etc.

Experimentally achieved localization precisions estimated by both methods and theoretical predictions fit in case of the NA 1.2 lens.

A strong deviation becomes apparent in case of the NA 0.4 lens being used. It is self-evident that the statistics of the localization precision computed by the reconstruction software [149] match the theoretical predictions of the model of Mortensen et al. [138] as they are based on the same assumptions, while the broad variance is possibly due to the low SNR in the raw data, of which Figure 3.14b shows an example. For comparison, Figure 3.14c shows an example of the raw data for the NA 1.2 lens being used, and Figure 3.14d and Figure 3.14e show reconstructions of the same FOV for the entire image stack.

3.6.4. Imaging sparse emitters shows agreement of both approaches

In contrast to the method that uses the individual localization photon statistics, the estimation by the method that purely uses the localization positions table results in significantly higher values for the localization precision. To investigate this, experiments were performed on a conventional inverted microscope configured for SMLM experiments (Figure 3.15). Fluorescent beads of 100 nm diameter at a low concentration served as the sample. This approach allows for the modeling of SMLM experiments with adjustable image statistics, particularly photon count values, comparable to the experiments on the waveguide by appropriately choosing excitation power and exposure times. Examples from the raw data are shown in Figure 3.15b and Figure 3.15c for the used objective lenses of NA 0.35 and NA 1.49, respectively.

As the beads do not blink, it was possible to localize them over a large number of frames (2 046 frames for NA 1.49 and 4 153 frames for NA 0.35), such that the localization precisions in x-direction (red circle in Figure 3.15a) and y-direction (red diamond) can be measured directly as the standard deviations of the localization distribution, shown in Figure 3.15d and Figure 3.15e. The comparison to the estimation by both methods shows good agreement with the directly measured values for both high and low NA lenses utilized. The higher value for the localization

precision in x-direction for the NA 0.35 case is possibly due to drift on the order of 10 nm during the experiment. Again, the localization precision values computed by reconstruction software show a broad variance, which is consistent with the findings on the waveguide. Inconsistently, the results show that in case of the low NA for the bead experiment (Figure 3.15a), the deviation between the estimation of the different methods is not given as in case of the waveguide experiment (Figure 3.14a). Taking the raw data in case of the low NA lens (Figure 3.14c) and the high NA lens (Figure 3.14d) on the waveguide into account shows that the emitter density looks comparable. However, the individual PSFs are much worse separated in case of the low NA simply due to the significantly larger PSF widths.

3.6.5. Disagreement between different approaches indicates high emitter densities

As discussed in section 3.5, the locations of the blinking dyes in a *d*STORM experiment are distributed stochastically. Wider PSFs increase the chances of overlapping PSFs which can lead to (i) a wrong emitter position estimation as a localization will be found in between the real positions of the multiple emitters, and (ii) a wrong estimation on the single emitter photon count as this will be based on the photon emission of the multiple emitters simultaneously. Equation (3.3) can be used to calculate the PSF overlap probability. For the *d*STORM image shown in Figure 3.16c, it is $A = 3.1 \cdot 10^4\,\mu\text{m}^2$, $\lambda = 523\,\text{nm}$, and NA $= 0.4$. The maximum number of simultaneously active emitters during the raw data acquisition is $m_{\text{max}} = 1,821$ while the mean number of simultaneously active emitters is $m_{\text{mean}} = 959$. It follows that for m_{max}, each emitter has the probability $p = 7.5\%$ to overlap with another emitter of, while for m_{mean}, the probability is $p = 4.0\%$. Note that this estimation is presumably underestimating the number of active emitters as overlapping PSFs are registered only once by the reconstruction algorithm.

This can now explain the deviation of the localization precision estimations by the two different methods considering their underlying principles: The method used by the reconstruction software performs an estimation of the precision for each localization on the statistics of the raw data independent of the complete reconstructed image. If an erroneous localization occurs due to overlapping PSFs of multiple emitters, this affects the quality of the reconstructed image but also the localization precision statistics. In contrast, the method using the nearest neighbor distances in subsequent frames performs computations only on the localization coordinate list that is used to render the super-resolved image. Hence, deviations

between the two methods can indicate the problem of too dense single molecule blinking in the raw data.

Due to the stochastic nature of the process, overlapping of the PSFs of multiple emitters cannot be fully avoided in *d*STORM. The probability can be decreased by tuning the experimental conditions, including the choice of an appropriate dye. Due to its relative good photostability [40], Atto 488 performs well for multiple subsequent acquisitions of the same sample that is used to compare between different modalities in the remainder. Nevertheless, the high ratio of fluorescence on-time to off-time leads to a relative high probability of overlapping PSFs [40]. Because of its blinking behaviour in terms of on/off ratio and number of emitted photons per on-event, Alexa 647 is often considered a better option if the focus is laid on *d*STORM imaging only. Consequently, a higher resolution in *d*STORM imaging can be achieved using the latter dye. This is confirmed by the very good agreement for the localization precisions determined by both methods for low and high NA chip-based *d*STORM imaging (Figure 3.10d,e and Figure 3.8d,e). Anyway, it is possible to achieve a resolution beyond the diffraction limit for low NA (0.4 and 0.45) lenses on the waveguide chip for both Atto 488 and Alexa 647, showing that waveguide-based *d*STORM allows for large FOV *d*STORM imaging in TIRF excitation.

3.7. Scaleable super-resolution imaging

3.7.1. Realization

As the evanescent field generation in waveguide-based imaging does not depend on the objective lens used for fluorescence detection, the presented approaches of chip-based *d*STORM and ESI can be applied for successive image acquisitions at different magnifications enabling scaleable FOV imaging: To obtain an overview image on a large FOV, low magnification/ low NA lenses can be used. If higher resolution is desired, specific regions of interest can be imaged at superior resolution afterwards via switching to a high magnification/ high NA objective lens.

To experimentally demonstrate the applicability of this strategy, Atto 488-stained actin in LSECs is imaged on the waveguide. Using a 20×/ NA 0.4 objective lens, 208 frames are acquired at a low illumination intensity. Their temporal average gives a diffraction limited image of multiple cells at once (Figure 3.16a). Using the same data as input for the ESI analysis yields a resolution enhanced image (Figure 3.16b) where neighboring actin filaments at 334 nm distance can already

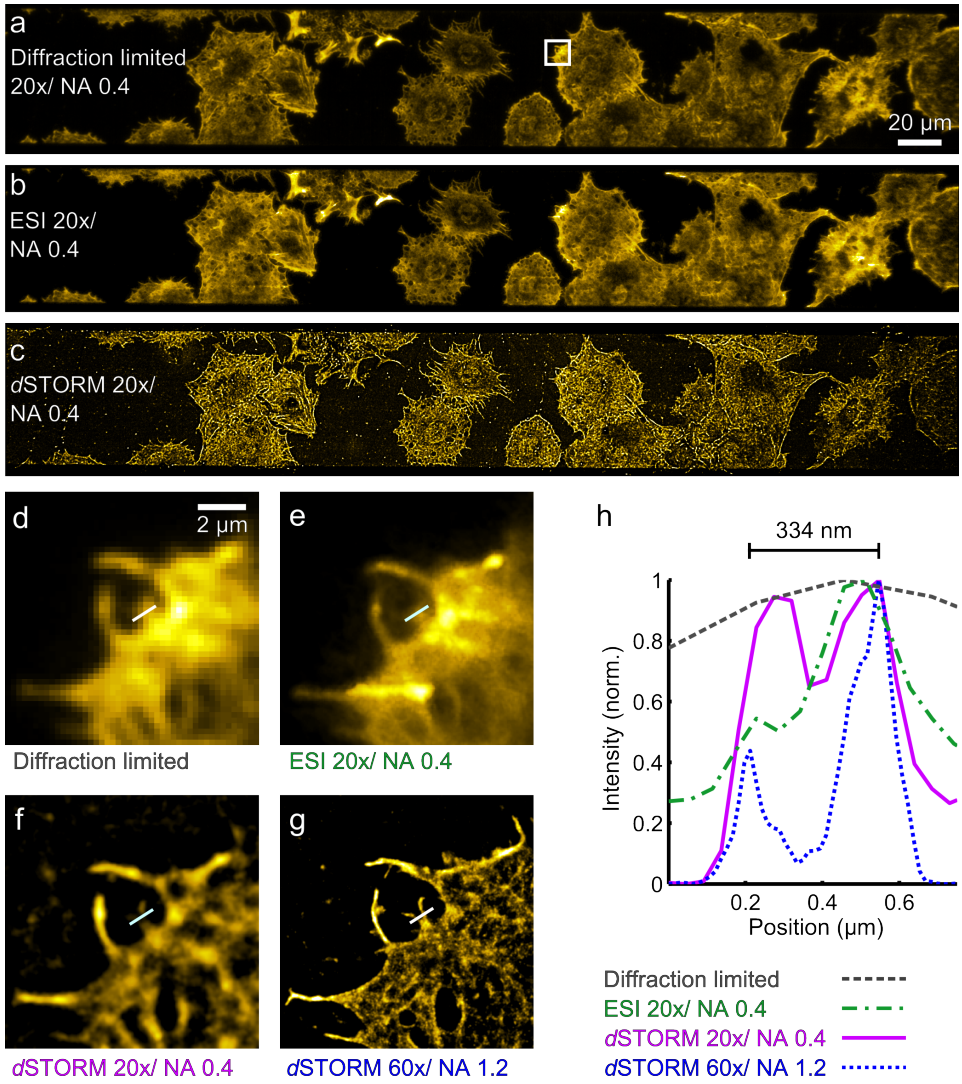

Figure 3.16.: Using a $20\times$ magnification objective lens allows for chip-based TIRF imaging over a field-of-view of $0.46\,\mathrm{mm}$ width (**a**,**d**). Both fluctuation-based ESI (**b**,**e**) and localization-based *d*STORM (**c**,**f**) result in an optical resolution enhancement obtained using the NA 0.4 lens, and, thus, resolve actin bundles at $334\,\mathrm{nm}$ distance (**h**). Hence, both techniques provide a tool for scanning large fields-of-view at high resolution to identify cells of interest that can be re-imaged using a high magnification/ high NA lens in a subsequent step (**g**), accomplishing even superior resolution. The choice between wide field-of-view ESI or *d*STORM can be made on either prioritizing short acquisition times (choosing ESI) or best resolution (choosing *d*STORM). **d**-**g** show a detail of the region marked by the box in **a**.

be separated (Figure 3.16h). To further enhance the resolution without sacrificing the FOV, a significant increase in the excitation intensity leads to photoswitching of the dye such that a *d*STORM image can be recorded (Figure 3.16c). Alternatively, switching to a 60×/ NA 1.2 objective lens allows for imaging at further increased resolution, but at the cost of a smaller FOV (Figure 3.16g).

3.7.2. Tradeoff between throughput and spatial resolution

These results show that the waveguide-based imaging platform indeed opens the opportunity to choose the tradeoff between throughput and resolution. Fast software tools for (almost) real-time *d*STORM reconstruction are readily available [219, 190], such that *d*STORM is mainly limited by the acquisition time. For example, either low NA ESI or *d*STORM can be used for identification of cells of interest or for finding rare biological events, while the choice of the proper method can be made by prioritizing either the acquisition time (choosing ESI) or the resolution (choosing *d*STORM). Subsequently, an identified region of interest may be imaged using high NA *d*STORM to achieve uncompromised resolution. Additionally, the relatively short acquisition times for the low NA images help to prevent photobleaching of fluorophores, allowing for successive acquisition procedures of the same sample as Figure 3.16 shows.

In contrast, answering specific biologically relevant questions might not require highest spatial resolution, but a large sample size instead. In this case, it might not be desirable to successively increase the resolution, but to choose the imaging modality such that the highest possible throughput can be achieved while obtaining just the necessary resolution.

3.7.3. Challenges in defining absolute resolution

As discussed above (cf. section 3.5), the use of low NA objective lenses for localization microscopy suffers from the need for more frames of the same sample to achieve the same localization density and, thus, potentially same resolution in comparison to high NA objective lenses. However, a lower NA also comes with a worse localization precision (cf. section 3.6) which also lowers the potential resolution. Thus, the constraint on the localization density can be relaxed as the resolution will be worse anyway due to the lowered localization precision. The combined effect of localization density and precision can be assessed using the heuristically motivated equation (2.21).

Waveguide imaging approach	Advantages	Possible resolution	Throughput
Low magn./ low NA, diffraction limited	Largest simultaneous FOV, fastest, live-cell compatible, no complex postprocessing	+	++++++
Low magn./ low NA, ESI	Largest simultaneous FOV, fastest, potentially live-cell compatible	++	+++++
High magn./ high NA, dif-fraction limited	Fast, live-cell compatible, no complex postprocessing	++	++++
High magn./ high NA, ESI	Fast, potentially live-cell compatible	+++	+++
Low magn./ low NA, *d*STORM	Largest simultaneous FOV	++++	++
High magn./ high NA, *d*STORM	Highest possible resolution	+++++	+

Figure 3.17.: Qualitative summary of the presented waveguide chip-based imaging approaches that enable scaleable super-resolution imaging and allow to choose the tradeoff between resolution and throughput.

The 20× *d*STORM image of Figure 3.16c features $9.6 \cdot 10^6$ localizations in an area of about $3.1 \cdot 10^4$ µm^2, thus the localization density is $M = 310\,\mu\text{m}^{-2}$. The localization precision determined by the methods of nearest neighbors in adjacent frames is $\Delta x = 87.6\,\text{nm}$ (Figure 3.14a). This results in a lower bound for the resolution of 235.5 nm when using equation (2.21). The authors of [121] argue by empirical findings that the Nyquist resolution limit underestimates the true value for the resolution. They introduced a Nyquist-limit oversampling factor for each spatial dimension. Correspondingly, equation (2.21) can be rewritten in the two-dimensional case as

$$\text{R} \geq \sqrt{\left(q^2 L\right)^2 + \left(2\sqrt{2\ln 2}\Delta x\right)^2}, \tag{3.6}$$

with the oversampling factor $q \geq 1$. Hence, the resolution of Figure 3.16c might be much worse than 235.5 nm. Nevertheless, they did not take into account that in many cases the samples does not cover the entire FOV just like in this example. Furthermore, many imaged structures are not evenly distributed throughout biological samples but rather follow lines like cytoskeleton components.

This argument becomes even stronger when applying equation (2.21) to the 20× *d*STORM image of tubulin as shown in Figure 3.10: The imaged area here is $2.5 \cdot 10^5\,\mu\text{m}^2$ and features $4.9 \cdot 10^6$ localizations and a mean localization precision of 37.8 nm. Hence, the resolution would be worse than 460.4 nm but a significant part of the image is not covered by cells and, additionally, the imaged tubulin is only sparsely concentrated inside the cells. Consequently, the FRC resolution of $(122 \pm 10)\,\text{nm}$ of the same image (cf. Figure 3.10c) is better by about factor of four.

From this discussion, it can be noted that measuring the obtained resolution can be a challenging and inconclusive task as different definitions can lead to significantly different results. Thus, it is not easy to state which technique (e.g. diffraction limit imaging, ESI, or *d*STORM) should be chosen for a particular field-of-view and desired resolution. Anyway, the discussion so far can give a qualitative reference which approach to choose and is summarized in Figure 3.17.

3.7.4. Analytical expression for resolution estimation in SMLM

To draw a quantitative conclusion, using the definition of equation (2.21) allows to estimate the obtainable resolution. As a big advantage, this can be done in an analytical way for different *d*STORM scenarios (Figure 3.18). The alternative way

of using the FRC resolution requires extensive simulations [46] or will only lead to conclusions only for specific sample geometries [143]. For instance, Legant et. al [121] have demonstrated by simulation, that only changing the sample geometry while keeping other influences on the resolution constant, the FRC resolution can differ by a factor of two.

It is therefore beneficial to derive an analytical expression for the estimation of the achievable resolution that is independent from the sample geometry. From the above derived relations, it is possible to combine equation (2.21) to estimate the resolution with equation (3.3) to estimate reasonable emitter densities. Furthermore, equation (2.15) can be used to estimate the localization precision while equation (3.5) is used to find the collection efficiencies and equation (3.4) to find the PSF widths for different NAs. The experimentally determined photoelectron count values for waveguide-based *d*STORM imaging are used for Atto 488 and Alexa 647 and the emission wavelengths are taken from literature [40].

3.7.5. Imaging time determines resolution in SMLM

When using a state-of-the art sCMOS camera with 2048 × 2048 pixels and a 20× magnification objective lens, a FOV of 665 µm × 665 µm can be imaged simultaneously. The resolution is plotted as a function of the number of necessary frames to image this FOV. For a higher magnification, it is possible to stitch together multiple smaller FOVs, which increases the necessary number of frames accordingly [139] and can be applied to different modalities [137]. It should be noted that in this case the detection arm of the microscope and the sample need to be moved relative to each other which can take additional time but is not further considered here.

Different parameters are evaluated for the *d*STORM imaging scenario. On the one hand, the diffraction limited resolution (defined by the Abbe limit) as well as the density of simultaneously active emitters can be higher due to the shorter emission wavelength when using Atto 488 in comparison to Alexa 647. On the other hand, about four times more photons were emitted per switching cycle for Alexa 647 which leads to a higher localization precision, so both dyes are considered. Additionally, different parameters for the Nyquist limit oversampling factor q and the PSF overlap probability p are evaluated. The resolution lower bound is calculated for an oversampling factor of $q = 1$ and an overlap probability of $p = 1\%$ as well as an oversampling factor of $q = 5$ and an overlap probability of $p = 10\%$. The second scenario corresponds to the assumption that the two-

dimensional emitter density should be 25 times higher than in the first case, for which the longer imaging time is partially compensated for by permitting a higher emitter density on the cost of taking false localizations into account.

3.7.6. Comparison of imaging modalities

The three cases of a 20×/ NA 0.45 air objective lens, a 20×/ NA 0.7 air objective lens and a 60×/ NA 1.2 water immersion objective lens are considered. All of these lenses are commercially available. The first and the latter are rather often used because the magnification and the NA are matched to the Nyquist sampling theorem for diffraction limited imaging when using detectors with 6.5 µm pixel width, though the image is already undersampled, depending on the fluorescence emission wavelength. When using the 20×/ NA 0.7 lens, the image is even more undersampled so there is no gain in resolution. Nevertheless, the localization precision in SMLM is improved as the light collection efficiency increases when the NA is increased. It is also possible to vary the magnification in the detection path e.g. by changing the tube lens which can lead to both improved resolution and localization precision in diffraction limited or SMLM imaging, respectively. However, this would change the FOV so the interdependencies are nontrivial and therefore not further considered here.

The diffraction limited resolution is chosen as the maximum of the Nyquist sampled resolution and the Abbe limit, while the resolution of waveguided based ESI is assumed to be a factor of 1.47 better than the diffraction limit (cf. Figure 3.12). A number of 200 frames is assumed to be acquired for one reconstructed ESI image. Furthermore, the throughput of a commercially available structured illumination microscope (GE Healthcare OMX v4) is considered that achieves a resolution enhancement of a factor of two as compared to the Abbe limit. However, fifteen raw images need to be recorded for the generation of one super-resolved image and more than 263 reconstructed images need to be stitched together to achieve a FOV of 665 µm × 665 µm.

3.7.7. Choosing the modality for optimal throughput and resolution

The dependence between the throughput and the lower resolution bound is plotted in Figure 3.18. As expected, the relation is not trivial and different modalities need

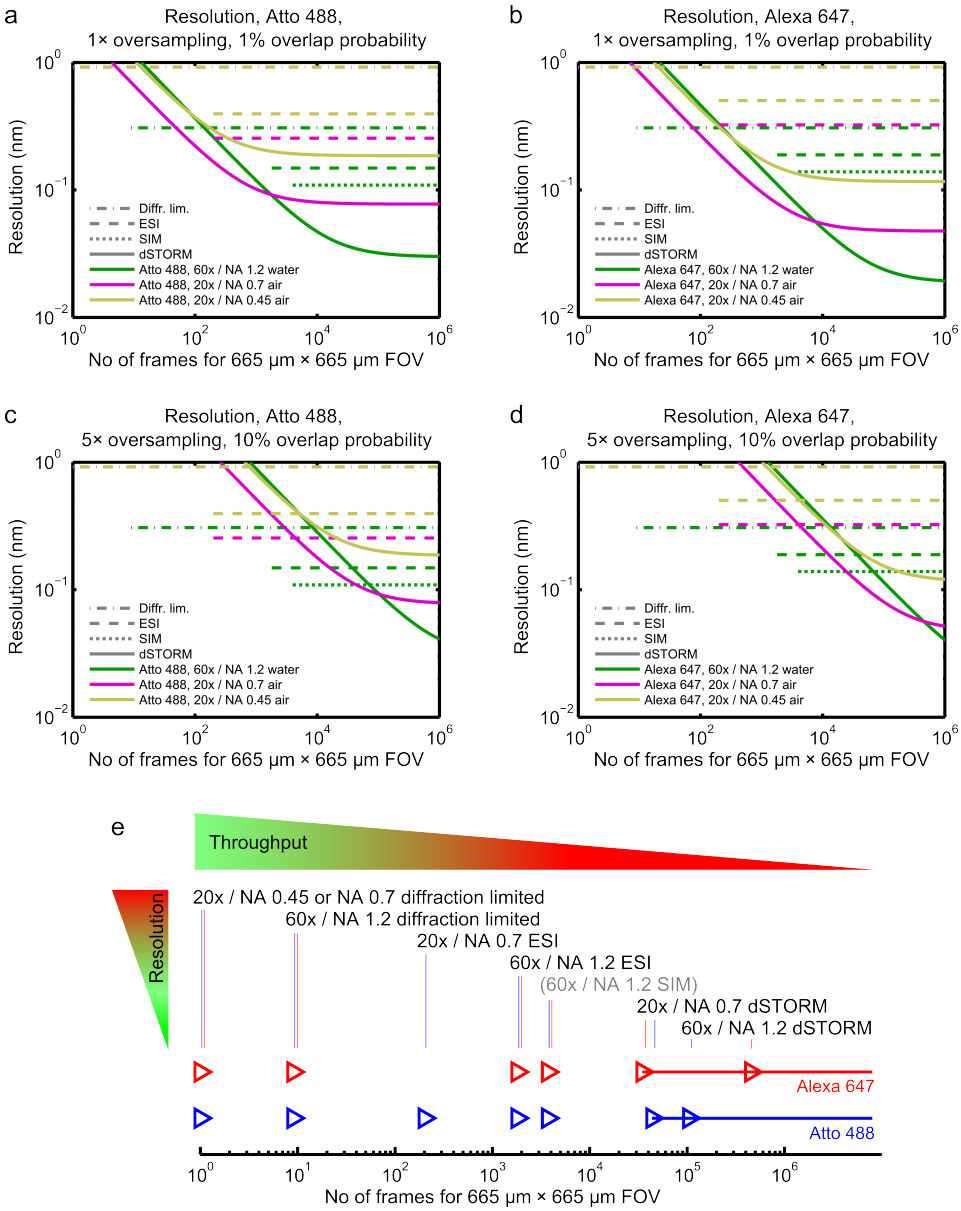

Figure 3.18.: a-d, The relation between throughput and the obtainable resolution strongly depends on the particular imaging scenario, exemplary shown for four different cases. Subfigure **e** summarizes the break even points for the considered techniques and scenarios of **c** and **d**. Solid lines indicate that the resolution can be increased at cost of throughput in SMLM, while increasing the number of frames in case of diffraction limited imaging, ESI, and SIM cannot increase the resolution when neglecting the influence of the SNR.

to be selected to achieve the best resolution for a particular throughput in terms of required raw data frames and vice versa.

In case of Atto 488 at $q = 1$ times Nyquist oversampling for dSTORM and $p = 1\%$ PSF overlap probability (Figure 3.18a), diffraction limited imaging with 20× lenses and the 60× from 9 frames on yield best results. The better resolution predicted with the NA 0.7 lens between 5 and 9 frames should be neglected for different reasons, e.g. the time necessary to drive most dyes to the non-emitting off-state. Nevertheless, already from 50 frames on, dSTORM with the NA 0.7 lens gives a better resolution than widefield imaging with the NA 1.2 lens. For more than 1750 frames, switching to the higher NA can be advised. In case of Alexa 647 at $q = 1$ times Nyquist oversampling for dSTORM and $p = 1\%$ PSF overlap probability (Figure 3.18b), the break-even point between NA 0.7 and NA 1.2 shifts to 7563 frames. Assuming a single frame exposure time of 50 ms, this corresponds to 6.3 minutes of imaging and a resolution of about 56 nm that can be achieved over this large field of view. ESI is outperformed by dSTORM in all cases for the $q = 1$ times Nyquist oversampling and $p = 1\%$ PSF overlap probability scenario. Even more noteably, the commercially established SIM microscopy with a NA 1.2 objective lens is also outperformed by dSTORM, even when using the low NA 0.45 lens.

This relation changes when considering $q = 5$ times Nyquist oversampling and 10% PSF overlap probability scenario, however, then the situation becomes more complex and also depends on the utilized dye. For Atto 488, the best options while decreasing the throughput to increase the resolution in ascending order range from diffraction limited, over ESI and SIM to dSTORM imaging at different magnifications and NAs (Figure 3.18c). Note that SIM imaging requires a different setup, hence, this option is not available for presented waveguide-imaging. In contrast to Atto 488, NA 1.2 diffraction limited can be preferred over NA 0.7 ESI imaging in all cases for Alexa 647 (Figure 3.18d). In this theoretical evaluation, high NA 1.2 dSTORM leads to a better resolution than NA 0.7 dSTORM not before 451 000 frames which corresponds to more than 6 hours of imaging at single frame exposure times of 50 ms.

For extremely long acquisition times in dSTORM, it can be expected that most labels will either have been bleached or have photoswitched at least once already. In both cases, the resolution cannot be increased by recording more frames. These scenarios are therefore reserved for other SMLM approaches like PAINT [182] or DNA-PAINT [113, 178] where fresh labels are continuously supplied from solution. These techniques have the advantage that the emitter density can be more

easily adjusted by simply changing the concentration of the labels in the solution. Controlling the density of simultaneously active emitters in *d*STORM and PALM requires to dynamically control the intensity of the photoswitching laser. As the data presented in Figure 3.18 assumes an optimal and constant emitter density, active control of this parameter is crucial to achieve the discussed resolutions for *d*STORM.

Importantly, throughput must not be confused with temporal resolution. The temporal resolution corresponds to how many raw frames must be recorded to achieve one (reconstructed) image of arbitrarily large or small FOV. In contrast, throughput states how many frames must be recorded for one resulting image of a particular FOV, which is chosen as $665\,\mu m \times 665\,\mu m$ for the calculations of Figure 3.18. Additionally, just like temporal resolution it makes sense to measure throughput in time rather than number of frames. The comparison between different techniques becomes again very challenging in this case because required single frame exposure times can vary significantly depending on the used fluorophores, camera, etc. and other factors like movement of the sample might need to be considered. Therefore, the throughput is given in frames which leads to comparison between different techniques that is dependent on less parameters while the dependency on the considered parameters is non-trivial already.

3.8. Discussion and outlook

This work has focused on the development of waveguide chip-based imaging for super-resolution microscopy rather than on its application. Nevertheless, the ability to choose the operation point in the tradeoff between resolution and throughput opens up several new opportunities in cellular biology.

As one possible scenario, a large number of cells can be scanned via low magnification/ low NA imaging on the waveguide at high throughput. This data can be used to find rare biological events or phenotypes of interest which can be re-imaged at superior resolution with high magnification/ high NA lenses. Alternatively, it is possible to identify the resolution necessary for specific problems and select the modality that enables this resolution at highest throughput. Waveguide-based imaging is well suited in both cases as it offers a wide range of imaging conditions ranging from diffraction limited imaging over a moderate resolution enhancement using ESI to uncompromised resolutions using SMLM. The use of advanced localization routines that can deal with high density data as for instance compressive

sensing [230] or multi-emitter fitting [100] might further contribute to the variety of approaches in this context. However, waveguide-based imaging is so far restricted to TIRF excitation which limits the axial extend to about 200 nm depth. While the illumination over the entire stretch of the waveguide enables large FOV TIRF imaging, the illuminated area usually goes beyond the FOV. All samples located on top of the currently imaged waveguide are simultaneously exposed to fluorescence excitation which must be considered in the experimental design, e.g. with respect to photobleaching.

Another promising application is wide FOV live-cell imaging. A large number of cells can be observed simultaneously at temporal resolutions that are only limited by the frame rates of the detector. If a higher spatial resolution is desired, temporal resolution can be sacrificed to enhance the spatial resolution via chip-based ESI which still has the potential to enable live-cell imaging at sub-second temporal resolutions, but comes at the cost of potentially inhomogeneous or anisotropic spatial resolution.

Though both ESI and *d*STORM are based on fluorescence signal dynamics, the underlying processes significantly differ for their waveguide-based implementations. As in conventional realizations, chip-based *d*STORM relies on the ability of the dyes to exhibit photoswitching, but the waveguide-based implementation of ESI induces spatial intensity fluctuations by the waveguide excitation. It is therefore not restricted to specific probes, which makes it applicable to an even wider range of scenarios.

While SMLM and fluctuation-based approaches already belong to the most wide-spread techniques for super-resolution imaging, the chip-based implementation dramatically reduces the complexity of the setup and, thus, has the potential to make it accessible for a wider range of users. Incorporating it into photonic integrated circuits will make it compatible with fast and compact optical fiber components. This will simply allow to add or remove any optical fiber components, thus eliminating the need of system re-alignment which is often the case when using free-space optical components. By guiding the illumination light through optical fibers and waveguides, many standard optical microscopes can be used to acquire super-resolved images. Future developments towards on-chip laser generation, filtering, and steering of entire illumination systems will potentially further extend the capabilities.

Additionally, advances in the chip-design that allow for the precise controlling of interference patterns, for instance counterpropagating waves with plane wavefronts, will supposably upgrade waveguide-based super-resolution to further

modalities, e.g. SIM [90]. Furthermore, the integrated platform makes combinations with different lab-on-a-chip methods, e.g. microfluidics [213], optical trapping [89] or other detection techniques [52] straightforward to implement. Other analysis modes based on single emitter localization can also be utilized e.g. for highly sensitive quantitative binding assays [109].

4. Nanoscopy of optically trapped samples

This chapter is based in major parts on the peer-reviewed publication

R. Diekmann, D.L. Wolfson, C. Spahn, M. Heilemann, M. Schüttpelz, and T. Huser. Nanoscopy of bacterial cells immobilized by holographic optical tweezers. *Nature Communications*, **7**:13711, 2016,

and the invited article

R. Diekmann, M. Schüttpelz, and T. Huser. Super-Auflösung in der Laser-Falle. *Physik in unserer Zeit*, **48**(2):58–89, 2017.

Section 4.6 gives an outlook to the manuscript in preparation

A. Ahmadi, I. Rosnes, P. Blicher, R. Diekmann, M. Schüttpelz, K. Glette, J. Tørresen, M. Bjørås, B. Dalhus, and A. Rowe. A deep insight into protein DNA-repair on the single molecule level (in preparation, 2017).

Imaging non-adherent cells by super-resolution far-field fluorescence microscopy is currently not possible because of their rapid movement while in suspension. Holographic optical tweezers enable the ability to freely control the number and position of optical traps, thus facilitating the unrestricted manipulation of cells in a volume around the focal plane. Immobilizing non-adherent cells by optical tweezers is sufficient to achieve optical resolution well below the diffraction limit using localization microscopy. The image quality can be further increased via statistical correction for the residual Brownian motion of the sample inside the optical trapping potential. Using the holographic optical tweezers, individual cells can be oriented arbitrarily relative to the microscope's focal plane, enabling access to sample sections that are impossible to achieve with conventional sample preparation and immobilization. This opens up new opportunities to super-resolve e.g. the nanoscale organization of chromosomal DNA in individual bacterial cells. Furthermore, the implementation of flexible optical trapping together with a fast and sensitive detector for single emitter localization allows to study DNA-protein interactions at high dynamics.

4.1. Introduction

Single molecule localization microscopy techniques, such as *d*STORM, (F)PALM, or (DNA-) PAINT typically require several thousands of image frames for the reconstruction of a single super-resolved image (cf. section 3.7), leading to very long acquisition times on the scale of seconds to minutes [18, 168, 85, 182, 178]. This entails a high demand on the spatial position stability of the sample, which is typically achieved by chemical fixation and attachment of biological samples such as cells to glass coverslips.

Extended acquisition times make super-resolution microscopy inapplicable to non-adherent cells or other freely diffusing samples, such as bacterial cells or immune cells. Embedding these cells into gel matrices [20] (e.g. agarose) can physically hold them still in a certain position and orientation but may alter their appearance and impair signal-to-noise ratios during the imaging process. Also, the complex optical requirements for current super-resolution microscopy methods restrict the ability to freely access and/or orient the sample with respect to the image plane or during cell-cell interactions, typically resulting in different spatial resolutions along different directions [176]. Fast, parallelized versions of nanoscopy have been developed, but these still require the acquisition of several tens of images, making them too slow to image fast moving cells [87, 80, 81, 117, 181, 34]. Indeed, non-adherent cells in suspension have not been imaged by any form of super-resolution microscopy before.

This chapter demonstrates that it is possible to overcome these limitations in super-resolution microscopy by the combined use of a holographic optical tweezers system and SMLM. Beam shaping by a spatial light modulator enables the generation and dynamic control of multiple, independent optical traps. Combining this system with *d*STORM and single molecule tracking facilitates the immobilization of the sample at specific, pre-defined positions as well as orientations in suspension during the imaging process.

4.2. Influence of trap on dSTORM image

4.2.1. Optical setup

Holographic optical tweezers are integrated into a widefield fluorescence microscope (Figure 4.1). Specific wavelengths emitted by an Argon-Krypton-ion laser are selected via an acousto-optical tunable filter and the beam is focussed onto the

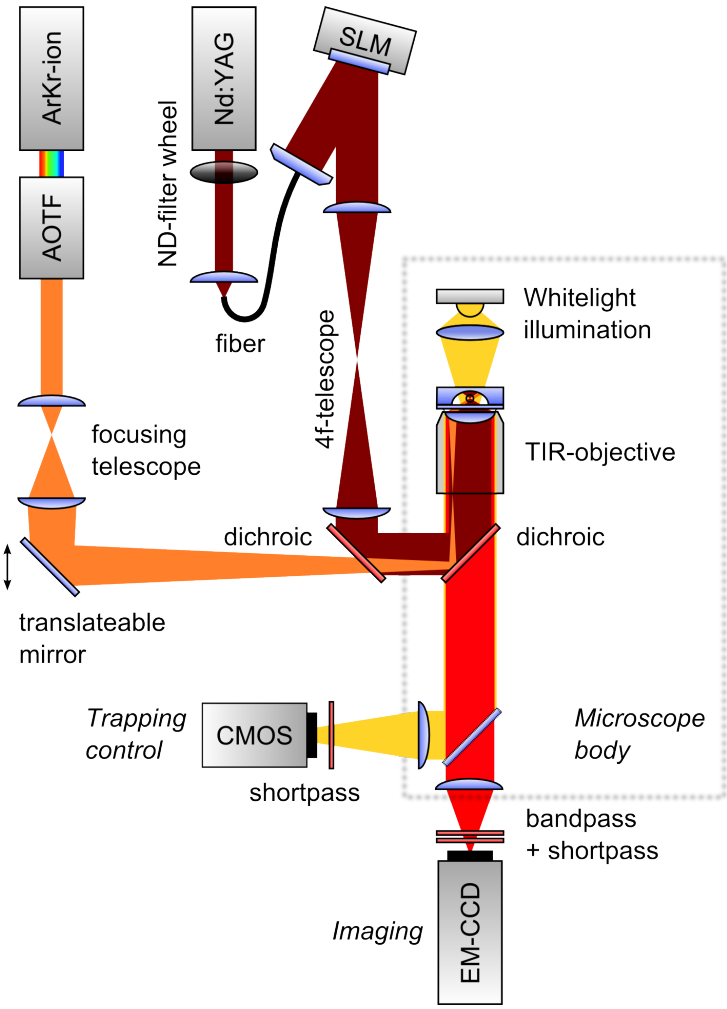

Figure 4.1.: Microscope setup combining widefield fluorescence imaging for *d*STORM and holographic optical trapping.

back-focal plane of the microscope objective lens. A translateable mirror allows to switch from epi to HILO illumination [201]. The fluorescence emission is separated from the excitation by a dichroic beam splitter and focused onto an EM-CCD camera. Optical trapping is achieved by the use of a Neodym:YAG laser emitting at 1064 nm. The beam is coupled through a polarization-maintaining fiber, collimated and directed onto an SLM. The SLM is imaged to the back-focal plane of the objective lens via a 4f-telescope. Along this path, the trapping beam is combined with the fluorescence excitation via a dichroic mirror. Control of the SLM via a GPU-based algorithm allows for dynamic positioning of multiple optical traps in a volume around the focal plane [60, 152, 153, 154, 155]. Hence, it is possible to hold samples at multiple points and position them almost arbitrarily during imaging.

4.2.2. Brownian motion lowers effective localization precision

The potential of the implementation (Figure 4.1) is demonstrated by first trapping microspheres in suspension (Figure 4.2b). Their surface is labeled with Alexa 647 for single molecule localization by *d*STORM, excited by HILO illumination. Note that the beads are significantly bigger than the depth of focus, so only their edge appears in the reconstructed images. Due to the short single frame exposure time of 29.55 ms, individual fluorophores on the bead surface are in general localized with mean single molecule localization precisions [200] of approximately 10 nm to 12 nm (Figure 4.2c), mainly depending on the photon statistics of the fluorescence emission. This is comparable to what is typically achieved in SMLM of samples attached to a glass coverslip (cf. Figure 5.2d,e).

Nevertheless, holding the sample above the coverslip by optical traps weakens the effective localization precision due to position fluctuations of the sample (Figure 4.2d). For this reason, the localization precision determined from the distribution of nearest neighboring localizations in subsequent frames will be used in the following. In constrast to the use of the photon statistics, it takes the resulting distribution of the localizations into account and therefore also measures the effect of the sample moving inside the optical traps.

Depending on the laser power of the optical tweezers, the surface of the microspheres is reconstructed with different apparent widths in the *d*STORM images obtained from several thousands of image frames (Figure 4.2a). Different near-IR laser powers lead to differences in trap stiffness and, hence, to different restoring forces during the experiment. This circumstance becomes clear by considering an inherent property of optical tweezers: due to weak interaction forces, an optically

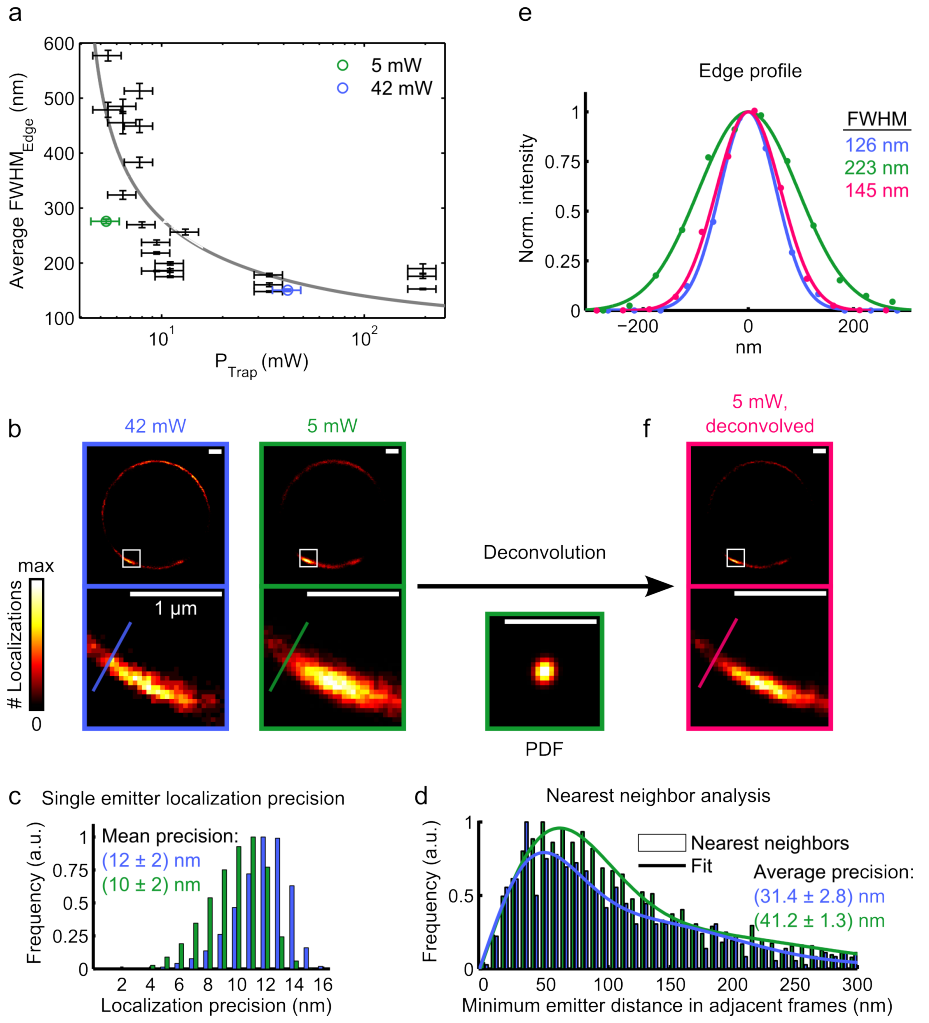

Figure 4.2.: Response of the combined *d*STORM and optical tweezers setup. **a**, Polystyrene beads with fluorophores attached to their surface are optically trapped by applying different trapping laser powers. The average FWHM in the *d*STORM reconstruction of the bead edge is determined for the different trapping powers. For reference, the gray curve indicates the theoretically expected power dependence. **b**, Exemplary images show *d*STORM reconstructions for trapping laser powers of $42\,\mathrm{mW}$ (blue) and $5\,\mathrm{mW}$ (green). **c**, The histogram of the individual single molecule localization precisions shows comparable values though the bead edge appears significantly wider in the line profile when trapping with the lower power (**e**). **d**, Accordingly, different localization precisions are found when using the neareast neighbor analysis in adjacent frames. **f**, The PDF for a specific trap configuration is used for deconvolution, uncovering the much smaller structure of the bead's edge.

trapped object moves stochastically around a mean position while experiencing Brownian motion of the surrounding molecules.

4.2.3. Position distribution function (PDF)

As the optical trapping potential may be approximated by a harmonic oscillator potential [62], the position of an optically trapped particle follows the statistics of a Gaussian distribution. The position distribution function PDF can thus be approximated by the function

$$\mathrm{PDF}(\boldsymbol{x}) = C \exp\left(\frac{-V(\boldsymbol{x})}{k_b T}\right), \tag{4.1}$$

where $k_b T$ is the thermal energy, $V(\boldsymbol{x})$ is the trapping potential, and C is a normalization factor [221]. As the trapping potential can be approximated by a harmonic potential in the vicinity of a stable equilibrium position [49], the restoring force is

$$\boldsymbol{F}(\boldsymbol{x}) = -\kappa\,(\boldsymbol{x} - \boldsymbol{x}_0) \tag{4.2}$$

and the trapping potential is given by

$$V(\boldsymbol{x}) = \kappa\,(\boldsymbol{x} - \boldsymbol{x}_0)^2 \tag{4.3}$$

where κ denotes the scalar trap stiffness and $(\boldsymbol{x} - \boldsymbol{x}_0)$ the displacement from the particle's mean position $\boldsymbol{x}_0$. By explicitly considering the harmonic potential, the position distribution function $\mathrm{PDF}(\boldsymbol{x})$ becomes a Gaussian distribution with a standard deviation of

$$\sigma = \sqrt{\frac{k_b T}{2\kappa}}. \tag{4.4}$$

As the trap stiffness κ is directly proportional to the trap power P_{trap} [120], it follows for the full-width-at-half-maximum FWHM of the PDF that

$$\mathrm{FWHM} = 2\sqrt{2\ln 2}\,\sigma \propto \frac{1}{\sqrt{P_{\mathrm{trap}}}}. \tag{4.5}$$

For explicit consideration of the three-dimensional trap properties, the restor-

ing force of the optical trap can be written in the form of

$$\boldsymbol{F}(\boldsymbol{x}) = -\boldsymbol{\kappa}\,(\boldsymbol{x} - \boldsymbol{x}_0)\,, \tag{4.6}$$

where $\boldsymbol{\kappa}$ is the stiffness matrix in the coordinate system of the microscope. By an appropriate coordinate transformation, it is possible to approximate the stiffness matrix by a diagonal matrix, where the diagonal entries correspond to three (distinct) trap stiffness values in orthogonal spatial directions. Using a single, "perfect" trap focus, the diagonal matrix $\boldsymbol{\kappa}$ consists of two equal elements indicating the lateral trap stiffness and one element indicating the axial trap stiffness. The axial stiffness is usually significantly lower than the lateral trap stiffness [24], causing position fluctuations of greater extent in the axial direction. If the effective trapping potential does not possess lateral rotational symmetry, e.g. caused by the shape of the trapped object or the simultaneous use of multiple traps, the projection of the PDF to the lateral plane becomes an elliptical Gaussian distribution, i.e.

$$\begin{aligned}\mathrm{PDF}(x,y) = C\exp\Bigg(&- \left(\frac{(x-x_0)\,\cos\alpha + (y-y_0)\sin\alpha}{\sqrt{2}\,\sigma_1}\right)^2 \\ &- \left(\frac{-(x-x_0)\,\sin\alpha + (y-y_0)\cos\alpha}{\sqrt{2}\,\sigma_2}\right)^2 \Bigg),\end{aligned} \tag{4.7}$$

where (x, y) is the object's position with the center position (x_0, y_0), α is the rotational angle of the ellipsoid axes relative to the coordinate system of the microscope, σ_1 and σ_2 are the independent standard deviations for orthogonal directions, and C is a normalization factor.

Any fluorescent molecule which is firmly attached to the optically trapped particle will exhibit the displacement statistics described by the PDF. If the same single molecule is located multiple times during the *d*STORM experiment, its localizations must exhibit the position distribution characteristics of the entire optically trapped sample (assuming the sample is stiff in comparison to the surrounding medium). The same applies to labeled structures that are visualized with subdiffraction resolution by single emitter localizations.

Mathematically, this corresponds to the *d*STORM image of the structure, as it might be determined for an immobilized sample, convolved with the position distribution experienced within the optical trap. In case of the microsphere bead edges, this fact is illustrated by their average FWHM becoming broader in the *d*STORM images as the trap power decreases and roughly following the theoretically expected dependence of FWHM $\propto \frac{1}{\sqrt{P_{\mathrm{trap}}}}$ (Figure 4.2a).

4.3. Computational motion compensation

4.3.1. Similarity to diffraction-limited image formation

This considerations clearly bears analogies with the process of optical image formation where the diffraction-limited imaging process causes a structure to appear convolved by the optical point spread function in far-field light microscopy. An established postprocessing technique in this case is image deconvolution [186], exploiting the fact that by prior knowledge of the PSF (or even theoretical modeling of the PSF based on known parameters of the imaging system) the actual structure can be revealed from the originally recorded image more clearly. With regard to SMLM of samples held by optical tweezers, knowing the PDF of the object inside the optical trap also enables the use of algorithmic deconvolution of the reconstructed image to reduce the influence of position fluctuations on the reconstructed image.

4.3.2. Validity of deconvolution approach

This approach will hold if at least one of two conditions is met: (i) each label is localized several times during the *d*STORM imaging process, or (ii) a high labeling density of the structure is achieved, thus, the distance between the labels is sufficiently small, i.e. on the order of the effective localization precision.

Though the first condition is difficult to measure for an individual experiment, Dempsey et al. [40] have found that each Alexa 647 molecule could be localized during a mean number of 14 switching cycles under comparable buffer conditions (enzymatic oxygen removal using glucose oxidase and catalase plus using MEA as the reducing agent, though the MEA concentration was 10 mM instead of 100 mM) as it has been used for the experiments presented here. If single frame exposure times are shorter than the timespan of the fluorescence emission during a switching cycle, a fluorophore can be detected multiple times per switching cycle. This allows for an even higher number of localizations per fluorophore contributing to the reconstructed image. Additionally, one label, e.g. an antibody, might possibly be tagged by multiple fluorophores, further increasing the possible number of localizations per label. The number of localizations per label does, however, also depend on other experiment specific parameters, e.g. the number of frames recorded, and might therefore differ from the reported values. In any case, the condition of many localizations per label can in principle be met when using Alexa 647.

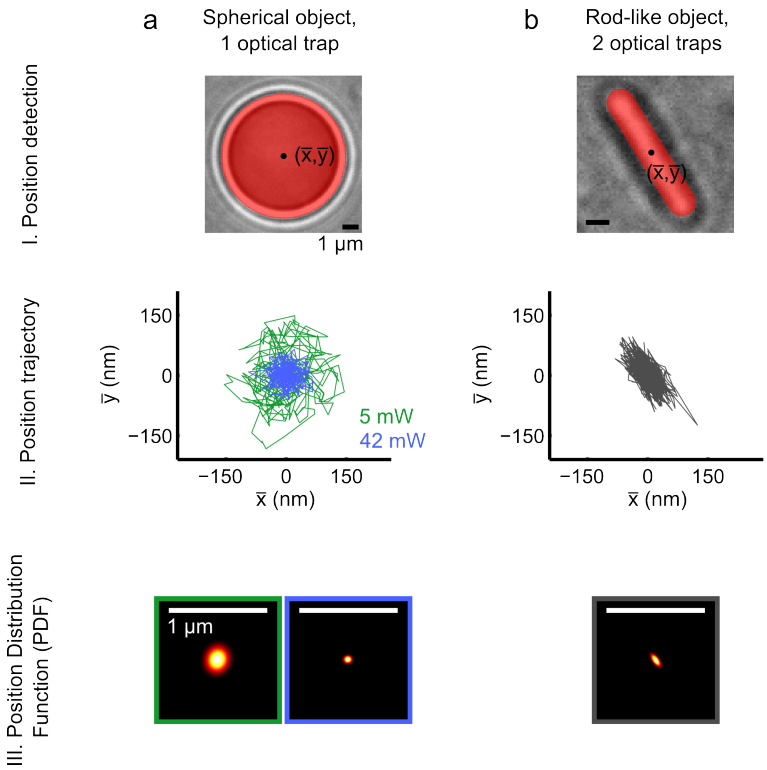

Figure 4.3.: Principle of the position distribution function (PDF): I, White light imaging of the trapped object (**a**, polystyrene bead, **b**, *E. coli* cell) followed by frame-by-frame determination of its "center-of-mass" $(\overline{x}, \overline{y})$. II, Typical position trajectories $(5\,\mathrm{s})$. Beads were trapped using $42\,\mathrm{mW}$ (blue) and $5\,\mathrm{mW}$ (green) laser power, revealing different extents of the trap stiffness. III, Multiple position determinations are used to calculate the PDF. In contrast to spherical beads, trapping rod-like shaped bacteria results in a strongly elliptical PDF.

The localization density is estimated to find the average distance between the labels: The reconstruction shown in Figure 4.2b for a trap power of 5 mW consists of 15,236 localizations detected in 7,056 raw images recorded in approximately 220 s. As the diameter of the bead is 8.18 µm, its perimeter is 25.7 µm, and from the line profile shown in Figure 4.2e it can be estimated that the localizations are spread over a length of 0.5 µm orthogonal to the bead edge. Consequently, the localizations cover an area of about 12.85 μm^2. As the bead presumably shows rotational Brownian motion during the imaging procedure (Figure 4.6d), the labels move and each position on the edge is detected just once rather than 14 times. These numbers yield an approximate labeling density of the bead edge of about 1186 μm^{-2}, giving a mean distance between two localizations of about $\frac{1}{\sqrt{1186\,\mu m^{-2}}} =$ 29 nm. This value is on the order of the effective localization precision of (41.3 ± 1.3) nm (Figure 4.2d) and confirms that the deconvolution approach is valid.

4.3.3. Sample geometry and trap arrangement influence PDF

For PDF generation, a transmitted light image stack (Figure 4.3, upper row) is recorded prior or subsequent to the *d*STORM data acquisition. Compared to the microsphere experiment (Figure 4.3a), where a single optical trap was used to hold each bead, fixed rod-like Escherichia coli (*E. coli*) bacteria floating in suspension are captured by two optical traps (Figure 4.3b), which are positioned at the cell's end caps (Figure 4.7a). The bacterium shows a strongly elliptical PDF (Figure 4.2b and Figure 4.5c), yielding standard deviations for the 2D Gaussian of $\sigma_1 = (43.6 \pm 0.4)$ nm and $\sigma_2 = (19.5 \pm 0.2)$ nm. During displacements orthogonal to the long axis of the *E. coli* cell, a similarly high restoring force from both traps acts on the cell, while during displacements parallel to the long axis, the restoring force from one trap is significantly lower due to the cell's rod-like shape. This assumption is confirmed by the fact that the long axis of the PDF ellipse is co-located with the long axis of the bacterial cell.

These data show that the PDF not only depends on the optical trap properties, but also on the shape and alignment of the trapped object. That is why the PDF is not a property of the setup only, but has to be determined for each experiment individually. The beam used for fluorescence excitation and photoswitching also has an effect on the PDF. Usually, high intensities on the order of 0.5 $\frac{kW}{cm^2}$ to 5 $\frac{kW}{cm^2}$ are used [203], leading to non-negligible radiation pressure that may significantly displace the trapped object. As highly inclined and laminated optical sheet (HILO) excitation is often used to obtain such high intensities, the specimen becomes dis-

placed both in axial and lateral directions. Hence, the HILO beam is also switched on during the data acquisition for determination of the PDF.

4.3.4. Experimental PDF generation

Using a center of mass algorithm [26], the PDF can be identified for symmetrically as well as for non-symmetrically shaped samples, such as single bacteria and other cells. After the trajectory of the sample is binned, a 2D Gaussian function is fitted to the distribution and rendered to the same pixel size as the *d*STORM image for which it will be used during deconvolution.

A white light image stack of the sample shown in Figure 4.5 consisting of 10 146 frames is used to evaluate how many measured frames are necessary to generate a PDF with sufficient accuracy (Figure 4.4). Only a certain number of frames starting from the first frame is used for fitting the 2D elliptical Gaussian, and the result from the fit is compared to the 2D histogram, which is directly obtained from the position measurements of all 10 146 frames. Using a pixel size (according to a bin size) of 25 nm × 25 nm, the mean deviation from the fit (Figure 4.4d) to the measured values (Figure 4.4b) of all 10 146 frames drops below 1.4% (within the central region of 400 nm × 400 nm) if data from more than 500 frames is used for the fit (Figure 4.4a). The PDF accuracy is even further increased by using a smaller pixel size of 10 nm × 10 nm (Figure 4.4c,e). It has to be assured that the resulting PDF exhibits the same pixel size as the *d*STORM image for which it is used during the deconvolution.

The excellent agreement between the directly measured values (Figure 4.4b,c) and the PDF obtained from the fit to all available frames (Figure 4.4d,e) shows that an elliptical 2D Gaussian is a valid model to describe the position distribution of optically trapped objects. This is also valid for non-spherical samples and multiple trap foci as both are present in case of the *E. coli* held by two traps. By taking an effective acquisition time of 6 ms to 31 ms per frame into account, the measurements for the PDF from 500 frames can be conducted within 3 s to 16 s. Thus, it could also be collected prior to the *d*STORM acquisition due to this relatively short time without significantly bleaching the fluorescent labels even if the HILO beam for fluorescence excitation was switched on.

With regard to the trapped beads, it becomes evident that the width of the PDF strongly depends on the trapping laser power, and, therefore, the stiffness of the optical trap. Nevertheless, the outcome of the deconvolution process affirms that also in the case of low trap stiffness a similar result concerning an imaged

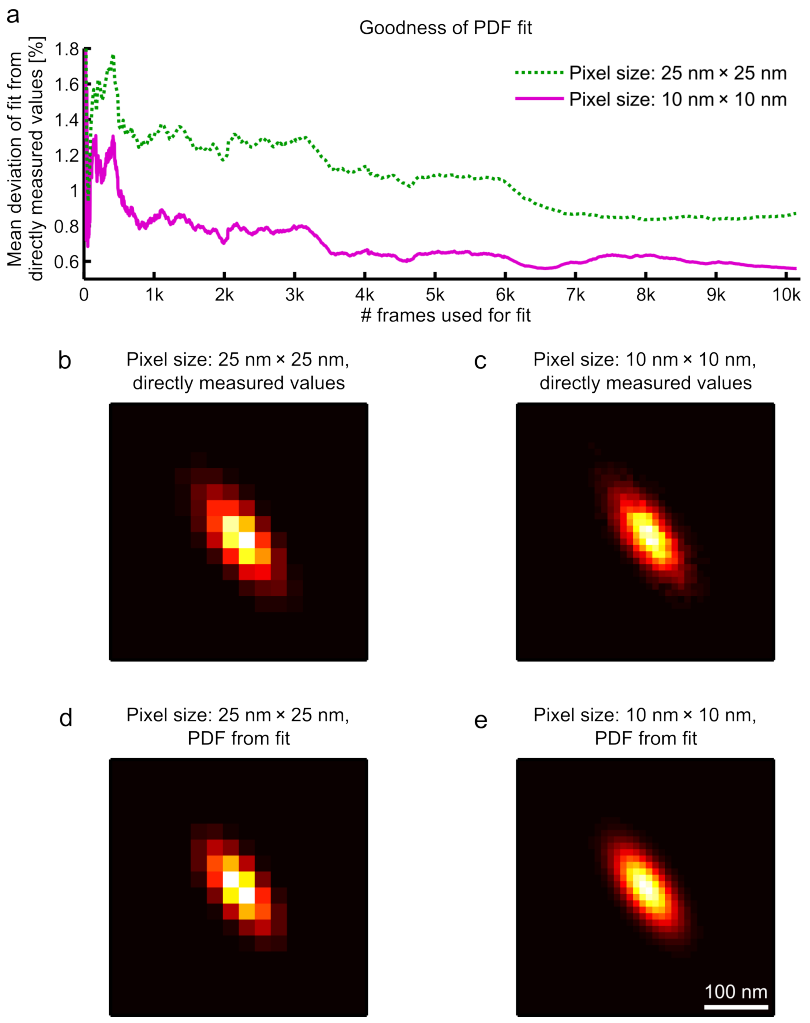

Figure 4.4.: **a**, Quality of the determined position distribution function depending on the numbers of frames used for its computation. Binning the measured positions of the trapped object to a grid of $25\,\mathrm{nm}$ (**b**) or $10\,\mathrm{nm}$ (**c**) pixel widths and heights enables the fit of a two-dimensional, elliptical Gaussian function (**d**,**e**). The deviation between the measured PDF and the model is below 1.4% when 500 frames are used for the fit. Hence, a PDF of high quality can be acquired in about $3\,\mathrm{s}$.

structure is achieved in comparison to the same bead being trapped at 8.4 times higher power (Figure 4.2d). This is of particular relevance for potential extensions to live cell imaging, where preferably the lowest possible trap powers should be used to minimize phototoxicity [141].

4.3.5. Simultaneous position tracking as a possible alternative

As an alternative to the deconvolution approach, it might be possible to simultaneously track the position of the sample and acquire the *d*STORM data frame by frame. In this case, the position fluctuations could be used to directly correct for their effect on the localization data in each frame without the need for a statistical method. This could be realized by optically splitting the imaging path into two different color channels, i.e. one which images the sample position in a transmitted light color channel and one which collects fluorescence signals for *d*STORM analysis. As a drawback, this approach would complicate the optical setup because the position detection by transmitted light and the fluorescence imaging path would now have to be split into two different channels, e.g. separated by wavelengths. Furthermore, illuminating the sample with an additional wavelength could interfere with the photoswitching process.

4.4. Imaging optically trapped bacteria in solution

4.4.1. dSTORM of E. coli

For testing *d*STORM imaging in combination with optical trapping on biological samples, *E. coli* bacterial cells were arranged parallel to the focal plane by the use of two traps and held a few µm above the glass coverslip during the data acquisition. Chromosomal DNA within the bacteria was pre-labeled with Alexa 647 using a click chemistry approach. Once trapped, a super-resolution image of the *E. coli* cell was recorded in about 90 s. A comparison of the directly reconstructed *d*STORM image of the chromosomal DNA (Figure 4.5a) and the diffraction-limited fluorescence image (Figure 4.5b) demonstrates the capability of super-resolution imaging of optically trapped biological samples.

Deconvolution of the *d*STORM reconstruction (Figure 4.5a) with the optical trap's PDF (Figure 4.5c) leads to an image with increased spatial resolution and higher contrast (Figure 4.5d). Structural features of the bacterial chromosome with dimensions of less than 100 nm can now be resolved (Figure 4.5e). Close inspection

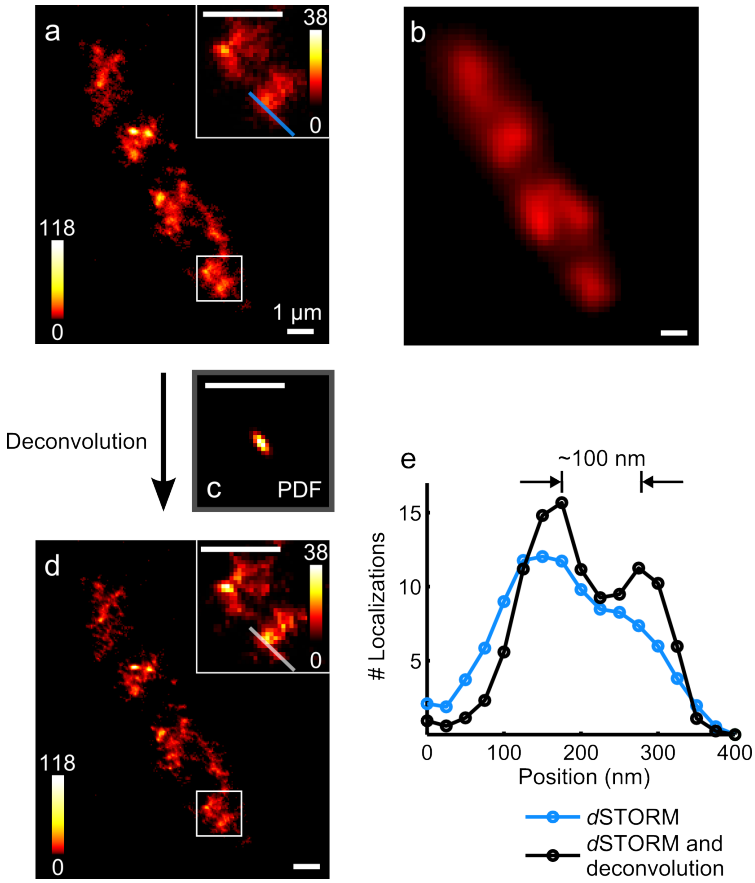

Figure 4.5.: Super-resolution fluorescence microscopy of the chromosome of an *E. coli*. The bacterial cell is immobilized by two optical traps positioned at its end caps. Diffraction-limited fluorescence image (**b**), and super-resolution fluorescence images before (**a**) and after (**d**) deconvolution using the position distribution function (**c**). **e**, The cross sections shown in the insets demonstrate an increased spatial resolution of better than $100\,\mathrm{nm}$ for the labeled nucleoid structures following successful deconvolution.

of the super-resolution images reveals multiple nucleoids within a single cell. It has recently been shown that the nucleoids show heteromeric substructures which are typical for a particular stage in the cell cycle [192]. Clearly, these heteromeric substructures of the *E. coli* chromosome are visualized in the super-resolution images of optically trapped *E. coli* (Figure 4.5d).

4.4.2. Feasibility

To verify that similar structures are observed in trapped and attached cells, *E. coli* are initially held in suspension and then pulled onto the coverglass by the optical traps. *d*STORM images recorded under these conditions show consistent structures in both cases (Figure 4.6a,b).

Rotational Brownian motion inside the optical traps can be evaluated using a series of white light images (Figure 4.6c). A bead of 8.18 µm nominal diameter is held by an optical trap. For this sample, it is possible to observe an inner structure in white light images. Its position changes over time and shows a rotation of the bead inside the trap. This is possible as the bead possesses an almost homogeneous inner structure and can be approximated by a rotational invariant object, such that the optical traps do not restrict rotational motion.

In contrast to the trapped beads, no obvious structure is visible in the white-light images of the trapped *E. coli* bacteria. In this case, a series of *d*STORM images is used to evaluate the rotational motion of a bacterial cell held by two optical tweezers at its end caps (Figure 4.6e). A number of 20 395 localizations in 15 224 raw images is split up into four quarters with an equal amount of localizations in each. Their sum results in the complete *d*STORM reconstruction. Comparing the quarters with the complete reconstruction shows that similar structures are observed in each image while slight differences presumably result from the stochastic nature of the *d*STORM data acquisition. In contrast to the beads, the *E. coli* cells do not exhibit apparent rotational Brownian motion inside the optical traps during the *d*STORM imaging process which in this case took about 90 s. Presumably, rotational motion is frustrated by the interaction of the elliptically shaped trap focus with the inner structure of the cells that features small refractive index gradients throughout parts of the cellular volume. From these observations it can be concluded that rotational Brownian motion does not significantly affect the *d*STORM images of the optically trapped bacteria.

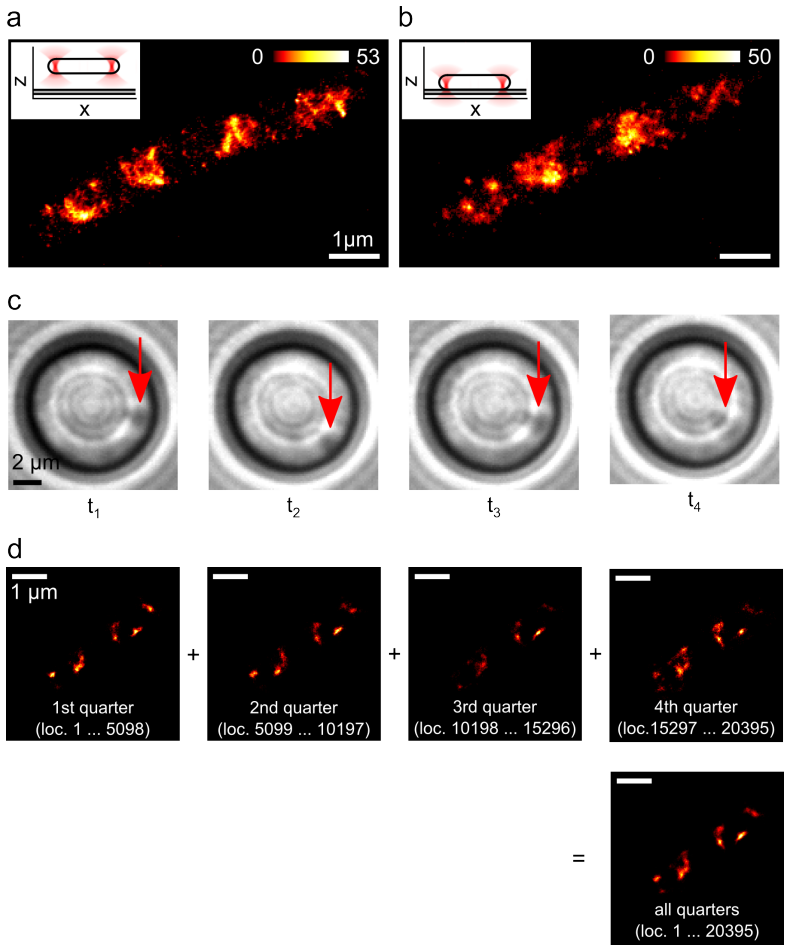

Figure 4.6.: a,**b**, *d*STORM images of the same *E. coli* during optical trapping and after deposition on a substrate: deconvolved *d*STORM image of the optically trapped sample (**a**) and *d*STORM image of the sample attached to a coverslip (**b**). Similar structures can be observed in the optically trapped bacterium compared to the same cell stuck to the cover slip. Subtle differences are likely due to bleaching as the images were acquired subsequently. **c**, Image sequence of a bead which is held by one optical trap. The marked structure changes its position over time and indicates rotational motion of the bead inside the trap. **e**, In contrast, no apparent rotation can be found for trapped *E. coli* held by two traps during the *d*STORM imaging process of about 90 s.

4.5. Multiple perspectives by controlling the sample orientation

4.5.1. Investigating nucleoids from orthogonal directions

The benefit of being able to adjust the sample's alignment relative to the image plane can be used to consecutively image the same sample at different orientations: An *E. coli* cell is first held horizontally, i.e. parallel to the focal plane (Figure 4.7a), and *d*STORM data is recorded (Figure 4.7b). Subsequently, one trap is switched off. This forces the bacterial cell to align vertically along the trap axis, caused by its rod-like shape following the form of the Gaussian laser beam waist in the axial direction (Figure 4.7c). The lower end cap of the *E. coli* cell is then pushed onto the coverslip, followed by a second acquisition of *d*STORM data (Figure 4.7d). By this means, three-dimensionally super-resolved information of a specimen can be gathered, where each single image reaches the isotropic high resolution of two-dimensional SMLM. This feature enables bypassing the inherently poorer spatial resolution along the optical axis of many 3D localization microscopy implementations. This could be even more important in combination with fluorescent proteins, which emit substantially fewer photons than synthetic dyes and yield poor axial resolution in 3D localization schemes.

For interpretation of the data, it must be taken into account that a reconstructed localization microscopy image shows a projection of the emitter's position in the axial direction within a certain volume around the focal plane that can span throughout the entire *E. coli* chromosome. Hence, aligning one axis of a sample parallel to the focal plane in a first step results in limited information about the radial emitter distribution around that axis, but this is achieved in the second step after aligning that axis orthogonal to the focal plane. The orthogonal alignment indicates that the nucleoid is located heterogeneously along the radial direction (Figure 4.7d). Significantly lower DNA concentration is found near the center of the bacterium, while the DNA concentration (determined by the number of *d*STORM localizations) is increased at a distance of about 200 nm to 380 nm from the center (Figure 4.7e).

4.5.2. Highly resolved measurement of DNA structure sizes

The parallel alignment of *E. coli* reveals distinct hetero-structures of the nucleoid along the long axis (Figure 4.5d, Figure 4.7b), which have been observed by

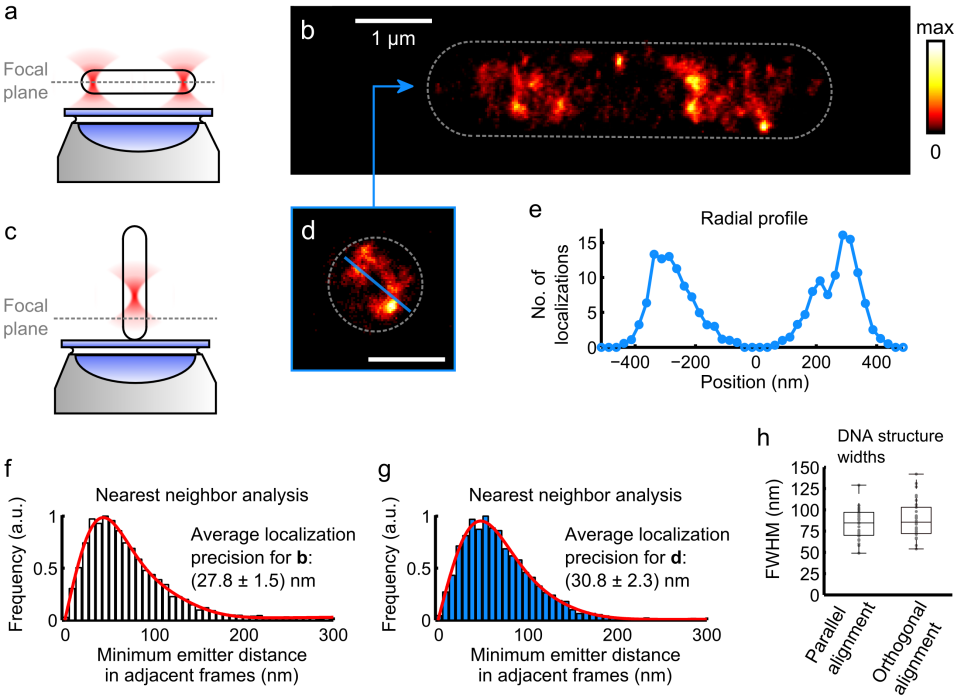

Figure 4.7.: **a**,**c**, Holographic optical tweezers allow for super-resolution imaging of the same sample arranged in different orientations with respect to the focal plane. **b**, Horizontal alignment reveals distinct structures of the labeled nucleoid DNA. **d**, Vertical alignment indicates a heterogeneous distribution in the radial direction as well, with decreased density near the center of the cell (**e**). The approach of combining *d*STORM and optical trapping allows for isotropic super-resolution of two-dimensional localization microscopy for each orientation of the sample, in this case with effective localization precisions of about $28\,\mathrm{nm}$ (**f**) and $31\,\mathrm{nm}$ for (**g**) for the two orientations. **h**, Measuring the structure widths of the DNA filaments in multiple *E. coli* shows a median FWHM of $84.5\,\mathrm{nm}$ ($\mathrm{n} = 30$) for the parallel and $85.5\,\mathrm{nm}$ for the orthogonal sample alignment ($\mathrm{n} = 30$).

*d*STORM before [192]. The reason for the tube-like structure of the nucleoid, which was revealed by measuring in orthogonal alignment, remains unclear. Compaction of DNA into thicker filaments is facilitated by entropic effects and nucleoid associated proteins [50]. Pelletier et al. have hypothesized that these filaments follow a bead-on-a-string formation with an estimated bead size of 130 nm to 440 nm [151]. From the measurements of optically trapped *E. coli*, a median FWHM of the highly resolved DNA filaments of approximately 85 nm is found in both, parallel and orthogonal alignment of the cell, a value that is close to the lower bound of the reported bead size (Figure 4.7h).

4.6. Setup modification for dynamic measurement of protein DNA interaction

4.6.1. Studying DNA repair on a single molecule level

SMLM imposes high demands on the camera in terms of frame rates and sensitivity, which is met by utilizing an EM-CCD camera in the setup combining holographic optical trapping and *d*STORM. These requirements on the detector correspond with the demands for single emitter tracking. Accordingly, the setup can also be used for tracking of fluorescently labeled particles at high temporal resolution as well as high spatial precision. Several amendments particularly with respect to the sample preparation and support (Figure 4.8a) enable the study of DNA-protein interaction during DNA-repair.

Damages in the DNA molecule can arise from chemical additions or disruptions. These can lead to mutation or genomic instability which is believed to drive the development of cancer as well as aging [64, 93, 94]. To prevent these effects, cells rely on a network of proteins for detection and repair of DNA damage, such as the protein hOgg1 [22, 160]. Investigating the phenomenon of DNA repair at high temporal resolution and high spatial precision can help gaining deeper inside into the relevant mechanisms, as DNA repair proteins are considered as targets for cancer therapeutics [91]. Former studies on dynamic DNA repair by proteins have used a constant flow to stretch the DNA strands or have used quantum dots or antibodies for labeling to achieve high fluorescent signals [19, 21, 54, 188]. As disadvantages, these approaches exert constant forces on the proteins by drag from the flowing solution and the protein mass as well as the hydrodynamic radius can be significantly increased.

4.6.2. Realization for low interference with biophysical process

To overcome these drawbacks, organic dyes were covalently attached to the proteins in order to provide fluorescent labeling without remarkably changing the biophysical parameters. Furthermore, optical trapping was used instead of flow for DNA stretching. This was achieved by attaching one end of double-stranded DNA via biotin-streptavidin linkage to the coverslip. The other end was attached via digoxigenin-anti-digoxigenin linkage to a polystyrene bead. Optical trapping of this bead allows for stretching of the DNA when the optical trap and the coverslip are moved relative to each other. Though the possiblity to dynamically position the optical trap allows to perform this stretching without additional equipment, it has emerged that keeping the trap position stable but moving the sample stage gives greater precision during the process of stretching the DNA. A three-axes piezo stage was added to the setup for this purpose and also to allow for precise focusing. Additionally, the setup was equipped with a syringe pump to provide the different reagents to a flow chamber during the sample preparation. Performing the experiment inside a flow chamber also allows for quick changing of the experimental parameters, e.g. varying the concentration of proteins or salts.

4.6.3. Experimental verification of applicability

The use of polystyrene beads of 1 µm to 2 µm diameter causes the DNA strand to be mainly stretched within the evanescent field of the TIRF excitation (Figure 4.8b,c). This illumination mode was chosen because it resulted in high signal-to-background ratios that allowed for tracking of hOgg1 proteins interacting with the DNA. The proteins were tagged with single dye molecules and could be followed during their scanning of the DNA over multiple tens of seconds at a mean precision of 31 nm (Figure 4.8e,d). This proof-of-concept shows the possiblity to investigate DNA-repair proteins of different structures and to provide an understanding of the underlying scanning mechanisms.

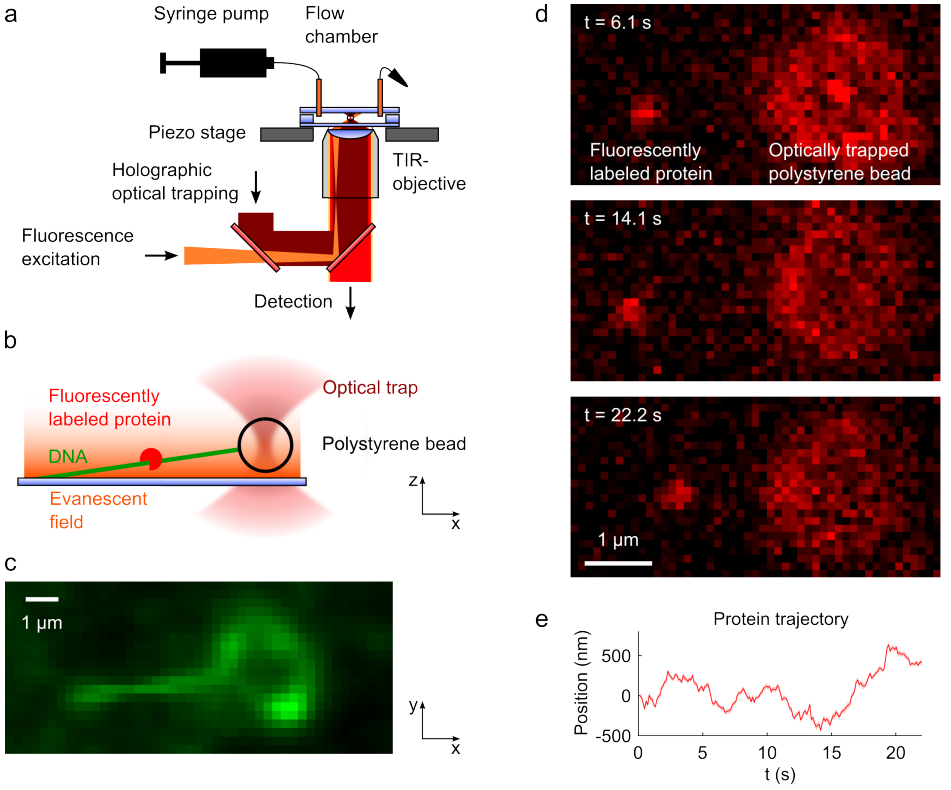

Figure 4.8.: **a**, Retrofitting of the setup shown in Figure 4.1 extends the capability to study dynamic DNA-protein-interaction. The microscope is equipped with a three-axes piezo stage for precise controlling of the sample position. Mounting a flow chamber to it enables to perform a part of the sample preparation directly on the microscope by flowing the respective reagents subsequently into the chamber by a syringe pump. **b**, Double-stranded DNA is anchored with one end to the coverslip and with the other end to a polysterene bead that is being held by an optical trap. Movement of the coverslip and the trap relative to each other allows for stretching of the DNA in the evanescent field of the TIRF excitation. Accordingly, fluorescently labeled proteins can be detected with high signal-to-background ratios when they interact with the DNA strand. **c**, A Yoyo-1 stained DNA strand is stretched by the aid of an optically trapped bead. **d**, Three frames from a recording of hOgg1 scanning a DNA stand. **e**, The fluorescently labeled protein is tracked at a mean precision of $31\,\mathrm{nm}$ and it trajectory along the stretched DNA strand can be followed for more than $20\,\mathrm{s}$.

4.7. Discussion and outlook

The combination of *d*STORM and holographic optical trapping has enabled the investigation of the *E. coli* nucloid under different viewing angles at super-resolution. Other techniques also offer the ability to gather super-resolved 3D images, as for instance 3D-SIM. Though 3D-SIM provides the ability to observe multiple layers orthogonal to the focal plane, e.g. the long *E. coli* axis, it cannot provide isotropic spatial resolution because the axial resolution is approximately a factor of three lower than its lateral resolution [176]. A similar disadvantage also applies to many implementations of 3D localization microscopy, which also suffer from anisotropic resolution, often worse in the axial direction [98, 150]. With the combined HOT and *d*STORM system, this drawback is overcome by its ability to freely align samples with respect to the image plane. Though not providing the opportunity to render a full 3D image, realignment of the sample allows for uniform super-resolution imaging of conventional two-dimensional SMLM in planes parallel and orthogonal to their respective axes.

Immobilization and handling of suspension cells by optical tweezers is in principle also compatible with other super-resolution imaging methods and opens up new opportunities to image and track cellular structures and interactions on the nanoscale when applied to live-cell imaging. Furthermore, the combination of optical trapping and sensitive detection enables the use of this setup to study the dynamic process of DNA repair by individual proteins under different conditions at high temporal and spatial resolution.

5. Cost-efficient solutions for localization microscopy

This chapter is based in major parts on the manuscript

R. Diekmann, K. Till, M. Müller, M. Simonis, M. Schüttpelz, and T. Huser. Characterization of an industry-grade CMOS camera well suited for single molecule localization microscopy – high performance super-resolution at low cost. *Scientific Reports*, in print, 2017.

Section 5.7 gives an outlook to the manuscript in preparation

H. Mao*, R. Diekmann*, H. Liang*, V. Cogger, D. Le Couteur, G. Lockwood, M. Schüttpelz, T. Huser, V. Chen, and P. McCourt. Liver endothelium and platelets studied by cost-efficient super-resolution microscopy (in preparation, 2017).
(* equal contribution)

Many commercial as well as custom-built fluorescence microscopes use scientific-grade cameras that represent a significant share of the instrument's cost. This holds particularly true for SMLM where high demands are placed especially on the detector with respect to sensitivity, noise, and also frame rates. An industry-grade CMOS camera is presented as a cost-efficient alternative to a commonly used scientific-grade camera and carefully characterized. Direct experimental comparison of these two detector types shows widely similar performance for *d*STORM imaging and high image acquisition speeds are demonstrated for this CMOS detector by ultra-fast super-resolution imaging. Simulations show that imperfections of CMOS detectors can be partially compensated. Furthermore, two CMOS cameras are used in a custom-built, cost-efficient multi-color setup to study plasma-membrane fenestrations in LSECs.

5.1. Introduction

A significant advantage of SMLM over other approaches to super-resolution microscopy such as SIM [87, 80] or STED [88] is the relatively low technical effort while possibly the highest resolution enhancement can be achieved. Simple wide-field sample illumination as well as detection is sufficient, which relaxes the demand on the microscope design. If efficient photoswitching of organic dyes or fluorescent proteins is required, such as in *d*STORM or PALM, the use of high illumination intensities is beneficiary. Hence, powerful light sources are preferred, which might be fulfilled by the use of costly lasers. Furthermore, the collection and detection of as many photons as possible is desirable, as this directly influences the localization precision (cf. equation (2.15)). Accordingly, the use of objective lenses with a high NA as well as sensitive detectors are required, which can also be accompanied with the need for expensive investments.

However, multiple cost-efficient alternatives to traditional equipment have recently been demonstrated. Additionally, technical advancements further relax the demands on the microscope components. The use of cheap laser diodes that are coupled through a multimode fiber can lead to a significant cost reduction in *d*STORM setups as shown by Kwakwa et al. [118]. It is also possible to excite with less powerful lasers than usually required in *d*STORM. For instance, other approaches to localization microscopy like PAINT [182], DNA-PAINT [178], or HIDE [196] feature inherent blinking independent of the excitation intensities. Many implementations of SMLM use costly TIRF objective lenses with high NAs. It is of course possible to exchange these with cheaper lenses of lower NA, but this directly compromises the localization precision as discussed in section 3.6, and might lead to the loss of TIRF capability.

Besides the illumination source and the objective lens, the detector has a major share in the microscope cost for SMLM. As the fluorescent signal of single emitters has to be detected with sufficiently high signal to noise ratios (SNR), sensitive and low-noise photon detectors are a prerequisite for fluorescence detection. This was achieved by using EM-CCD cameras in the first realizations of SMLM [18, 168, 85]. The advent of SCMOS cameras resulted in a gradual replacement of the EM-CCD architecture in many SMLM implementations [159, 174, 99, 126, 102, 129, 196]. Prime movers of this trend are the usually lower cost and higher frame rates of sCMOS cameras. Furthermore, except for very low signal levels, higher localization precisions can be achieved [99], which is one of the major performance marks in SMLM. This is complemented by the development of advanced fluorophores [37]

and superior imaging buffer compositions [148]. These lead to a significant increase in the brightness of the probes and reduce the demands on the detector to some extent.

While Holm et al. [96] have recently begun to demonstrate the use of a standard CCD camera in a cost efficient SMLM setup, the use of an industry-grade CMOS camera for this purpose was also just demonstrated by Ma et al. [131]. These works have, however, focused on presenting cost efficient setups rather than extensively analyzing the individual components and carefully characterizing the camera performance for SMLM. In the latter publication, the CMOS camera was only theoretically compared to other camera architectures. One drawback of the Sony IMX265 CMOS sensor used there for the frequently preferred magnification of 60× is the rather small pixel width of 3.45 µm. This leads to a suboptimal projected pixel width [200, 138] of 57.5 nm or a loss of 75% of the maximally possible field-of-view in case of 2 × 2 binning to achieve projected pixel widths of 115 nm.

In contrast, this chapter demonstrates the use of an industry-grade camera that uses the Sony IMX174LLJ-C image sensor which features a pixel width of 5.86 µm, leading to projected pixel widths of 97.7 nm in case of 60× magnification. Focusing mainly on its use in SMLM, the industry-grade CMOS camera is systematically compared experimentally and theoretically to a frequently used camera based on the sCMOS architecture [99]. While not making compromises regarding the additional components of the microscope setup or experimental design, the findings reveal that both cameras show comparable performance for conventional *d*STORM imaging.

Building a cost-efficient multi-color microscope, two CMOS cameras can be used due to their low cost. Additional cost saving, e.g. by sparing an optical table, still allows for acquisition of *d*STORM images of the LSEC plasma membrane.

5.2. Industry-grade CMOS and scientific-grade CMOS performance

5.2.1. Optical setup

A custom-built inverted fluorescence microscope setup (Figure 5.1b) was used to compare the performance between the Hamamatsu Orca Flash 4.0 sCMOS camera and the industry-grade IDS µeye UI-3060CP-M-GL Rev.2 CMOS camera (Figure 5.1a) for single emitter localization. By equally dividing the fluorescence signal

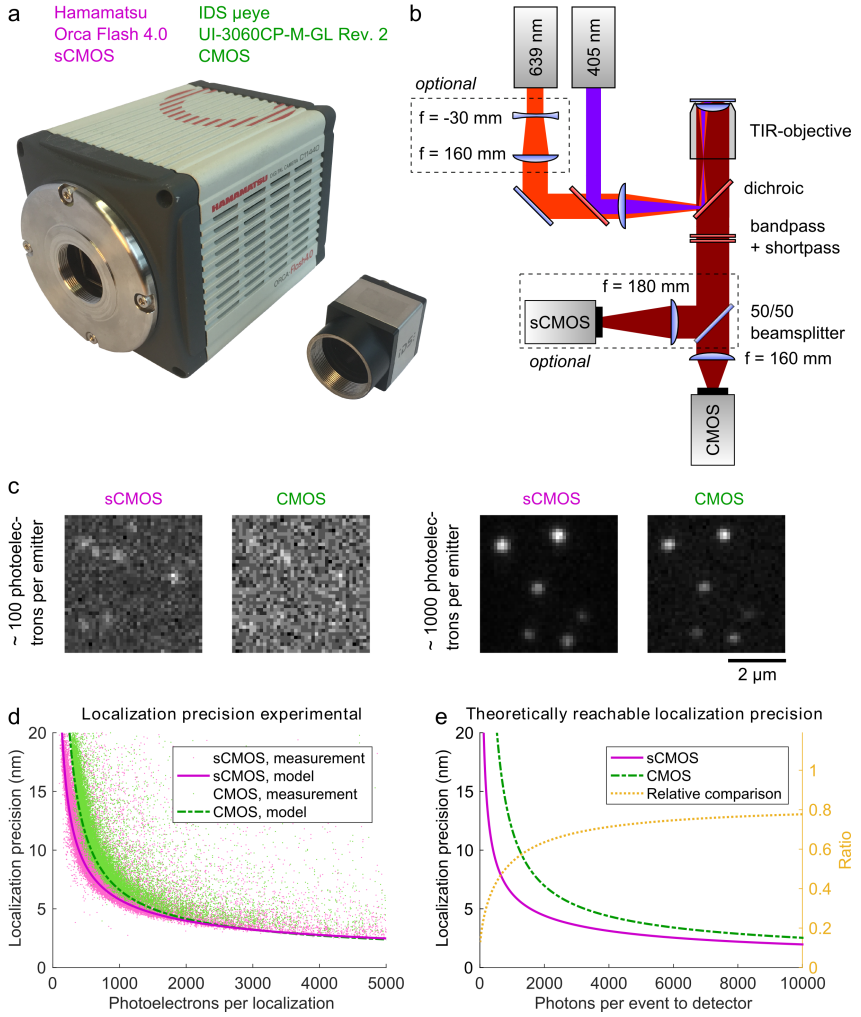

Figure 5.1.: **a**, Photo of the Hamamatsu sCMOS camera and the IDS CMOS camera. **b**, Sketch of the setup used for the camera comparison. The sample is imaged to both cameras by different tube lenses to achieve comparable backprojected pixel widths. **c**, Simultaneous imaging of sub-diffraction sized fluorescent beads visualizes the difference in the signal-to-noise ratio at low photon counts which is less pronounced for higher signals. **d**, Directly measured localization precisions for the two cameras diverge in particular for low photoelectron counts. **e**, Plotting the theoretically reachable localization precision as a function of the photons that reach the detector reveals that the industry-grade camera features more than 20% worse precision for all considered signal levels. This is particularly pronounced for low photon numbers because of the significantly higher read noise of the CMOS camera.

via a 50/50 beamsplitter cube to both cameras, samples were imaged simultaneously by both detectors to allow for a comparison that is as fair as possible. For this case, separate tube lenses of adjusted focal lengths were used for each camera accounting for the different physical pixel sizes of the detectors (Figure 5.1b). In case of the CMOS camera, the use of $f = 160\,\text{mm}$ nominal focal length resulted in measured backprojected pixel widths and heights of 109.7 nm and in case of the sCMOS camera, the use of $f = 180\,\text{mm}$ achieved comparable values for the backprojected pixel widths and heights of 107.5 nm.

5.2.2. Camera-specific parameters affect resolution

Both, sample drift [136] and labeling density (cf. section 3.7) have significant influence on the spatial resolution of SMLM images but are not mainly affected by the detector. Localization precision [45] also significantly determines the obtainable resolution but strongly depends on the specific camera that is being used. To characterize this effect, 30 stacks consisting of 1 000 frames each of immobilized, sub-diffraction sized 100 nm fluorescent beads were recorded at different illumination intensity levels (Figure 5.1c). This allowed to mimic the signal from single fluorophores at photon count rates comparable to raw localization microscopy data and running it through the single emitter detection software [149]. These beads, however, emitted continuously for the entire 1 000 frames such that the localization precision could be measured directly for each bead as the standard deviation of the localized positions.

Among other factors, the localization precision depends on Poisson-distributed photon shot noise and camera noise. As the former is a function of the number of detected photons, the quantum efficiency is an important measure to compare the performance of different cameras. For the deep red spectral range at about 660 nm, the spectral range where a majority of *d*STORM experiments is conducted, the Hamamatsu Orca Flash 4 sCMOS camera features approximately 69% quantum efficiency [82] while the IDS μeye UI-3060CP-M-GL Rev.2 CMOS camera features approximately 48% quantum efficiency [106]. Roughly estimated, the localization precision scales with the inverse of the square root of the number of detected photons per localization (cf. equation 2.13), such that a 20% better localization precision could be expected for the sCMOS camera when only taking these considerations into account. A more detailed evaluation based on the model presented by Mortensen et al. (cf. equation 2.15) that incorporates additional factors predicts an even higher value depending on the number of photons that reach the detector,

e.g. a 35% better precision in case of 5 000 photons and 83% better precision in case of 1 000 photons (Figure 5.1e). Note that these relations change for a different spectral range, e.g. the CMOS camera has a peak quantum efficiency of more than 75% at wavelengths around 500 nm while the sCMOS camera has a peak quantum efficiency of about 72% for wavelengths around 580 nm.

5.2.3. Worse localization precision at low signal levels due to higher noise of CMOS

The CMOS camera features increased camera noise as compared to the sCMOS camera and therefore suffers from an inferior SNR. This becomes visible by the direct comparison between the two cameras at low signal strengths of about 100 detected photoelectrons per emitter (Figure 5.1c). However, in case of about 1 000 detected photoelectrons per emitter, visual inspection of the data reveals more comparable SNRs due to the increased signal. Plotting the localization precision as a function of the number of detected photoelectrons per localization shows the influence of the SNR (Figure 5.1d). At low numbers of photoelectrons per localization, the experimentally determined localization precision of the CMOS camera is significantly worse than the localization precision of the sCMOS camera. E.g. the localization precision is about 9 nm for the sCMOS camera in case of 500 detected photoelectrons while it is about 12 nm for the CMOS camera, and, hence approximately 33% worse. However, the experimentally determined localization precisions converge for about 2, 000 photoelectrons per localization or more.

The model of Mortensen et al. [138] is used to check for consistency of the experimentally determined localization precision. The theoretical prediction coincides with the high density regions of the data points at around 1 000 photoelectrons per localization, while the fit is better for the sCMOS camera. The worse experimental values in comparison to the prediction might be due to the less homogeneous detector in case of the CMOS camera (see e.g. the noise, offset and gain maps in Figure 5.4). At high signal levels of multiple thousands of photoelectrons, the experimentally achieved localization precisions do not reach the theoretically predicted values for either camera, though. This might be due to uncorrected spatial drifts owing to thermal and/or mechanical instabilities of the setup. Additionally, some data points have significantly higher values than the average experimentally determined as well as theoretically predicted localization precision which is possibly due to erroneously detected noise in the single emitter reconstruction algorithmic pipeline. On purpose, the algorithmic parameters of the reconstruction software

were not optimized but the default settings were used to compare the two cameras as impartially as possible.

Please note that while the prediction based on camera parameters only (Figure 5.1e) also considers the cameras' quantum efficiency, Figure 5.1d shows the localization precision as a function of the number of detected photoelectrons, i.e. the quantum efficiency is not considered. Further deviations between the curves can be attributed to different camera properties. For instance, the sCMOS camera itself causes aberrations that broaden the PSF. The theoretically expected value of the PSF FWHM is close to Rayleigh's criterion (cf. equation (3.4)) of approximately 270 nm for this experiment. This is almost reached by the modal value of 271 nm for the CMOS camera but the modal value of 299 nm for the sCMOS camera is about 11% higher. The first presumption was to attribute this effect to aberrations in the beam reflected from the 50/50 beamsplitter. Hence, the sCMOS camera was tested in both the reflection as well the transmission paths behind the beamsplitter and also with four different tube lenses (two times $f = 160\,\text{mm}$ and two times $f = 180\,\text{mm}$). The modal value of the PSF FWHM was close to 300 nm for all tested configurations. It can therefore be concluded that the wider PSF is not induced by the setup but a property of the utilized sCMOS camera itself. The difference in the PSF widths also explains that the curve of the localization precision model (Figure 5.1d) for the CMOS camera falls below the curve for the sCMOS camera for more than about 3 200 photoelectrons as experimentally determined values for the PSF width and noise are used to generate these curves. In contrast, optimal conditions were assumed for the curves shown in Figure 5.1e where the localization precision is better for the sCMOS camera for all photon numbers.

5.3. Comparative dSTORM imaging

The considerations presented so far apply to general single molecule detection-based techniques ranging from, e.g., particle tracking [72] to imaging approaches such as (F)PALM, and (d)STORM. Next, a comparison of the cameras' performance was conducted in the specific case of dSTORM imaging. Again, the signal was split to both cameras and raw data were collected simultaneously. In this manner, Alexa 647 immunostained microtubules in fixed U2OS cells were imaged. Using default parameters for the single emitter fitting algorithm and equal settings for post-processing of both data sets resulted in super-resolved reconstructions of extensive similarity for the two cameras (Figure 5.2a,b). However, 28% more emit-

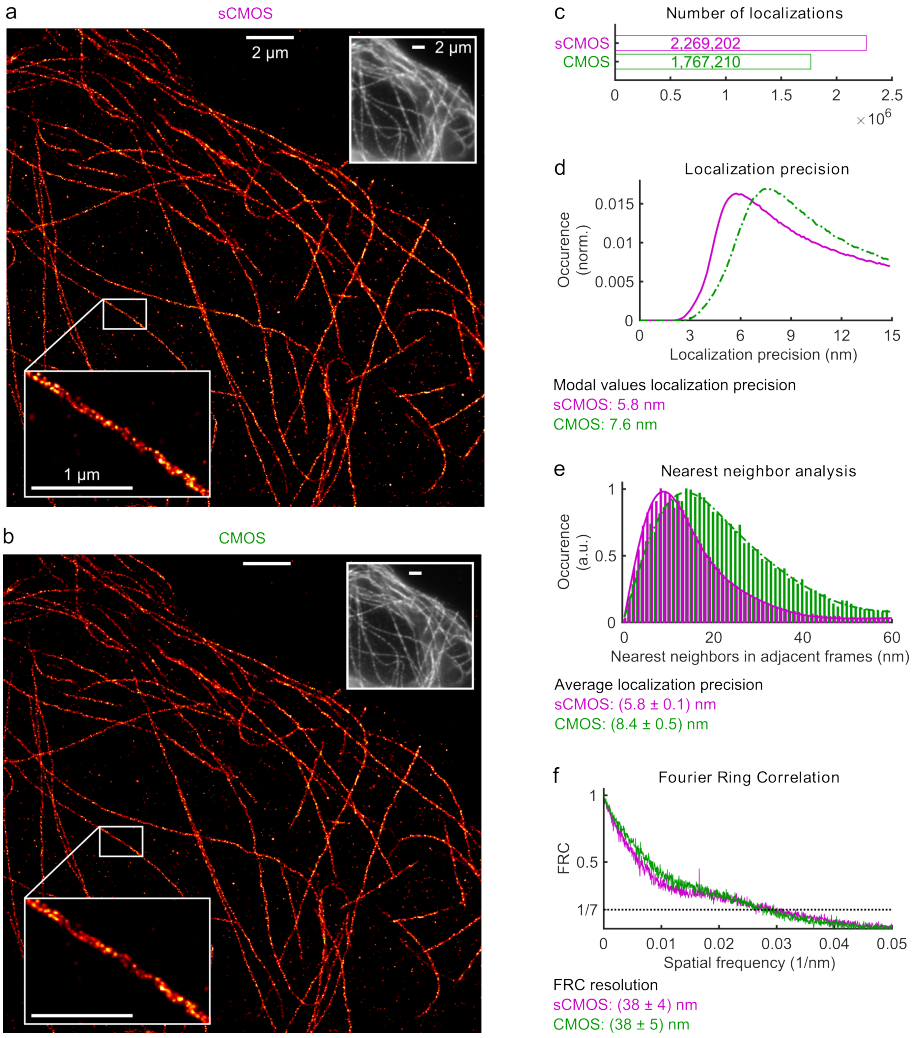

Figure 5.2.: **a**, **b**, Simultaneous *d*STORM imaging of microtubules with both cameras exhibits no significant difference in the reconstructed images (small inset: diffraction limited conventional fluorescence). **c**, Due to its lower quantum efficiency and SNR, fewer localizations are detected from the CMOS camera raw data in the *d*STORM experiment. Both the distributions of the localization precision estimated from the individual signal statistics (**d**) as well as the average value determined from a nearest neighbor analysis on the localizations table (**e**) reveal a slightly worse precision for the CMOS camera. Note that the localizations were filtered for values better than $15\,\mathrm{nm}$. **f**, The FRC resolution for both cameras is on the order of $38\,\mathrm{nm}$, indicating that for this typical *d*STORM experiment the localization precision of the cameras is not the limiting parameter, but rather the spatial frequencies of the stained structure.

ters were detected with the applied algorithmic parameters in case of the sCMOS camera (Figure 5.2c) which is presumably due to its higher quantum efficiency and better SNR. Using the quantitative measure of localization precision, the CMOS camera again performs slightly worse than the sCMOS camera (Figure 1d,e). Both, the modal value of the single emitter localization precision as estimated directly from the signal statistics [159, 138, 149] (Figure 5.2d) and the average localization precision estimated from the analysis of nearest neighboring localizations in subsequent frames [56] (Figure 5.2e), are about 6 nm for the sCMOS camera and 8 nm for the CMOS camera.

It should also be noted that each camera only detected half of the available signal due to the 50/50 beamsplitter, lowering the overall possible localization precision by about a factor of $\sqrt{2}$ (cf. equation 2.13). The spatial resolution obtained by FRC analysis, however, does not show a significant difference and is about 38 nm for both cameras (Figure 5.2f). This suggests that the main factor limiting the achievable spatial resolution is the distribution of the spatial frequencies imposed by the stained sample structure, but not the localization precisions, which is also implied by the similar visual impression of the reconstructed images. Hence, both cameras perform in practical terms equally well for this typical *d*STORM imaging scenario.

5.4. High-speed dSTORM imaging

A significant advantage of (s)CMOS cameras over EM-CCD cameras is their usually much higher maximum image frame rate due to parallel readout. Running the CMOS camera while reading out its full detector size of 1936 × 1216 pixels, the maximum possible stable frame rate was approximately 166 fps (Figure 5.3i) in agreement with the manufacturer specifications [106]. When decreasing the region of interest (ROI) size to 128 × 128 pixels, the image acquisition rate increased to approximately 894 fps. Using sufficiently high intensities of the laser for fluorescence excitation of 33 $\frac{\mathrm{kW}}{\mathrm{cm}^2}$ to 180 $\frac{\mathrm{kW}}{\mathrm{cm}^2}$ and additional UV activation, *d*STORM images can be reconstructed from 10 000 raw frames recorded in 11.2 s seconds (Figure 5.3a,b), comparable to what has been demonstrated earlier by Lin et al. using an sCMOS camera [127]. The line profile (Figure 5.3c) along an immunostained microtubule filament (Figure 5.3b) shows its hollow structure [147, 206, 56, 25, 148], thus indicating a resolution of better than 44 nm (cf. section 3.3). Decreasing the frame rate to 40 fps while keeping the readout illumination constant but deactivating the UV activation (Figure 5.3e,f), the localization precision was improved by a factor

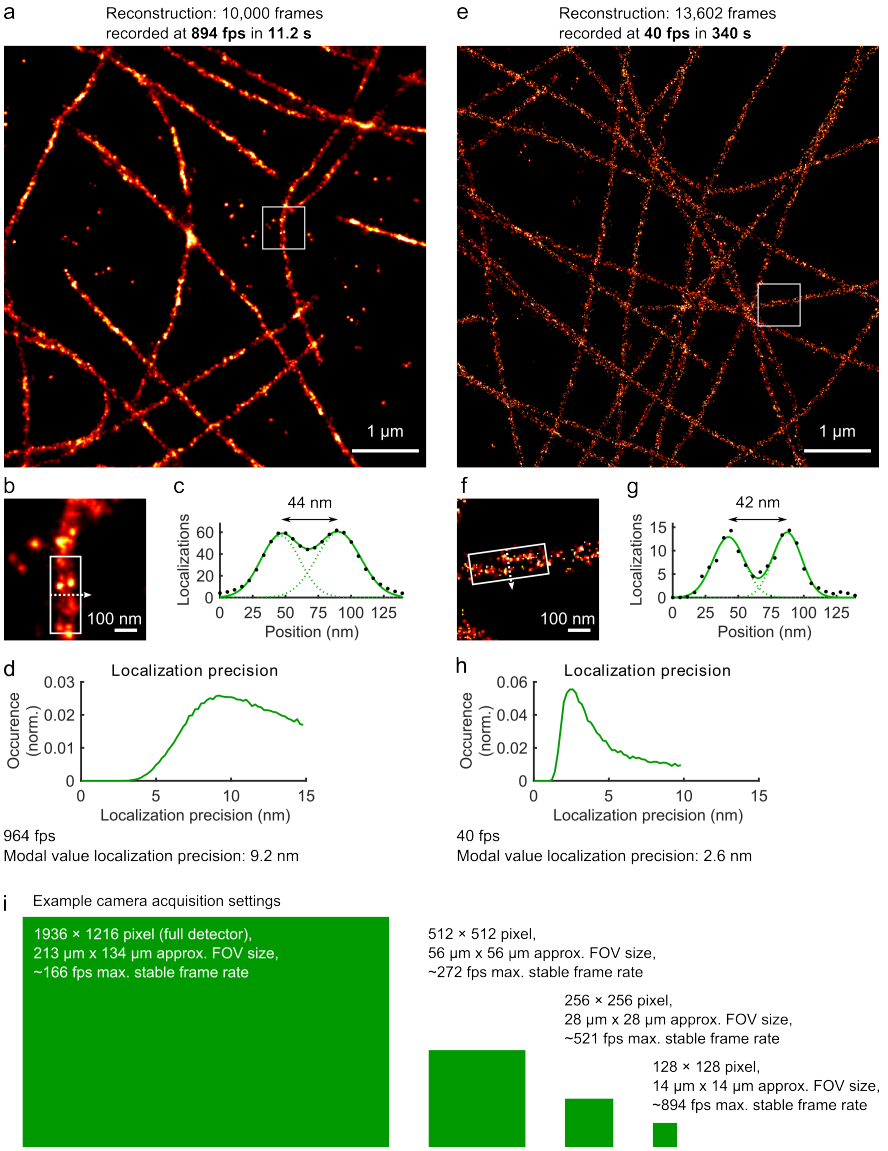

Figure 5.3.: The CMOS camera allows for *d*STORM imaging over a wide range of frame rates and fields-of-view. **a**,**b**, A microtubule image reconstructed from $10\,000$ frames recorded at a rate of 894 fps. **e**,**f** Imaging a similar sample at 40 fps. **c**,**g**, Line profiles along straight microtubules reveal the hollow microtubule structure both for high and low frame rate imaging. **d**,**h**, Localization precisions of about $10\,\mathrm{nm}$ and $3\,\mathrm{nm}$ were achieved. **i**, Depending on the ROI, imaging can be performed at different maximum frame rates.

of 3 to 4 (Figure 5.3d,h) to the modal value of 2.6 nm. Hence, the CMOS camera enables to adjust the frame rate over a wide range that covers a majority of typical SMLM scenarios. Furthermore, the large detector size also permits the use of this camera in large FOV applications [51, 228] (cf. 3.5) at sufficiently high frame rates.

5.5. Detector characterizations

5.5.1. Temperature dependence

Besides the application-based analysis of the camera performances, the camera properties are systematically analyzed. The CMOS camera housing heats up and thermally equilibrates in about 52 minutes to approximately 54 °C when operated at room temperature (Figure 5.4a). An exponential function fits well to the data which gives rise to the assumption that the temperature stabilizes at the asymptotic value of (53.9 ± 0.2) °C. It can be hypothesized that the camera chip reaches an even higher temperature than the housing. Hence, all measurements were conducted after allowing sufficient time for the camera to heat up.

The mean pixel values of the dark detector follow an approximate exponential function of the temperature (Figure 5.4b). However, the highest values are only 1.3 ADU counts above the lowest values, corresponding to approximately 0.62 electrons while the noise rises by about 6% from approximately 6.05 to 6.40 electrons after the camera has warmed up (Figure 5.4c). These and the following characterizations were performed at a frame rate of 40 frames per second (fps) and for a region of 512 × 512 pixels in the center of the chip, which corresponds to an approximate FOV size of 56 µm × 56 µm. In principle, the detector size of 1936 × 1216 pixels would allow for imaging of a FOV of approximately 213 µm × 134 µm (Figure 5.3g).

5.5.2. CMOS detector inhomogeneities in terms of noise, offset and gain

Following the approach as described by Huang et al. [99], the chips of the CMOS and sCMOS cameras were characterized pixelwise for noise, offset, and gain, i.e. the conversion factor from the number of detected photoelectrons to ADU counts by photon transfer curve measurements [110, 125]. In principle, a homogeneous detector in terms of offset and gain is favorable for good performance in SMLM, and low noise values are beneficial.

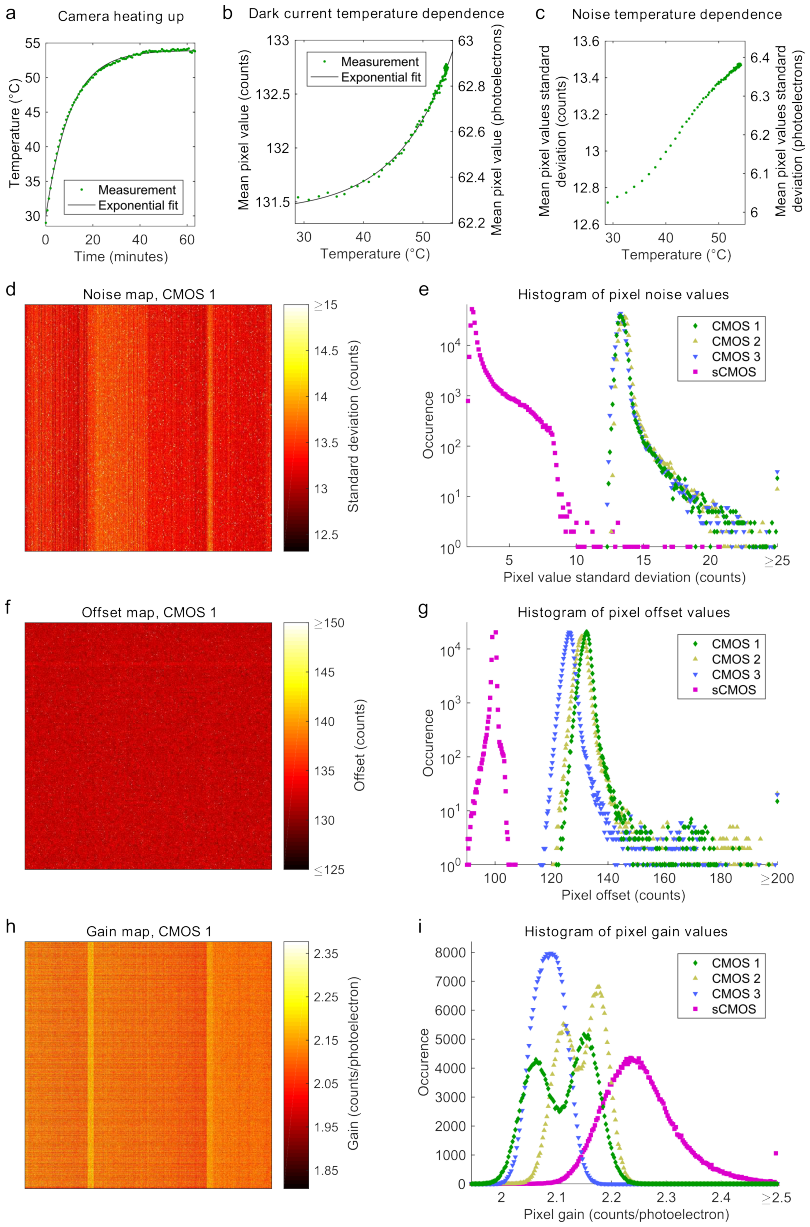

Figure 5.4.: **a-c**, CMOS camera thermal response. **d-i**, CMOS camera noise, offset, and gain maps as well as histograms. Histograms are shown for characteristics of three different industry-grade CMOS cameras of the same model and one established sCMOS camera. In principle, low noise and homogeneous offset and gain characteristics are beneficial.

A pixelwise noise analysis (Figure 5.4d,e) reveals that the majority of the pixels for the IDS μeye applied in the fluorescence measurements of this work (CMOS 1) shows a standard deviation in their dark current of 12.7 counts to 14.2 counts. Some pixels feature higher noise levels, which applies to 0.11% of all pixels. This statistics is confirmed by measuring the same parameter for two further cameras of the same type and manufacturer (CMOS 2 and CMOS 3). Of their pixels, also 0.11% show a standard deviation higher than 14.2 counts (Figure 5.4e). The noise map (Figure 5.4d) visualizes that the elevated pixel noise partially follows a pattern, as prominent stripes are visible. The same behavior was observed for other cameras of the same type. Pixels with elevated noise levels lead to a loss in localization precision in their direct environment [99, 126]. Accordingly, such a pattern supposedly leads to a spatially inhomogeneous localization precision.

This prominent pattern does not show up in the pixelwise offset map (Figure 5.4f), but the map for the pixelwise gain (Figure 5.4h) also shows vertically striped structures. As has been reported earlier [99, 126], the sCMOS camera shows remarkably less noise (Figure 5.4e) and a narrower distribution of the pixel offset values (Figure 5.4g). Both of these characteristics are favorable for better camera performance and these results are consistent with the localization precision measurements (Figure 5.1d, Figure 5.2d,e).

Huang et al. [99] and Lin et al. [126] have extensively discussed the use of (s)CMOS specific reconstruction algorithms. This is possible by altering internal camera data-processing routines and more notably by explicitly taking the maps for pixel-dependent noise, offset and gain into account. However, many researchers successfully reconstruct sCMOS data with nonspecific, standard algorithms [102, 178, 187, 118] that can be chosen from a wide variety of software implementations [170]. Hence, each camera was utilized as is, and data was reconstructed by the ThunderSTORM software [149] because its underlying localization algorithm showed reliable performance using its default settings which were not changed to compare the cameras. The mean values of the offset and gain maps were used in the software settings as explicit camera specific parameters.

5.6. Compensating for CMOS detector inhomogeneities

5.6.1. Former work focuses on noise correction

Huang et al. [99] have extensively discussed that pixel-to-pixel variations of the detector can obscure the single emitter localization and focused on the consideration of noise in a maximum-likelihood-based reconstruction algorithm. The authors have shown that this method can clearly improve the super-resolved reconstruction of raw data acquired with a sCMOS camera. Lin et al. [126] used a different approach that is based on PSF fitting, but also explicitly considers pixel-dependent noise in flat-fielded data. However, this raises the necessity of specific software and is accompanied with an increased computational demand.

As mentioned above, researchers seem to tend to still use not (s)CMOS-specific software for reconstruction of data collected with this camera architecture. Therefore, simulations were performed to investigate a simple method for correction of the raw data to cope with pixel-dependent gain and offset variations, but explicitly not with pixel-dependent noise.

5.6.2. A simple approach to correcting offset and gain variations

Before analyzing the raw data with the widely used, freely available but not (s)CMOS-specific analysis software ThunderSTORM [149], it can be corrected pixel-wise for the offset by subtracting the offset map from each frame. Additionally, ADU counts are converted to photoelectron counts via division by the gain map. The first operation may result in negative pixel values which might not be handled correctly by the reconstruction software, so a uniform offset is added to all frames in a last step. Accordingly, the corrected data that is used as input for the reconstruction software can be written as

$$\mathrm{H}(x,y) = \frac{\mathrm{M}(x,y) - \mathrm{O}(x,y)}{\mathrm{G}(x,y)} + k, \tag{5.1}$$

where (x, y) is the pixel coordinate, M is the measured data, H is the corrected data, O is the offset map, G is the gain map, and k is a positive constant chosen such that all elements of H are non-negative. As this procedure is straightforward and only uses basic mathematical operations, it can be easily performed in common image analysis software, e.g. Image J/Fiji [177].

To verify the applicability of this approach, diffraction-limited imaging of point-like emitters utilizing both cameras was simulated. Simulations considered the measured maps of noise, offset and gain as well shot-noise and the photon binning to pixels. Each emitter position was simulated for 250 frames at 133 225 different emitter position placed on a periodic grid on a detector area of 512 × 512 pixel. Simulations were performed at 200, 1 000, and 5 000 photoelectrons per frame and per emitter, to consider SMLM scenarios of low photon count rates as likely in the case of PALM as well as high photon-count rates as likely in the case of *d*STORM and DNA-PAINT. While the standard deviation of the localized positions over the 250 frames gives the localization precision, the distance between the mean localized position and real emitter coordinates, i.e. the ground truth data gives the localization accuracy.

For each scenario, the single emitter fitting algorithm was run with default settings on three different sets of raw data: (i) the simulated, uncorrected data; (ii) the simulated, but corrected data via Fiji according to equation 5.1; and (iii) data simulated under the assumption of a homogeneous detector with no pixel-to-pixel variations in terms of noise, offset and gain (Figure 5.5g). For the homogeneously simulated data, the mean values of the maps for noise, offset, and gain were used for all pixels.

The distributions of the resulting localization precision show slight differences particularly in the case of 200 photoelectrons per localization, but the general trend points towards similar distributions for the uncorrected , corrected and homogeneous detector data (Figure 5.5b,d,f). This holds for both the characteristics of the CMOS camera as well as the sCMOS camera, though the latter features significantly better localization precisions for all three photons levels, which is likely due to the considerably lower noise (Figure 5.4e), and, hence, higher SNR values. Flat-fielding does not correct for noise and the average noise is equal for all three cases of uncorrected, corrected, and homogeneously simulated data. As no large effect on the localization precision is observed, it can be concluded that localization precision is mainly affected by SNR which is in line with the findings of Thompson et al. [200] and Mortensen et al. [138].

5.6.3. Effectivity

However, the distributions for the obtained localization accuracy show that for all simulated photon levels, the correction for gain and offset variations yielded better accuracies on average (Figure 5.5a,c,e). This holds for both detectors, though

again the sCMOS characteristics show better results, presumably due to the higher homogeneity in terms of pixel offset (Figure 5.4g). Remarkably, the distributions for the corrected data largely converge towards the distributions of the homogeneously simulated data in all cases. This shows a high effectivity of the flat-fielding procedure for the conducted simulations. Nevertheless, this approach requires the knowledge of the true maps for pixel-wise camera gain and offset. As the same maps have been used for simulation as well as correction of the raw data, the pixel characteristics were exactly known by definition.

These results show that by the consideration of the pixelwise offset and gain and neglecting the noise characteristics, it is in principle possible to enhance the localization accuracy. However, when measuring these maps for real detectors, there could be remaining deviations between the measured and the true camera properties due to measurement errors or the underlying assumptions simply being too rough. The effect on real data might therefore be less pronounced as found in the simulations. Anyway, the simulations show that sufficient knowledge of the offset and gain maps can significantly improve the results in terms of localization accuracy, but not localization precision because the method does not correct for noise.

Next, the correction approach was applied to measured data. Because no ground-truth data is available for fluorescent bead experiments, the obtained accuracy cannot be measured. However, Figure 5.5h shows that a pixel with an increased offset attracts the localized positions. The correction shifts the mean localized position by 5.2 nm in this particular case. It should be taken into account that though the offset is remarkably elevated in comparison to the surroundings, the obtained shift is only on the order of or even lower than typically obtained localization precisions in SMLM experiments (cf. Figure 5.5b,d,f), especially at low signal levels. Then again, variations in the offset values supposably play a diminished role at high signal levels, though the influence of gain variations is not expected to depend strongly on the signal levels. Therefore, the significance of the presented correction procedure should not be overemphasized. The correction potentially helps in improving the quality of single emitter localization experiments with (s)CMOS detectors as has been shown by simulations, but this is not an obligatory requirement. Anyway, the easily implementable algorithm allows to enhance the results without the need for (s)CMOS-specific single emitter localizers.

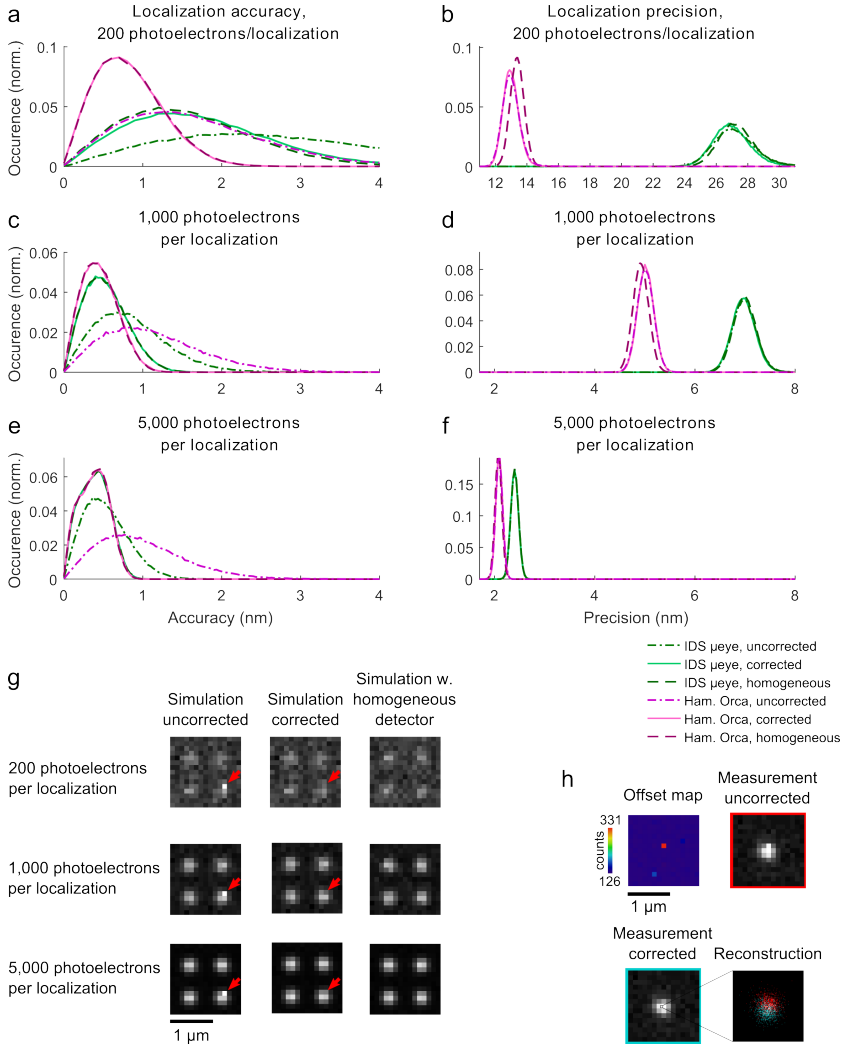

Figure 5.5.: a-f, Results from simulation and reconstruction of single emitter data for (s)CMOS cameras featuring the measured characteristics, with and without correction. While the correction significantly enhances the localization accuracy (**a**,**c**,**e**) for all tested numbers of photoelectrons per localization, the localization precision remains mainly unaffected by the correction (**b**,**d**,**f**). For all photoelectron numbers, the distribution for the corrected data converges towards the distribution of the data when a homogeneous detector is assumed. **g**, Examples from the simulated raw data. A pixel with significantly higher offset than surrounding pixels (red arrow) can easily be seen in the uncorrected data, but is not noticed by eye in the corrected data. **h**, Application to measured data shows that a pixel with elevated offset spatially attracts localizations. Correcting for this effect leads to a mean shift of about $5\,\mathrm{nm}$ in the localized positions.

5.7. Low-cost nanoscopy of LSECs

5.7.1. Super-resolution enables structural analysis of membrane fenestrations

The price of the presented industry-grade CMOS camera is not only well below the price of a scientific CMOS camera but also well below the price of a commercial image splitter. Hence, it is economically efficient to use even two cameras of this type to build a multi-color setup. For the project presented in this chapter, this strategy was followed to provide a cost-efficient microscope without significantly compromising the performance for dual-color TIRF imaging. Furthermore, it should feature the possibility to be upgraded to more colors later. The resolution of the system was specified to be good enough to perform a fenestration size analysis in LSECs, hence it should feature a resolution as small as about 50 nm [27]. Additionally, operation and alignment of the system must be possible to users with limited experience in optics.

For these reasons, it was decided to build a *d*STORM setup as it best covers the demanded aspects, e.g. in comparison to SIM or STED. Assembly of the microscope needed to be conducted in a laboratory without the possibility of having parts custom-made. Hence, the majority is built from commercially available parts. The few exceptions are the plate supporting the sample and five threads that were removed by drilling in the mechanical workshop of a hospital.

5.7.2. Optical setup

The setup uses two solid-state lasers that emit at 488 nm and 647 nm, respectively (Figure 5.6). The latter was bought as a fiber-coupled device to allow for easy handling. After adjusting the beam diameters using a collimation lens and telescopes, the beams are overlaid via a dichroic mirror and focused onto the back-focal-plane of a TIRF lens for sample illumination. Mounting appropriate parts of the illumination unit on a translateable stage allows for easy switching between epi, HILO, and TIRF configuration. The system has enough degrees of freedom such that both lasers can be optimally aligned to illuminate the sample that is mounted on an xy-stage. Focusing is performed by a z-stage that holds the objective lens. The fluorescence emission is separated from the excitation by a dichroic mirror and the emission is further separated by another dichroic beam-splitter.

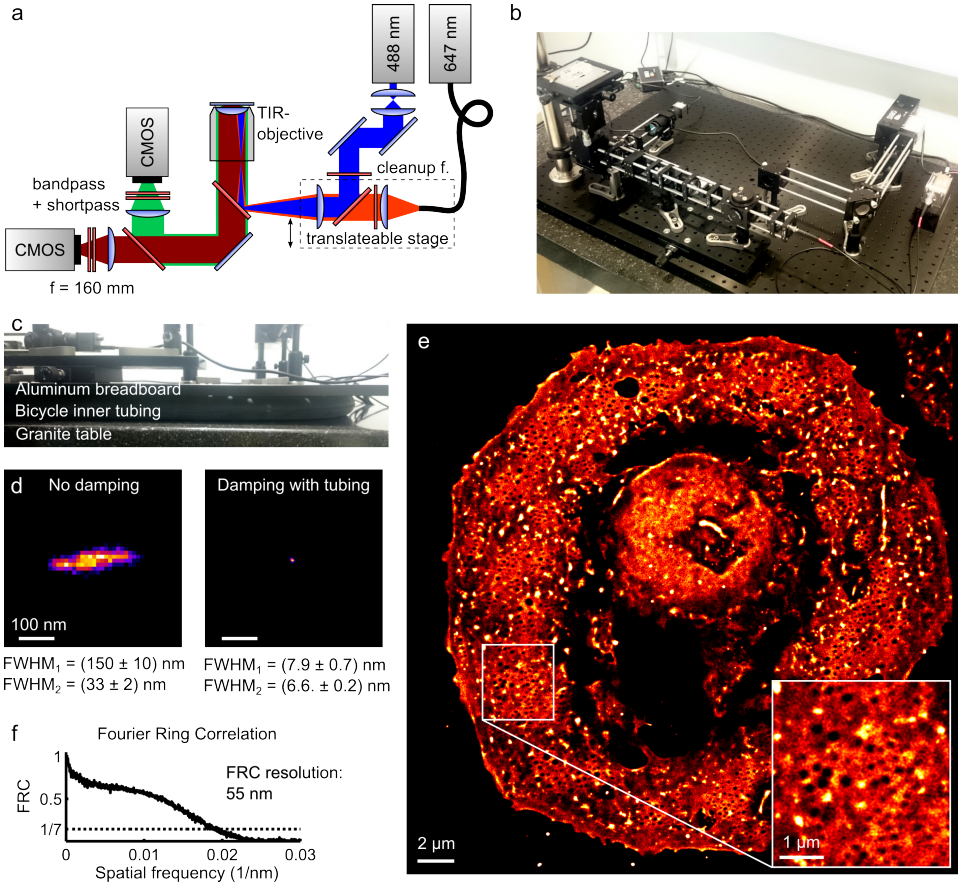

Figure 5.6.: **a**, Sketch of the custom-built setup for low-cost SMLM. Two CMOS cameras are used for fluorescence detection that can be excited via epi, HILO and TIRF illumination at two different wavelengths. **b**, The implementation leaves space for the integration of further wavelengths while the use of two cameras allows for simultaneous widefield imaging. **c**, Using a bicycle inner tubing for vibration damping significantly contributes to cost efficiency and effectively inhibits motion blur in the localization of single emitters (**d**). **e**, The application of this microscope to *d*STORM of the LSEC plasma membrane visualizes fenestrations at a FRC resolution of $55\,\mathrm{nm}$ (**f**).

Each detection path features its own tube lens of $f = 160\,\mathrm{nm}$ focusing the image to the camera at backprojected pixel widths of about 110 nm. In this way, the dichroic beam-splitter transmits and reflects, respectively, the collimated beams of the fluorescence signal. This alternative is preferred over using a single tube lens that is placed in the beam path before the dichroic mirror. Arimoto et al. have discussed how a tilted glass plate in a medium of lower refractive index medium (in this case air) can cause serious aberrations when transmitting a focused beam [9]. This effect is avoided by transmitting the collimated beam which gets only displaced laterally but not aberrated.

5.7.3. A simple alternative to an optical table

The setup is mounted on a breadboard of $0.9\,\mathrm{m} \times 0.6\,\mathrm{m}$ footprint (Figure 5.6b), hence, it can easily be transported. Sparing an optical table also contributed significantly to a cost reduction in comparison to conventional setups. However, placing the breadboard directly on a granite table that was in contact with a wall housing the laboratory's air-conditioning system caused serious vibrations. The impact on the imaging was measured by using fluorescent beads as position sensors that can in principle by localized with very high precision due to their high brightness. Without damping, the vibration caused relative motion between the sample and the camera that resulted in effective amplitudes up to 270 nm. Charaterization of this motion by the FWHM of the beads localization distribution at a high frame rate resulted in values of $(150 \pm 10)\,\mathrm{nm}$ and $(33 \pm 2)\,\mathrm{nm}$ in orthogonal directions (Figure 5.6d). This motion of the sample around a mean position would lead to a significant decrease in the effective localization precision similar to residual Brownian motion of optical trapped samples (cf. section 4.2).

It turned out that placing a bicycle inner tubing between the breadboard and the optical table (Figure 5.6c) leads to a significant damping of the vibration. Accordingly, the FWHM of the beads localization distribution resulted in values of $(7.9 \pm 0.7)\,\mathrm{nm}$ and $(6.6 \pm 0.2)\,\mathrm{nm}$ in orthogonal directions which is on the order of the localization precision of bright single emitters. Thus, the vibration was weakened by about a factor of 5 to 18 by this simple action and the resulting bead localization FWHM is 33% to 45% better than what has been reported for another cost-efficient SMLM setup [131].

5.7.4. Capability

Figure 5.6e shows the application of this microscope to *d*STORM. The DiD-labeled membrane of a LSEC was imaged in 40 000 frames where $4.6 \cdot 10^6$ individual emitters were localized. The resulting reconstruction features an FRC resolution of 55 nm (Figure 5.6f) and a mean localization precision of 15.8 nm. Using the definition of equation (2.21) for the resolution based on localization precision and localization density gives a resolution of 46.6 nm. Hence, the specification of enabling super-resolution imaging of LSECs at sufficient resolution for fenestration size analysis was achieved with this cost-efficient setup.

5.8. Discussion and outlook

The industry-grade IDS μeye UI-3060CP-M-GL Rev.2 CMOS camera has been thoroughly evaluated and compared to the established scientific-grade Hamamatsu Orca Flash 4.0 sCMOS camera. While these specific models have been tested for their performance, both detectors are used in multiple commercially available camera models by different manufacturers. Hence, the results presumably apply not only to two specific models, but to families of cameras.

The presented approach of using the exact same methods for characterization and a custom setup that enables simultaneous imaging of the same sample by both cameras allows for a fair comparison of their overall performance. Hence, this method is generally applicable to run competitions between different detectors. For this work, the first generation of the Hamamatsu Orca Flash sCMOS camera was used, while the third generation has recently become commercially available.

Though some differences in their performance can be expected, the utilized first generation camera already shows superior performance when compared to the industry-grade CMOS camera particularly with respect to noise and quantum efficiency in the deep red spectral range. This leads to an experimentally confirmed higher localization precision for the sCMOS detector at low signal levels where relative differences are on the order of 33% at around 500 photoelectrons per localization but become less pronounced for more than 2 000 photoelectrons per localization. A few nanometers difference in the localization precision is not supposed to play a major role for many biological questions anyway. Consequently, *d*STORM imaging of biological samples showed no substantial difference in the FRC resolution. It can therefore be concluded that for *d*STORM scenarios such as imaging the popular dye Alexa 647, here demonstrated for microtubule labeling, it

is possible to resort to the tested CMOS camera without considerable drawbacks.

Lower signal levels are more common in case of different SMLM scenarios such as *d*STORM with inferior dyes like DiD, worse localization precision on the order of several nanometers need to be accepted, but still allow for imaging at resolutions on the order of 50 nm. Additionally, different probes often emit at shorter wavelengths where the CMOS camera features a quantum efficiency that is as far as 63% higher relative to the deep red spectral range, counteracting the effect of lower fluorescence signals, for instance of fluorescent proteins.

Optimizing the imaging conditions, the experimentally obtained localization precision is about 3 nm. This is easily on the order of label sizes (e.g. if antibodies are used) or residual drift effects even after correction, and, therefore, no remarkable difference for the considered camera types is expected.

This work used a custom setups with approximately 53× magnification for the CMOS camera, but the convenient pixel size of the presented CMOS detector also allows for its easy integration at projected pixel widths of 97.7 nm into microscopes with the frequently used 60× magnification. As it is connected via USB 3.0, it can simply be controlled by standard contemporary computers without the need for additional hardware. The camera size and weight are considerably smaller than that of commercially available sCMOS cameras which may make it a preferred choice in compact and mobile setups. The latter is also favored by the lack of moving parts, e.g. fans. The additional I/O connector can be used for camera triggering. Hence, multiple cameras can easily be used in a synchronized manner, e.g. for multi-color imaging. The low cost makes it economically reasonable to integrate a second camera instead of a commercial image splitter. Combination with other approaches to cost-efficient building of custom setups enables to remarkably lower the price of super-resolution microscopy in comparison to commercial instruments. For instance, it is easily possible to replace a costly optical table by a bicycle inner tubing without considerably compromising the effectivity.

While this chapter has focused on the use in SMLM, the CMOS camera properties also promise a highly efficient use in other approaches to high- and super-resolution microscopy. Certainly, novel industry-grade CMOS detectors with even superior quality will become available in the future. For instance, the Sony IMX250 CMOS sensor has substantially less read noise and will enable a larger FOV at the same magnification. However, it features lower peak quantum efficiency, a suboptimal pixel width and a decreased frame rate for full chip readout. Nevertheless, properties of industry-grade CMOS cameras will presumably further approach the fundamental limits toward which scientific-grade cameras are already converging

against today. Hence, the differences for new detector generations will probably become even fewer. In any case, the results show that even with the tested cameras and depending on the scenario, differences in the performance of the CMOS and the sCMOS camera can be vanishing and may not be relevant for biological applications.

6. Comprehensive outlook

This work demonstrates concepts for enhancing throughput, flexibility, and cost-efficiency in super-resolution microscopy and particularly SMLM. The combination of super-resolution microscopy with waveguide-based excitation can contribute to a remarkable increase in throughput and gives flexibility in the choice of the imaging modality. So far, waveguide-based SMLM experiments have focused on the application of *d*STORM. Using the more advanced approach of DNA-PAINT [178] can potentially further enhance the spatial resolution. This might be possible both by increasing the localization precision due to higher photon counts per localization and by straightforward control over the number of simultaneously active emitters due to its widely linear dependence on the label concentration in the imaging buffer.

Modifications of the waveguide architecture that give better control over the excited modes and interference patterns will enable the integration of further approaches to nanoscopy, such as linear SIM [80, 87] and non-linear SIM [162]. Even for linear SIM, the high effective refractive index of waveguide materials [6] can enable a resolution enhancement for the reconstructed fluorescence image beyond a factor of two [90] at temporal resolutions that are well-suited for live-cell experiments. Furthermore, the preparation of waveguides on transparent substrates, e.g. conventional coverslips, will allow for the use of inverted microscopes for fluorescence detection. Accordingly, this technique could be combined with other illumination schemes that additionally provide highly resolved 3D information either in close proximity to the surface [33] or in large volumes [32]. Anyway, evanescent excitation makes waveguide-based imaging a particularly suited choice for membrane [27] or endocytosis studies [156]. Partially coherent excitation either by the presented approach of using a diffuser [51] or using dynamic speckle patterns from multi-mode fibers [44] will allow for highest temporal resolution. The combination with the large FOV has the potential to perform live-cell imaging of membrane-related processes while observing a large number of events simultaneously, thus unifying high throughput and high temporal resolution. Alternatively, the combination with novel 3D localization schemes [25, 43] can also enable SMLM at both high throughput and high spatial resolution.

The large illuminated area in waveguide-based imaging is complemented by the large detector sizes of modern sCMOS cameras, resulting in unprecedented FOVs for TIRF. Replacement with industry-grade CMOS detectors can maintain large FOVs, but enables a significant cost reduction while only low compromises must be made with respect to the performance. Consequently, low-cost setups can be realized even when using multiple cameras [12] which opens up possibilities for advanced detection schemes using multiple simultaneous detections such as spectrally resolved SMLM [226], multiple-plane SMLM [112] or multiple-plane fluctuation-based imaging [69], and 4π SMLM [101]. Other super-resolution techniques relying on widefield detection like 2D SIM [80, 87], 3D SIM [81], SOFI [41], or ESI [222] can also benefit from inexpensive cameras. Besides the use of industry-grade detectors, possible cost reductions without notable performance restrictions are the potential in situ calibration via labeled bead-shells in astigmatism-based 3D SMLM [28] that allows for sparing of a z-piezo or the demonstrated replacement of an optical table.

While waveguide-based imaging increases the flexibility of nanoscopy by offering multiple modalities in the same microscope, the use of holographic optical tweezers gives flexibility with respect to the sample orientation. Though the presentation in this work focuses on SMLM and particle tracking, the combination of multiplexed optical trapping [78] with faster approaches to super-resolution microscopy [34, 117, 181] will enable live-cell imaging of non-adherent samples. In this manner, also contacts between different cells can be induced to study their interaction [135], for instance visualizing the cell-to-cell transfer of HIV [103].

In summary, the presented approaches of waveguide chip-based nanoscopy, the combination of holographic optical trapping with *d*STORM, and cost-efficient SMLM have the potential to contribute to the further wide-spread use of super-resolution microscopy.

Bibliography

[1] E. Abbe. Beiträge zur Theorie des Mikroskops und der mikroskopischen Wahrnehmung. *Archiv für mikroskopische Anatomie*, **9**(1):413–418, 1873.

[2] K. Agarwal and R. Machan. Multiple signal classification algorithm for super-resolution fluorescence microscopy. *Nature Communications*, **7**:13 752, 2016.

[3] B. Agnarsson, S. Ingthorsson, T. Gudjonsson, and K. Leosson. Evanescent-wave fluorescence microscopy using symmetric planar waveguides. *Optics Express*, **17**(7):5075–5082, 2009.

[4] B. Agnarsson, A. B. Jonsdottir, N. B. Arnfinnsdottir, and K. Leosson. On-chip modulation of evanescent illumination and live-cell imaging with polymer waveguides. *Opt Express*, **19**(23):22 929–22 935, 2011.

[5] B. Agnarsson, A. Lundgren, A. Gunnarsson, M. Rabe, A. Kunze, M. Mapar, L. Simonsson, M. Bally, V. P. Zhdanov, and F. Höök. Evanescent light-scattering microscopy for label-free interfacial imaging: From single sub-100 nm vesicles to live cells. *ACS Nano*, **9**(12):11 849–11 862, 2015.

[6] B. S. Ahluwalia, A. Z. Subramanian, O. G. Hellesø, N. Perney, N. P. Sessions, and J. S. Wilkinson. Fabrication of submicrometer high refractive index tantalum pentoxide waveguides for optical propulsion of microparticles. *Photonics Technology Letters, IEEE*, **21**(19):1408–1410, 2009.

[7] C. E. Aitken, R. A. Marshall, and J. D. Puglisi. An oxygen scavenging system for improvement of dye stability in single-molecule fluorescence experiments. *Biophysical Journal*, **94**:1826–1835, 2008.

[8] P. Almada, S. Culley, and R. Henriques. PALM and STORM: Into large fields and high-throughput microscopy with scmos detectors. *Methods*, **88**:109–121, 2015.

[9] R. Arimoto and J. Murray. A common aberration with water-immersion objective lenses. *Journal of Microscopy*, **216**:49–51, 2004.

[10] J. Art. *Handbook of Biological Confocal Microscopy, 3rd edition*, chapter Photon Detectors for Confocal Microscopy, pp. 251–264. Springer, 2006.

[11] A. Ashkin. Forces of a single-beam gradient laser trap on a dielectric sphere in the ray optics regime. *Biophysical Journal*, **61**(2):569–582, 1992.

[12] H. Babcock. Multiplane and spectrally-resolved single molecule localization microscopy with industrial grade CMOS cameras. *bioRXiv preprint*, p. 186544, 2017.

[13] F. Balzarotti, Y. Eilers, K. C. Gwosch, A. H. Gynna, V. Westphal, F. D. Stefani, J. Elf, and S. W. Hell. Nanometer resolution imaging and tracking of fluorescent molecules with minimal photon fluxes. *Science*, **355**:606–612, 2017.

[14] N. Banterle, K. H. Bui, E. A. Lemke, and M. Beck. Fourier ring correlation as a resolution criterion fer super resolution microscopy. *Journal of Structural Biology*, **183**(3):363–367, 2013.

[15] A. Barsic, G. Grover, and R. Piestun. Three-dimensional super-resolution and localization of dense clusters of single molecules. *Scientific Reports*, **4**:5388, 2014.

[16] H. T. Beier and B. L. Ibey. Experimental comparison of the high-speed imaging performance of an EM-CCD and sCMOS camera in a dynamic live-cell imaging test case. *Plos One*, **9**(1):e84 614, 2014.

[17] E. Betzig. Proposed method for molecular optical imaging. *Optics Letters*, **20**(3):237–239, 1995.

[18] E. Betzig, G. H. Patterson, R. Sougrat, O. W. Lindwasser, S. Olenych, J. S. Bonifacino, M. W. Davidson, J. Lippincott-Schwartz, and H. F. Hess. Imaging intracellular fluorescent proteins at nanometer resolution. *Science*, **373**(5793):1642–1645, 2006.

[19] P. R. Bianco, L. R. Brewer, M. Corzett, R. Balhorn, Y. Yeh, S. C. Kowalczykowski, and R. J. Baskin. Processive translocation and DNA unwinding by individual RecBCD enzyme molecules. *Nature*, **409**:374–378, 2001.

[20] A. W. Bisson-Filho, Y.-P. Hsu, G. R. Squyres, E. Kuru, F. Wu, C. Jukes, C. Dekker, S. Holden, M. S. van Nieuwenhze, Y. V. Brun, and E. C. Garner. Treadmilling by Ftsz filaments drives peptidoglycan synthesis and bacterial cell division. *Science*, **355**(17):739–743, 2007.

[21] P. C. Blainey, A. M. van Oijen, A. Banerjee, G. L. Verdine, and X. S. Xie. A base-excision DNA-repair protein finds intrahelical lesion bases by fast sliding in contact with DNA. *PNAS*, **103**(15):5752–5757, 2006.

[22] S. Boiteux and R. J. Base excision repair of 8-hydroxyguanine protects DNA from endogenous oxidative stress. *Biochimie*, **81**:59–67, 1999.

[23] T. Boothe, L. Hilbert, M. Heide, L. Berninger, W. B. Huttner, V. Zaburdaev, N. L. Vastenhouw, E. W. Myers, D. N. Drechsel, and J. C. Rink. A tunable refractive index matching medium for live imaging cells, tissues and model organisms. *eLife*, **6**:e27 240, 2017.

[24] V. Bormuth, A. Jannasch, M. Ander, C. M. van Kats, A. van Blaaderen, J. Howard, and E. Schäffer. Optical trapping of coated microspheres. *Optics Express*, **16**(18):13 831–13 844, 2008.

[25] N. Bourg, C. Mayet, G. Dupuis, T. Barroca, P. Bon, S. Lecart, E. Fort, and S. Leveque-Fort. Direct optical nanoscopy with axially localized detection. *Nature Photonics*, **9**:587–593, 2015.

[26] R. W. Bowman and M. J. Padgett. Optical trapping and binding. *Reports on Progress in Physics*, **76**:1–28, 2013.

[27] F. Braet and E. Wisse. Structural and functional aspects of liver sinusoidal endothelial cell fenestrae: a review. *Comparative Hepatology*, **1**(1):1, 2002.

[28] C. Cabriel, N. Bourg, G. Dupuis, S. Lecart, E. Fort, and S. Leveque-Fort. Combining axial single molecule localization strategies to enhance 3D imaging of biological samples. In *Focus on Microscopy*. 2017.

[29] L. Carlini, S. J. Holden, K. M. Douglass, and S. Manley. Correction of a depth-dependent lateral distortion in 3D super-resolution imaging. *Plos One*, **10**(11):e0142 949, 2015.

[30] H.-C. Chang and L.-C. Wang. A simple proof of Thue's theorem on circle packing. *arXiv.org*, p. 1009.4322, 2010.

[31] L. Chang, X. Sun, H. Shang, P. Liu, T. J. Hall, and D. Sun. Analysis of the fiber-waveguide coupling efficiency and the resulting polarization dependent loss. In *International Conference on Numerical Simulation of Optoelectronic Devices*. 2017.

[32] B.-C. Chen, W. R. Legant, K. Wang, L. Shao, D. E. Milkie, M. W. Davidson, C. Janetopoulos, X. S. Wu, J. A. Hammer, Z. Liu, B. P. English, Y. Mimori-Kiyosue, D. P. Romero, A. T. Ritter, J. Lippincott-Schwartz, L. Fritz-Laylin, R. D. Mullins, D. M. Mitchell, J. N. Bembenek, A.-C. Reymann, R. Böhme, S. W. Grill, J. T. Wang, G. Seydoux, U. S. Tulu, D. P. Kiehart, and E. Betzig. Lattice light-sheet microscopy: Imaging molecules to embryos at high spatiotemporal resolution. *Science*, **346**(6208):439, 2014.

[33] A. I. Chizhik, J. Rother, I. Gregor, A. Janshoff, and J. Enderlein. Metal-induced energy transfer for live cell nanoscopy. *Nature Photonics*, **8**:124–127, 2014.

[34] A. Chmyrov, J. Keller, T. Grotjohann, M. Ratz, E. d'Este, S. Jakobs, C. Eggeling, and S. W. Hell. Nanoscopy with more than 100,000 'doughnuts'. *Nature Methods*, **10**:737–740, 2013.

[35] R. W. Cole, T. Jinadasa, and C. M. Brown. Measuring and interpreting point spread functions to determine confocal microscope resolution and ensure quality control. *Nature Protocols*, **6**:1929–1941, 2011.

[36] E. Condon. A theory of intensity distribution in band systems. *Physical Review*, **28**(6):1182–1201, 1926.

[37] P. J. Cranfill, B. R. Sell, M. A. Baird, J. R. Allen, Z. Lavagnino, H. M. de Gruiter, G.-J. Kremers, M. W. Davidson, A. Ustione, and D. W. Piston. Quantitative assessment of fluorescent proteins. *Nature Methods*, **13**(7):557–562, 2016.

[38] P. Dedecker, G. C. H. Mo, T. Dertinger, and J. Zhang. Widely accessible method for superresolution fluorescence imaging of living systems. *PNAS*, **109**(27):10 909–10 914, 2012.

[39] G. T. Dempsey, M. Bates, W. E. Kowtoniuk, D. R. Liu, R. Y. Tsien, and X. Zhuang. Photoswitching mechanism of cyanine dyes. *Journal of the American Chemical Society*, **131**(51):18 192–18 193, 2009.

[40] G. T. Dempsey, J. C. Vaughan, K. H. Chen, M. Bates, and X. Zhuang. Evaluation of fluorophores for optimal performance in localization-based super-resolution imaging. *Nature Methods*, **8**(12):1027–1036, 2011.

[41] T. Dertinger, R. Colyer, G. Iyer, S. Weiss, and J. Enderlein. Fast, background-free, 3D super-resolution optical fluctuation imaging (SOFI). *PNAS*, **106**(52):22 287–22 292, 2009.

[42] T. Dertinger, M. Heilemann, R. Vogel, M. Sauer, and S. Weiss. Superresolution optical fluctuation imaging with organic dyes. *Angewandte Chemie International Edition*, **49**(49):9441–9443, 2010.

[43] J. Deschamps, M. Mund, and J. Ries. 3D superresolution microscopy by supercritical angle detection. *Optics Express*, **22**(23):29 081–29 091, 2014.

[44] J. Deschamps, A. Rowald, and J. Ries. Efficient homogeneous illumination and optical sectioning for quantitative single-molecule localization microscopy. *Optics Express*, **24**(24):28 080–28 090, 2016.

[45] H. Deschout, F. Cella Zanacchi, M. Mlodzianoski, A. Diaspro, J. Bewersdorf, S. T. Hess, and K. Braeckmans. Precisely and accurately localizing single emitters in fluorescence microscopy. *Nature Methods*, **11**(3):253–266, 2014.

[46] H. Deschout, T. Lukes, A. Sharipov, D. Szlag, L. Feletti, W. Vandenberg, P. Dedecker, J. Hofkens, M. Leutenegger, T. Lasser, and A. Radenovic. Complementarity of PALM and SOFI for super-resolution live-cell imaging of focal adhesions. *Nature Communications*, **7**:13 693, 2016.

[47] F. M. Dickey and T. E. Lizotte. *Laser Beam Shaping Applications, Second Edition*. CRC Press, 2017.

[48] M. Dienerowitz, G. Gibson, F. Dienerowitz, and M. Padgett. Expanding the toolbox for nanoparticle trapping and spectroscopy with holographic optical tweezers. *Journal of Optics A*, **14**:045 003, 2012.

[49] M. Dienerowitz, M. Mazilu, and K. Dholakia. Optical manipulation of nanoparticles: A review. *Journal of Nanophotonics*, **2**(1):1–32, 2008.

[50] C. J. Dorman. Genome architecture and global gene regulation in bacteria: making progress towards a unified model? *Nature Reviews Microbiology*, **11**:349–355, 2013.

[51] K. M. Douglass, C. Sieben, A. Archetti, A. Lambert, and S. Manley. Super-resolution imaging of multiple cells by optimised flat-field epi-illumination. *Nature Photonics*, **10**(11):705–708, 2016.

[52] F. T. Dullo and O. G. Hellesø. On-chip phase measurement for microparticles trapped on a waveguide. *Lab on a Chip*, **15**(19):3918–3924, 2015.

[53] F. T. Dullo, J.-C. Tinguely, S. A. Solbø, and O. G. Hellesø. Single-mode limit and bending losses for shallow rib Si_3N_4 waveguides. *IEEE Photonics Journal*, **7**(1):2700 511, 2015.

[54] A. R. Dunn, N. M. Kad, S. R. Nelson, D. M. Warshaw, and S. S. Wallace. Single Qdot-labeled glycosylase molecules use a wedge amino acid to probe for lesions while scanning along DNA. *Nucleic Acids Research*, **39**(17):7487–7498, 2011.

[55] J. Enderlein, E. Toprak, and P. R. Selvin. Polarization effect on position accuracy of fluorophore localization. *Optics Express*, **14**(18):8111–8120, 2006.

[56] U. Endesfelder, S. Malkusch, F. Fricke, and M. Heilemann. A simple method to estimate the average localization precision of a single-molecule localization microscopy experiment. *Histochemistry and Cell Biology*, **141**(6):629–638, 2014.

[57] S. W. Englander, D. B. Calhoun, and J. J. Englander. Biochemistry without oxygen. *Analytical Biochemistry*, **161**:300–306, 1987.

[58] D. Engström, M. Persson, J. Bentsson, and M. Goksör. Calibration of spatial light modulators suffering from spatially varying phase response. *Optics Express*, **21**(13):16 086–16 103, 2013.

[59] M. Estevez, M. Alvaret, and L. Lechuga. Integrated optical devices for lab-on-a-chip biosensing applications. *Laser & Photonics Reviews*, **6**(4):463–487, 2012.

[60] A. Farré, M. Shayegan, C. López-Quesada, G. A. Blab, M. Montes-Usategui, N. R. Forde, and E. Martín-Badosa. Position stability of holographic optical traps. *Optics Express*, **19**(22):21 370–21 384, 2011.

[61] K. N. Fish. Total internal reflection fluorescence (TIRF) microscopy. *Current protocols in cytometry*, pp. 12–18, 2009.

[62] E.-L. Florin, A. Pralle, E. H. K. Stelzer, and J. K. H. Hörber. Photonic force microscope calibration by thermal noise analysis. *Applied Physics*, **66**:75–78, 1988.

[63] J. Franck and E. Dymond. Elementary processes of photochemical reactions. *Transactions of the Faraday Society*, **21**:536–542, 1926.

[64] E. C. Friedberg. DNA damage and repair. *Nature*, **421**:436–440, 2003.

[65] C. G. Gailbraith and J. A. Galbraith. Super-resolution microscopy at a glance. *Journal of Cell Science*, **124**(10):1607–1611, 2011.

[66] N. C. Gallagher and B. Liu. Method for computing kinoforms that reduces reconstruction error. *Applied Optics*, **12**:2328–2335, 1973.

[67] D. Gao, W. Ding, M. Nieto-Vesperinas, X. Ding, M. Rahman, T. Zhang, C. Lim, and C.-W. Qiu. Optical manipulation from the microscale to the nanoscale: fundamentals, advances and prospects. *Light: Science & Applications*, **6**, 2017.

[68] S. Geissbuehler, N. L. Bocchio, C. Dellagiacoma, C. Berclaz, M. Leutenegger, and T. Lasser. Mapping molecular statistics with balanced super-resolution optical fluctuation imaging (bSOFI). *Optical Nanoscopy*, **1**(4), 2012.

[69] S. Geissbuehler, A. Sharipov, A. Godinat, N. L. Bocchio, P. A. Sandoz, A. Huss, N. A. Jensen, S. Jakobs, J. Enderlein, F. G. van der Goot, E. A. Dubikovskaya, T. Lasser, and M. Leutenegger. Live-cell multiplane three-dimensional super-resolution optical fluctuation imaging. *Nature Communications*, **5**:5830, 2014.

[70] A. Georgiou. Noise formation in fourier phase-only holograms. *Journal of the Optical Society of America B*, **27**:2677–2686, 2010.

[71] R. W. Gerchberg and W. O. Saxton. A practical algorithm for the determination of phase from image and diffraction plane pictures. *Optik*, **35**(2):237–246, 1972.

[72] R. N. Ghosh and W. W. Webb. Automated detection and tracking of individual and clustered cell surface low density lipoprotein receptor molecules. *Biophysical Journal*, **66**(5):1301–1318, 1994.

[73] G. M. Gibson, R. W. Bowman, A. Linnenberger, M. Dienerowitz, D. B. Phillips, D. M. Carberry, M. J. Miles, and M. J. Padgett. A compact holographic optical tweezers instrument. *Review of Scientific Instruments*, **83**:113 107, 2012.

[74] J. W. Goodman. *Introduction to Fourier Optics*. McGraw-Hill, 1996.

[75] G. Goos and H. Hänchen. Ein neuer und fundamentaler Versuch zur Totalreflexion. *Annalen der Physik*, **7-8**:333–346, 1947.

[76] H. M. Grandin, B. Stadler, M. Textor, and J. Voros. Waveguide excitation fluorescence microscopy: A new tool for sensing and imaging the biointerface. *Biosensors & Bioelectronics*, **21**(8):1476–1482, 2006.

[77] M. Grange, D. Vasishtan, and K. Grünewald. Cellular electron cryo tomography and in situ sub-volume averaging reveal the context of microtubule-based processes. *Journal of Structural Biology*, **197**(2):181–190, 2017.

[78] D. G. Grier. A revolution in optical manipulation. *Nature*, **424**:810–816, 2003.

[79] J. A. Grieve, A. Ulcinas, S. Subramanian, G. M. Gibson, M. J. Padgett, D. M. Carberry, and M. J. Miles. Hands-on with optical tweezers: a multitouch interface for holographic optical trapping. *Optics Express*, **17**(5):3595–3602, 2009.

[80] M. G. L. Gustafsson. Surpassing the lateral resolution limit by a factor of two using structured illumination microscopy. *Journal of Microscopy*, **198**(2):82–87, 2000.

[81] M. G. L. Gustafsson, L. Shao, P. M. Carlton, C. J. R. Wang, I. N. Golubovskaya, W. Z. Cande, D. A. Agard, and J. W. Sedat. Three-dimensional resolution doubling in wide-field fluorescence microscopy by structured illumination. *Biophysical Journal*, **94**(12):4957–4970, 2008.

[82] Hamamatsu. Orca Flash 4.0 Data Sheet.

[83] W. Harm, A. Jesacher, G. Thalhammer, S. Bernet, and M. Ritsch-Marte. How to use a phase-only spatial light modulator as a color display. *Optics Letters*, **40**(4):581–584, 2015.

[84] M. Heilemann, S. van de Linde, A. Mukherjee, and M. Sauer. Super-resolution imaging with small organic fluorophores. *Angewandte Chemie International Edition*, **48**:6903–6908, 2009.

[85] M. Heilemann, S. van de Linde, M. Schüttpelz, R. Kasper, B. Seefeldt, A. Mukherjee, P. Tinnefeld, and M. Sauer. Subdiffraction-resolution fluorescence imaging with conventional fluorescent probes. *Angewandte Chemie International Edition*, **47**(33):6172–6176, 2008.

[86] R. Heintzmann. Estimating missing information by maximum likelihood deconvolution. *Micron*, **38**(2):136–144, 2006.

[87] R. Heintzmann and C. G. Cremer. Laterally modulated excitation microscopy: improvement of resolution by using a diffraction grating. *Proc. SPIE 3568, Optical Biopsies and Microscopic Techniques III*, **3568**:185–196, 1999.

[88] S. W. Hell and J. Wichmann. Breaking the diffraction resolution limit by stimulated emission: stimulated-emission-depletion fluorescence microscopy. *Optics Letters*, **19**(11):780–782, 1994.

[89] Ø. I. Helle, B. S. Ahluwalia, and O. G. Helleso. Optical transport, lifting and trapping of micro-particles by planar waveguides. *Optics Express*, **23**(5):6601–6612, 2015.

[90] Ø. I. Helle, J.-C. Tinguely, M. Lahrberg, R. Heintzmann, and B. S. Ahluwalia. Optical nanoscopy based on photonic integrated circuits. In *Focus on Microscopy*. 2017.

[91] T. Helleday, E. Petermann, C. Lundin, B. Hodgson, and R. A. Sharma. DNA repair pathways as targets for cancer therapy. *Nature Reviews Cancer*, **8**:193–204, 2008.

[92] S. T. Hess, T. P. K. Girirajan, and M. D. Mason. Ultra-high resolution imaging by fluorescence photoactivation localization microscopy. *Biophysical Journal*, **91**(11):4258–4272, 2006.

[93] J. H. J. Hoeijmakers. Genome maintenance mechanisms for preventing cancer. *Nature*, **411**:366–374, 2001.

[94] J. H. J. Hoeijmakers. DNA damage, aging, and cancer. *The New England Journal of Medicine*, **1475-1485**:2009, 2009.

[95] M. Hofmann, C. Eggeling, S. Jakobs, and S. W. Hell. Breaking the diffraction barrier in fluorescence microscopy at low light intensities by using reversibly photoswitchable proteins. *PNAS*, **102**(49):17 565–17 569, 2005.

[96] T. Holm, T. Klein, A. Loschberger, T. Klamp, G. Wiebusch, S. van de Linde, and M. Sauer. A blueprint for cost-efficient localization microscopy. *Chemphyschem*, **15**(4):651–4, 2014.

[97] P. Hoyer, T. Staudt, J. Engelhardt, and S. W. Hell. Quantum dot blueing and blinking enables fluorescence nanoscopy. *Nano Letters*, **11**(1):245–250, 2010.

[98] B. Huang, W. Wang, M. Bates, and X. Zhuang. Three-dimensional super-resolution imaging by stochastic optical reconstruction microscopy. *Science*, **319**(5864):810–813, 2008.

[99] F. Huang, T. M. P. Hartwich, F. E. Rivera-Molina, Y. Lin, W. C. Duim, J. J. Long, P. D. Uchil, J. R. Myers, M. A. Baird, W. Mothes, M. W. Davidson, D. Toomre, and J. Bewersdorf. Video-rate nanoscopy using sCMOS camera-specific single-molecule localization algorithms. *Nature Methods*, **10**(7):653–658, 2013.

[100] F. Huang, S. L. Schwartz, J. M. Byars, and K. A. Lidke. Simultaneous multiple-emitter fitting for single molecule super-resolution imaging. *Biomedical Optics Express*, **2**(5):1377–1393, 2011.

[101] F. Huang, G. Sirinakis, E. S. Allgeyer, L. K. Schroeder, W. C. Duim, E. B. Kromann, T. Phan, F. E. Rivera-Molina, J. R. Myers, I. Irnov, M. Lessard, Y. Zhang, M. A. Handel, C. Jacobs-Wagner, C. P. Lusk, J. E. Rothman, D. Toomre, M. J. Booth, and J. Bewersdorf. Ultra-high resolution 3D imaging of whole cells. *Cell*, **166**:1–13, 2016.

[102] Z. L. Huang, H. Zhu, F. Long, H. Ma, L. Qin, Y. Liu, J. Ding, Z. Zhang, Q. Luo, and S. Zeng. Localization-based super-resolution microscopy with an sCMOS camera. *Optics Express*, **19**(20):19 156–68, 2011.

[103] W. Hübner, G. P. McNerney, P. Chen, B. M. Dale, R. E. Gordon, F. Y. S. Chuang, X.-D. Li, D. M. Asmuth, T. Huser, and B. K. Chen. Quantitative 3D video microscopy of HIV transfer across T cell virological synapses. *Science*, **323**:1743–1747, 2009.

[104] R. G. Hunsperger. *Integrated Optics: Theory and Technology, Third Edition*. Springer, 1991.

[105] J. Icha, M. Weber, J. C. Waters, and C. Norden. Phototoxicity in live fluorescence microscopy, and how to avoid it. *BioEssays*, **39**(18):1700 003, 2017.

[106] IDS. μeye UI-3060CP-M-GL Rev.2 Data Sheet.

[107] S. Inoue. *Handbook of Biological Confocal Microscopy, 3rd edition*, chapter Foundation of Confocal Scanned Imaging in Light Microscopy, p. 1. Springer, 2006.

[108] A. Jablonski. Efficiency of anti-stokes fluorescence in dyes. *Nature*, **131**:839–840, 1933.

[109] A. Jain, R. J. Liu, B. Ramani, E. Arauz, Y. Ishitsuka, K. Ragunathan, J. Park, J. Chen, Y. K. Xiang, and T. Ha. Probing cellular protein complexes using single-molecule pull-down. *Nature*, **473**(7348):484–U322, 2011.

[110] J. Janesick, K. Klaasen, and T. Elliot. CCD charge collection efficiency and the photon transfer technique. *Proceedings of the SPIE 0570*, pp. 7–19, 1985.

[111] K. M. Johnson, W. Li, R. A. Rice, L. A. Pagano-Stauffer, and M. A. Handschy. High-speed binary optical addressed spatial light modulator. *Applied Physics Letters*, **55**(6):537–539, 1989.

[112] M. F. Juette, T. J. Gould, M. D. Lessard, M. J. Mlodzianoski, B. S. Nagpure, B. T. Bennett, S. T. Hess, and J. Bewersdorf. Three-dimensional sub-100 nm resolution fluorescence microscopy of thick samples. *Nature Methods*, **5**:527–529, 2008.

[113] R. Jungmann, C. Steinhauer, M. Scheible, A. Kuzyk, P. Tinnefeld, and F. C. Simmel. Single-molecule kinetics and super-resolution microscopy by fluorescence imaging of transient binding on dna origami. *Nano Letters*, **10**(11):4756–61, 2010.

[114] G. Keiser, F. Xiong, Y. Cui, and P. P. Shum. Review of diverse optical fibers used in biomedical research and clinical practice. *Journal of Biomedical Optics*, **19**(8):080 902, 2014.

[115] S. M. Kelly and M. O'Neill. *Handbook of Advanced Electronic and Photonic Materials and Devices, Volume 7: Liquid Crystals, Display and Laser Materials*, chapter Liquid crystals for electro-optic applications, pp. 1–66. Academic Press, 2000.

[116] M. Kim, C. Park, C. Rodriguez, Y. Park, and Y. H. Cho. Superresolution imaging with optical fluctuation using speckle patterns illumination. *Scientific Reports*, **5**:16 525, 2015.

[117] P. Kner, B. Chun, E. Griffis, L. Winoto, and M. Gustafsson. Super-resolution video microscopy of live cells by structured illumination. *PNAS*, **102**:13 081–13 086, 2009.

[118] K. Kwakwa, A. Savell, T. Davies, I. Munro, S. Parinello, M. A. Purbhoo, C. Dunsby, M. A. Neil, and P. M. W. French. easySTORM: a robust, lower-cost approach to localisation and TIRF microscopy. *Journal of Biophotonics*, **9**:947–957, 2016.

[119] J. R. Lakowicz. *Principles of Fluorescence Spectroscopy*. Springer, 2006.

[120] W. M. Lee, P. J. Reece, R. F. Marchington, N. K. Metzger, and K. Dholakia. Construction and calibration of an optical trap on a fluorescence optical microscope. *Nature Protocols*, **2**(10):3226–3238, 2007.

[121] W. R. Legant, L. Shao, J. B. Grimm, T. A. Brown, D. E. Milkie, B. B. Avants, L. D. Lavis, and E. Betzig. High-density three-dimensional localization microscopy across large volumes. *Nature Methods*, **13**:359–365, 2016.

[122] R. D. Leonardo, F. Ianni, and G. Ruocco. Computer generation of optical holograms for optical trap arrays. *Optics Express*, **15**(4):1913–1922, 2007.

[123] L. B. Lesem, P. M. Hirsch, and J. A. Jordan. The kinoform: A new wavefront reconstruction device. *IBM Journal of Research and Development*, **13**(2):150–155, 1969.

[124] D. Li and E. Betzig. Response to comment on "Extended-resolution structured illumination imaging of endocytic and cytoskeletal dynamics". *Science*, **352**(6285):527, 2016.

[125] L. C. Li, M. T. Li, Z. N. Zhang, and Z. L. Huang. Assessing low-light cameras with photon transfer curve method. *Journal of Innovative Optical Health Sciences*, **9**(3):1630 008, 2016.

[126] R. Lin, A. Clowsley, I. Jayasinghe, D. Baddeley, and C. Soeller. Algorithmic corrections for localization microscopy with sCMOS cameras - characterisation of a computationally efficient localization approach. *Optics Express*, **25**(10):11 701–11 716, 2017.

[127] Y. Lin, J. J. Long, F. Huang, W. C. Duim, S. Kirschbaum, Y. D. Zhang, L. K. Schroeder, A. A. Rebane, M. G. M. Velasco, A. Virrueta, D. W. Moonan, J. Y. Jiao, S. Y. Hernandez, Y. L. Zhang, and J. Bewersdorf. Quantifying and optimizing single-molecule switching nanoscopy at high speeds. *Plos One*, **10**(5):e0128 135, 2015.

[128] S. Liu, M. J. Mlodzianoski, Z. Hu, Y. Ren, K. McElmurry, D. M. Suter, and F. Huang. sCMOS noise-correction algorithm for microscopy images. *Nature Methods*, **14**:760–761, 2017.

[129] F. Long, S. Zeng, and Z. L. Huang. Localization-based super-resolution mi-

croscopy with an sCMOS camera part II: experimental methodology for comparing sCMOS with EMCCD cameras. *Optics Express*, **20**(16):17 741–17 759, 2012.

[130] L. Lucy. An iterative technique for the rectification of observed distributions. *Astronomical Journal*, **79**:745, 1974.

[131] H. Ma, R. Fu, J. Xu, and Y. Liu. A simple and cost-effective setup for super-resolution localization microscopy. *Scientific reports*, **7**:1542, 2017.

[132] M. L. Martin-Fernandez, C. Tynan, and S. Webb. A 'pocket guide' to total internal reflection fluorescence. *Journal of Microscopy*, **252**(1):16–22, 2013.

[133] A. L. Mattheyses and D. Axelrod. Direct measurement of the evanescent field profile produced by objective-based total internal reflection fluorescence. *Journal of Biomedical Optics*, **11**(1):014 006–014 007, 2006.

[134] S. A. McKinney, C. S. Murphy, K. L. Hazelwood, M. W. Davidson, and L. L. Looger. A bright and photostable photoconvertible fluorescent protein for fusion tags. *Nature Methods*, **6**(2):131–133, 2009.

[135] G. P. McNerney, W. Hübner, B. K. Chen, and T. Huser. Manipulating CD4+ T cells by optical tweezers for the initiation of cell-cell transfer of HIV-1. *Journal of Biophotonics*, **3**(4):216–223, 2010.

[136] M. J. Mlodzianoski, J. M. Schreiner, S. P. Callahan, K. Smolkova, A. Dlaskova, J. Santorova, P. Jezek, and J. Bewersdorf. Sample drift correction in 3D fluorescence photoactivation localization microscopy. *Optics Express*, **19**(16):15 009–15 019, 2011.

[137] V. Mönkemöller, C. Oie, W. Hübner, T. Huser, and P. McCourt. Multimodal super-resolution optical microscopy visualizes the close connection between membrane and the cytoskeleton in liver sinusoidal endothelial cell fenestrations. *Scientific Reports*, **5**, 2015.

[138] K. I. Mortensen, L. S. Churchman, J. A. Spudich, and H. Flyvbjerg. Optimized localization analysis for single-molecule tracking and super-resolution microscopy. *Nature Methods*, **7**(5):377–381, 2010.

[139] L. Nahidiazar, A. V. Agronskaia, J. Broertjes, B. van den Broek, and K. Jalink. Optimizing imaging conditions for demanding multi-color super resolution localization microscopy. *Plos One*, **11(7)**:e0158 884, 2016.

[140] H. Naumann, G. Schröder, and M. Löffler-Mang. *Handbuch Baulelemente Optik, 7th Edition*. Hanser, 2014.

[141] K. Neuman, E. Chadd, G. Liou, K. Bergman, and S. Block. Characterization

of photodamage to Escherichia coli in optical traps. *Biophysical Journal*, **77**:2856–2863, 1999.

[142] K. C. Neuman and S. M. Block. Optical trapping. *Review of Scientific Instruments*, **75**(9):2787–2809, 2004.

[143] R. P. Nieuwenhuizen, K. A. Lidke, M. Bates, D. L. Puig, D. Grunwald, S. Stallinga, and B. Rieger. Measuring image resolution in optical nanoscopy. *Nature Methods*, **10**(6):557–562, 2013.

[144] R. P. J. Nieuwenhuizen, S. Stallinga, and B. Rieger. *Cell Membrane Nanodomains – From Biochemistry to Nanoscopy*, chapter Visualization and Resolution in Localization Microscopy, pp. 409–430. CRC Press, 2014.

[145] H. Nyquist. Certain topics in telegraph transmission theory. *Transaction of the AIEE*, **47**:617–644, 1928.

[146] R. J. Ober, S. Ram, and E. S. Ward. Localization accuracy in single-molecule microscopy. *Biophysical Journal*, **86**(2):1185–1200, 2004.

[147] N. Olivier, D. Keller, P. Gonczy, and S. Manley. Resolution doubling in 3D-storm imaging through improved buffers. *Plos One*, **8**(7):e69 004, 2013.

[148] N. Olivier, D. Keller, V. S. Rajan, P. Gonczy, and S. Manley. Simple buffers for 3D storm microscopy. *Biomedical Optics Express*, **4**(6):885–899, 2013.

[149] M. Ovesny, P. Krizek, J. Borkovec, Z. Svindrych, and G. M. Hagen. ThunderSTORM: a comprehensive ImageJ plug-in for PALM and STORM data analysis and super-resolution imaging. *Bioinformatics*, **30**(16):2389–2390, 2014.

[150] S. R. P. Pavani, M. A. Thompson, J. S. Biteen, S. J. Lor, N. Liu, R. J. Twieg, R. Piestun, and W. E. Moerner. Three-dimensional, single-molecule fluorescence imaging beyond the diffraction limit by using a double-helix point spread function. *PNAS*, **106**:2995–2999, 2009.

[151] J. Pelletier, K. Halvorsen, B.-Y. Ha, R. Paparcone, S. J. Sandler, C. L. Woldringh, W. P. Wong, and S. Jun. Physical manipulation of the Escherichia coli chromosome reveals its soft nature. *PNAS*, **109**:2649–2656, 2012.

[152] M. Persson. *Advances in Holographic Optical Trapping*. Ph.D. thesis, University of Gothenburg, 2013.

[153] M. Persson, D. Engström, A. Frank, J. Backsten, J. Bengtsson, and M. Goksör. Minimizing intensity fluctuations in dynamic holographic optical tweezers by restricted phase change. *Optics Express*, **18**(11):11 250–11 263, 2010.

[154] M. Persson, D. Engström, and M. Goksör. An algorithm for improved control of trap intensities in holographic optical tweezers. *Proceedings of the SPIE*, **84582**:1–7, 2012.

[155] M. Persson, D. Engström, and M. Goksör. Reducing the effect of pixel crosstalk in phase only spatial light modulators. *Optics Express*, **20**(20):22 334–22 343, 2012.

[156] A. Picco, M. Mund, J. Ries, F. Nedelec, and M. Kaksonen. Visualizing the functional architecture of the endocytic machinery. *eLife*, **4**:04 535, 2015.

[157] R. M. Power and J. Huisken. A guide to light-sheet fluorescence microscopy for multiscale imaging. *Nature Methods*, **14**:360–373, 2017.

[158] F. Prieto, B. Sepulveda, A. Calle, A. Llobera, C. Dominguez, A. Abad, A. Montoya, and L. M. Lechuga. An integrated optical interferometric nanodevice based on silicon technology for biosensor applications. *Nanotechnology*, **14**(8):907–912, 2003.

[159] T. Quan, S. Zeng, and Z. L. Huang. Localization capability and limitation of electron-multiplying charge-coupled, scientific complementary metal-oxide semiconductor, and charge-coupled devices for superresolution imaging. *Journal of Biomedical Optics*, **15**(6):066 005, 2010. 5017.

[160] J. Radicella, C. Dherin, C. Desmze, M. Fox, and S. Boiteux. Cloning and characterization of hOGG1, a human homolog of the OGG1 gene of Saccharomyces cerevisiae. *PNAS*, **94**:8010–8015, 1997.

[161] S. Ramachandran, D. A. Cohen, A. P. Quist, and R. Lal. High performance, LED powered, waveguide based total internal reflection microscopy. *Scientific Reports*, **3**:2133, 2013.

[162] E. H. Rego, L. Shao, J. J. Macklin, L. Winoto, G. A. Johansson, N. Kamps-Hughes, M. W. Davidson, and M. G. L. Gustafsson. Nonlinear structured-illumination microscopy with a photoswitchable protein reveals cellular structures at 50-nm resolution. *PNAS*, **109**(3):135–143, 2011.

[163] R. Reichelt. *Science of Microscopy*, chapter Scanning Electron Microscopy, pp. 133–272. Springer, 2007.

[164] W. H. Richardson. Bayesian-based iterative method of image restoration. *Journal of the Optical Society of America*, **62**(1):55–59, 1972.

[165] J. Ries, V. Udayar, A. Soragni, S. Hornemann, K. P. R. Nilsson, R. Riek, C. Hock, H. Ewers, A. A. Aguzzi, and L. Rajendran. Superresolution imaging of amyloid fibrils with binding-activated probes. *ACS Chemical Neuroscience*,

4:1057–1061, 2013.

[166] M. S. Robbins. *Single-Photon Imaging*, chapter Electron-Multiplying Charge Coupled Devices – EMCCDs, pp. 103–121. Springer, 2011.

[167] P. W. K. Rothemund. Folding DNA to create nanoscale shapes and patterns. *Nature*, **440**:297–302, 2006.

[168] M. J. Rust, M. Bates, and X. Zhuang. Sub-diffraction-limit imaging by stochastic optical reconstruction microscopy (STORM). *Nature Methods*, **3**:793–795, 2006.

[169] B. Ruszczyncki and T. Bernas. Quality of biological images, reconstructed using localization microscopy data. *Bioinformatics*, 2007.

[170] D. Sage, H. Kirshner, T. Pengo, N. Stuurman, J. Min, S. Manley, and M. Unser. Quantitative evaluation of software packages for single-molecule localization microscopy. *Nature Methods*, **12**(8):717–724, 2015.

[171] S. J. Sahl, S. W. Hell, and S. Jakobs. Fluorescence nanoscopy in cell biology. *Nature Reviews Molecular Cell Biology*, 2017.

[172] P. Sarder and A. Nehorai. Deconvolution methods for 3-D fluorescence microscopy images. *IEEE Signal Processing Magazine*, pp. 32–45, 2006.

[173] M. Sauer, J. Hofkens, and J. Enderlein. *Handbook of Fluorescence Spectroscopy and Imaging*. Wiley-VCH, 2011.

[174] S. Saurabh, S. Maji, and M. P. Bruchez. Evaluation of sCMOS cameras for detection and localization of single Cy5 molecules. *Optics Express*, **20**(7):7338–7349, 2012.

[175] W. Saxton and W. Baumeister. The correlation averaging of a regularly arranged bacterial cell envelope protein. *Journal of Microscopy*, **127**(2):127–138, 1982.

[176] L. Schermelleh, R. Heintzmann, and H. Leonhardt. A guide to super-resolution fluorescence microscopy. *Journal of Cell Biology*, **190**(2):165–175, 2010.

[177] J. Schindelin, I. Arganda-Carreras, E. Frise, V. Kaynig, M. Longair, T. Pietzsch, S. Preibisch, C. Rueden, S. Saalfeld, and B. Schmid. Fiji: an open-source platform for biological-image analysis. *Nature Methods*, **9**(7):676–682, 2012.

[178] J. Schnitzbauer, M. T. Strauss, T. Schlichthaerle, F. Schueder, and R. Jungmann. Super-resolution microscopy with DNA-PAINT. *Nature Protocols*, **12**(6):1198–1228, 2017.

[179] I. Schoen, J. Ries, E. Klotzsch, H. Ewers, and V. Vogel. Binding-activated localization microscopy of DNA structures. *Nano Letters*, **11**:4008–4011, 2011.

[180] C. E. Shannon. Communication in the presence of noise. *Proceedings of the IEEE*, **86**(2):447–457, 1998. Reprint.

[181] L. Shao, P. Kner, E. H. Rego, and M. L. Gustafsson. Super-resolution 3D microscopy of live whole cells using structured illumination. *Nature Methods*, **8**:1044–1046, 2011.

[182] A. Sharonov and R. M. Hochstrasser. Wide-field subdiffraction imaging by accumulated binding of diffusing probes. *PNAS*, **103**(50):18 911–18 916, 2006.

[183] P. J. Shaw. *Handbook of Biological Confocal Microscopy, 3rd edition*, chapter Comparison of Widefield/Deconvolution and Confocal Microscopy for Three-Dimensional Imaging, pp. 453–467. Springer, 2006.

[184] H. Shen, E. Huang, T. Das, H. Xu, M. Ellisman, and Z. Liu. TIRF microscopy with ultra-short penetration depth. *Optics Express*, **22**(9):10 728–10 734, 2014.

[185] H. Shroff, C. G. Galbraith, J. A. Galbraith, and E. Betzig. Live-cell photoactivated localization microscopy of nanoscale adhesion dynamics. *Nature Methods*, **5**(5):417–423, 2008.

[186] J.-B. Sibarita. Deconvolution microscopy. *Advances in Biochemical Engineering/Biotechnology*, **95**:201–243, 2005.

[187] J. G. Silva, N. P. Martins, R. Henriques, and H. Soares. HIV-1 Nef impairs the formation of calcium membrane territories controlling the signaling nanoarchitecture at the immunological synapse. *Journal of Immunology*, **197**(10):4042–4052, 2016.

[188] T. Silverstein, B. Gibb, and E. Greene. Visualizing protein movement on DNA at the single-molecule level using DNA curtains. *DNA Repair*, **20**:94–109, 2014.

[189] B. Smedsrod and H. Pertoft. Preparation of pure hepatocytes and reticuloendothelial cells in high yield from a single rat liver by means of Percoll centrifugation and selective adherence. *Journal of Leukocyte Biology*, **38**(2):213–230, 1985.

[190] C. S. Smith, N. Joseph, B. Rieger, and K. A. Lidke. Fast, single-molecule localization that achieves theoretically minimum uncertainty. *Nature Methods*, **7**(5):373–375, 2010.

[191] X. Song and R. Leonhardt. Ray optics analysis of single-mode condition for optical waveguides with rectangular cross-section. *Progress In Electromagnetics Research*, **135**:81–89, 2013.

[192] C. Spahn, U. Endesfelder, and M. Heilemann. Super-resolution imaging of Escherichia coli nucleoids reveals highly structured and asymmetric segregation during fast growth. *Journal of Structural Biology*, **185**:243–249, 2014.

[193] C. Sparrow. On spectroscopic resolving power. *Astrophysical Journal*, **44**:76–86, 1916.

[194] D. R. Stabley, T. Oh, S. M. Simon, A. L. Mattheyses, and K. Salaita. Real-time fluorescence imaging with 20 nm axial resolution. *Nature Communications*, **6**:9307, 2015.

[195] D. J. Stephens and V. J. Allan. Light microscopy techniques for live cell imaging. *Science*, **300**(82):82–86, 2003.

[196] H. Takakura, Y. Zhang, R. S. Erdmann, A. D. Thompson, Y. Lin, B. McNellis, F. Rivera-Molina, S. N. Uno, M. Kamiya, Y. Urano, J. E. Rothman, J. Bewersdorf, A. Schepartz, and D. Toomre. Long time-lapse nanoscopy with spontaneously blinking membrane probes. *Nature Biotechnology*, **35**:773–780, 2017.

[197] H. F. Taylor and A. Yariv. Guided wave optics. *Proceedings of the IEEE*, **62**(8):1044–1060, 1974.

[198] G. Thalhammer, R. W. Bowman, G. D. Love, M. J. Padgett, and M. Ritsch-Marte. Speeding up liquid crystal slms using overdrive with phase change reduction. *Optics Express*, **21**(2):1779–1797, 2013.

[199] ThermoFisher. www.thermofisher.com/order/catalog/product/S21374, Download: 2017-10-25.

[200] R. E. Thompson, D. R. Larson, and W. W. Webb. Precise nanometer localization analysis for individual fluorescent probes. *Biophysical Journal*, **82**(5):2775–2783, 2002.

[201] M. Tokunaga, N. Imamoto, and K. Sakata-Sogawa. Highly inclined thin illumination enables clear single-molecule imaging in cells. *Nature Methods*, **5**(2):159–161, 2008.

[202] G. Tortarolo, M. Castello, C. J. R. Sheppard, S. Koho, A. Diaspro, and G. Vicidomini. Fourier ring correlation as a tool to assess effective resolution in point scanning microscopy. In *Focus on Microscopy*. 2017.

[203] S. van de Linde, I. Krstic, T. Prisner, S. Doose, M. Heilemann, and M. Sauer.

Photoinduced formation of reversible dye radicals and their impact on super-resolution imaging. *Photochemical & Photobiological Sciences*, **10**(4):499–506, 2011.

[204] S. van de Linde, A. Löschberger, T. Klein, M. Heidbreder, S. Wolter, M. Heilemann, and M. Sauer. Direct stochastic optical reconstruction microscopy with standard fluorescent probes. *Nature Protocols*, **6**(7):991–1009, 2011.

[205] S. van de Linde, S. Wolter, M. Heilemann, and M. Sauer. The effect of photoswitching kinetics and labeling densities on super-resolution fluorescence imaging. *Journal of Biotechnology*, **149**(4):260–266, 2010.

[206] J. Vaughan, S. Jia, and X. Zhuang. Ultra-bright photoactivatable fluorophores created by reductive caging. *Nature Methods*, **9**(12):1181–1184, 2012.

[207] C. Ventalon and J. Mertz. Quasi-confocal fluorescence sectioning with dynamic speckle illumination. *Optics Letters*, **30**(24):3350–3352, 2005.

[208] B. Villalobos-Mendoza, F. S. Granados-Agustin, D. Aguirre-Aguirre, and A. Cornejo-Rodríguez. Liquid crystal display for phase shifting. In *Proceedings of the SPIE Vol. 8785*. 2013.

[209] J. Vogelsang, R. Kasper, C. Steinhauer, B. Person, M. Heilemann, M. Sauer, and P. Tinnefeld. A reducing and oxidizing system minimizes photobleaching and blinking of fluorescent dyes. *Angewandte Chemie International Edition*, **47**:5465–5469, 2008.

[210] J. Vogelsang, C. Steinhauer, C. Forthmann, I. H. Stein, B. Person-Skegro, T. Cordes, and P. Tinnefeld. Make them blink: Probes for super-resolution microscopy. *ChemPhysChem*, **11**:2475–2490, 2010.

[211] C. Vonesch, R. Terres Cristofani, and G. Schmit. Deconvolutionlab. http://bigwww.epfl.ch/algorithms/deconvolution, 2007.

[212] S. Wäldchen, J. Lehmann, T. Klein, S. van de Linde, and M. Sauer. Light-induced cell damage in live-cell super-resolution microscopy. *Scientific Reports*, **5**:15 348, 2015.

[213] X. Wang, S. Chen, M. Kong, Z. Wang, K. D. Costa, R. A. Li, and D. Sun. Enhanced cell sorting and manipulation with combined optical tweezer and microfluidic chip technologies. *Lab on a Chip*, **11**(21):3656–3662, 2011.

[214] K. Weber, P. C. Rathke, and M. Osborn. Cytoplasmic microtubular images in glutaraldehyde-fixed tissue culture cells by electron microscopy and by

immunofluorescence microscopy. *PNAS*, **75**(4):1820–1824, 1978.

[215] N. Wiener. *Extrapolation, Interpolation, and Smoothing of Stationary Time Series*. Wiley, 1949.

[216] K. I. Willig, S. O. Rizzoli, V. Westphal, R. Jahn, and S. W. Hell. Sted microscopy reveals that synaptotagmin remains clustered after synaptic vesicle exocytosis. *Nature*, **440**:935–939, 2006.

[217] C. M. Winterflood and H. Ewers. Single-molecule localization microscopy using mCherry. *ChemPhysChem*, **15**(16):3447–3451, 2014.

[218] D. L. Wolfson, M. Steck, M. Persson, G. McNerney, A. Popovich, M. Goksör, and T. Huser. Rapid 3D fluorescence imaging of individual optically trapped living immune cells. *Journal of Biophotonics*, **8**(3):208–2016, 2015.

[219] S. Wolter, A. Löschberger, T. Holm, S. Aufmkolk, M.-C. Dabauvalle, S. van de Linde, and M. Sauer. rapidSTORM: accurate, fast open-source software for localization microscopy. *Nature Methods*, **9**(11):1040–1041, 2012.

[220] S. Wolter, M. Schüttpelz, M. Tscherepanow, S. van de Linde, M. Heilemann, and M. Sauer. Real-time computation of subdiffraction-resolution fluorescence images. *Journal of Microscopy*, **237**:12–22, 2009.

[221] M. Wördemann. *Structured Light Fields*. Springer, 2012.

[222] I. Yahiatene, S. Hennig, M. Müller, and T. Huser. Entropy-based super-resolution imaging (ESI): From disorder to fine detail. *ACS Photonics*, **2**(8):1049–1056, 2015.

[223] M. Yang, H. Chen, K. J. Webb, S. Minin, S. L. Chuang, and G. R. Cueva. Demonstration of mode conversion in an irregular waveguide. *Optics Letters*, **31**(3):383–385, 2006.

[224] P. Yeh and C. Gu. *Optics of Liquid Crystal Displays*. Wiley, 2009.

[225] W. S. Zaoui, A. Kunze, W. Vogel, M. Berroth, J. Butschke, F. Letzkus, and J. Burghartz. Bridging the gap between optical fibers and silicon photonic integrated circuits. *Optics Express*, **22**(2):1277–1286, 2014.

[226] Z. Zhang, S. J. Kenny, M. Hauser, W. Li, and K. Xu. Ultrahigh-throughput single-molecule spectroscopy and spectrally resolved super-resolution microscopy. *Nature Methods*, **12**:935–938, 2015.

[227] Z. Zhang, Z. You, and D. Chu. Fundamentals of phase-only liquid crystal on silicon (LCOS) devices. *Light: Science & Applications*, **3**:e213, 2014.

[228] Z. Zhao, B. Xin, L. Li, and Z. Huang. High-power homogeneous illumination for super-resolution localization microscopy with large field-of-view. *Optics*

Express, **25**(12):13 382–13 395, 2017.

[229] Q. Zheng, M. F. Juette, S. Jockusch, M. R. Wasserman, Z. Zhou, R. B. Altman, and S. C. Blanchard. Ultra-stable organic fluorophores for single-molecule research. *Chemical Society Reviews*, **43**:1044–1056, 2014.

[230] L. Zhu, W. Zhang, D. Elnatan, and B. Huang. Faster STORM using compressed sensing. *Nature Methods*, **9**(7):721–723, 2012.

A. Materials and Methods

A.1. Optical setups

A.1.1. Waveguide imaging

Most waveguide-related experiments were conducted together with Øystein Helle.

Optomechanics

Waveguide-based imaging was performed on an upright microscope based on a modular, commercially available series (BXFM, Olympus), retrofitted with a waveguide chip module consisting of a piezo stage (17MAX604, Melles Griot or MDT-630B/M, Thorlabs) holding an objective lens (LMPlanFI 50×/0.5 BD, or LMPlanFI 50×/0.5 Olympus) or a lensed fiber (HP460sm, WT & T) used for coupling into the waveguide. The piezo allows fine tuning of the coupling, and was also programed through a piezo controller (BPC303, Thorlabs) or controlled by a signal generator to oscillate during image acquisition. The chip was held by a vacuum chuck on a translation stage (MBT402D, Thorlabs) to prevent movement during coupling. During *d*STORM image acquisition, the vacuum pump was turned off to minimize sample drift but suction was retained.

Imaging path

Imaging was performed using a 20×/ NA 0.4 (Plan N 20×/0.4, Olympus), 20×/ NA 0.45 (LUCPlanFL N 20×/0.45, Olympus), a 60×/ NA 1.2 water immersion (UplanSApo 60×/ 1.2 w, Olympus), or a 60×/ NA 1.42 oil immersion (PlanApo N 60×/1.42 oil, Olympus) objective lens optionally held by a z-piezo stage. Different emission filter sets of both LP and BP filters were used, and the signal was captured by a sCMOS camera (Orca Flash 4 or Orca Flash 4 v2, Hamatsu), controlled by Micro Manager 1.4 or the manufacturer software (Hamamatsu HCImage). The backprojected pixel width and height was 75.9 nm or 228.3 nm for pamCherry,

MitoTracker Deep Red, Alexa 488, Atto 488, and CellMask Deep Red measurements, and 108.33 nm, 121.9 nm, or 325 nm for Alexa 647 measurements.

Illumination path

Illumination was provided to the chip either via coupling a laser (660 nm, Cobolt) into the lensed fiber or by combining several laser lines through the coupling objective lens or by an Argon-Krypton-Ion laser (Innova 70C, Coherent).

The combined illumination unit consisted of four solid state lasers (405 nm, Oxxius, 488 nm, Oxxius, 561 nm, Cobolt and 660 nm, Cobolt). Each beam profile width was adjusted by an individual Keplarian telescope and spatial overlay was achieved by dichroic mirrors.

From the multiple laser lines emitted by the Argon-Krypton-Ion laer, the 488 nm and 647 nm vaccum wavelengths were selected by an acousto-optic tunable filter (AOTFnC-VIS-TN 1001, AA Opto Electronic) and additionally filtered by a bandpass filter (FF01-390/482/563/640-25, Semrock).

The diffuser was built by removing the blades from a computer fan and glueing an opaque foil to it. The motor was then connected to a 12 V source. This diffuser was placed close to the shared focal plane of a 4f-telescope built from $f = 50$ mm (AC254-050-A-ML, Thorlabs) and a $f = 40$ mm (AC254-040-A-ML, Thorlabs) lenses.

Waveguide chips

Waveguide chips were provided by Balpreet Singh Ahluwalia and co-workers. Details about the fabrication process are described in [6, 158]. Before attaching samples to the waveguides, the chips were cleaned by submerging the chip in 5% (v/v) Hellmanex (Sigma Aldrich) for 10 minutes at 70 °C. Hellmanex was removed using distilled H_2O (dH_2O), and another cleaning step using isopropanol (Sigma Aldrich) was performed before rinsing once more with dH2O.

A.1.2. Widefield TIRF and HILO imaging

The same widefield micrsocope was used for the comparison of conventional objective-based TIRF *d*STORM to waveguide-based *d*STORM imaging and for the combination of holographic optical trapping with *d*STORM.

Illumination path

The setup is built around an inverted microscope (IX-71, Olympus) that uses oil-immersion objective lenses (PlanApo, 60×/ NA 1.45 or Apo N, and 60×/ NA 1.49, Olympus). For fluorescence excitation, 488 nm and 647 nm laser light emitted by an Argon-Krypton-Ion laser (Innova 70C, Coherent) was selected by an acousto-optic tunable filter (AOTFnC-VIS-TN 1001, AA Opto Electronic) and additionally filtered by a bandpass filter (FF01-390/482/563/640-25, Semrock). Using two lenses ($f = 25\,\text{mm}$ and $f = 120\,\text{mm}$ nominal focal lengths) the beam was focused onto the back focal plane of the microscope objective lens. Behind the second lens, a mirror (BB02-E02, Thorlabs) is mounted on a linear translation stage to adjust the position of the beam entering the objective lens.

Imaging path

Fluorescence emission and white light images were magnified by a telescope and projected onto an EMCCD camera (iXon DV887DCS-BV, Andor) with backprojected pixel widths and heights of 105 nm, 116 nm or 121 nm. For the selective suppression of excitation light and blocking of back-scattered light from the optical traps, three filters (LP02-647RU-25, Semrock, ET700/75m, Chroma, and FF01-775/SP-25, Semrock) were directly mounted to the camera.

A.1.3. Holographic optical tweezers

The setup for the holographic optical tweezers was built around the widefield setup using the inverted IX-71 microscope. The setup was partially built together with Deanna L. Wolfson. The modifications for DNA-repair protein tracking as well as the according experiments were performed together with Arash Ahmadi.

For the generation of holographic optical tweezers a 2 W diode-pumped all-solid-state IR laser (MIL-H-1064, CNI) emitting light at a wavelength of 1064 nm was used. The beam was expanded using a telescope (AC 254-030-B-ML, AC 254-100-B-ML, Thorlabs) before it was coupled through an objective lens (DIN 10, 10X, NA 0.25, Edmund) into a polarization-maintaining, high power optical fiber (PMJ-A3HPM, 3S-1060-6/125-3AS-3, OZ Optics). The global IR laser power was controlled with an adjustable ND-filter wheel. Using either a lens (AC 508-200-B-ML, Thorlabs) in combination with an adjustable aperture for spatial filtering or a collimator (F810SMA-1064, Thorlabs) the IR beam was expanded to overfill the active area of a SLM (XY Series 512x512, Boulder Nonlinear Systems). A 4f-

telescope consisting of two lenses (50 mm diameter, AC508-300-B-ML, Thorlabs) imaged the SLM onto the back focal plane (BFP) of the microscope objective lens (PlanApo, 60X, NA 1.45, Olympus). The laser tweezers light path was overlaid with the fluorescence excitation light path using a dichroic mirror (NFD01-1064-25x36, Semrock). To spectraly filter the excitation and trapping light from the fluorescence emission a second dichroic mirror (FF502/670-Di01-25x36x3.0, Semrock) was used. A folding mirror inside the microscope body allowed the imaging path to be guided through a short-pass filter (E700SP-2P, Chroma) to a CMOS camera (UI-1240SE-NIR-GL CMOS, IDS), which was used for alignment, SLM characterization, and video feedback for the software controlling the optical trap pattern, but not for super-resolution image acquisition. The camera and the SLM were connected to a computer (Intel i5-2400 3.1 GHz CPU, 4 GB RAM, Windows 7, 32-bit OS) equipped with a GPU (GeForce GTX 550Ti, Nvidia) for real-time computation of the phase pattern applied to the SLM. LabVIEW-based (LabVIEW 2010 SP1, National Instruments) software programmed by Martin Persson was used to control the trapping experiment and to compute the phase pattern corresponding to the traps' positions either by a lens-and-prism-phase or Gerchberg-Saxton-based algorithm [153].

A.1.4. (s)CMOS Camera characterization and comparison

Camera control

The CMOS μeye device adapter for Micro Manager was modified by Marcel Müller to allow for high acquisition speeds.

The CMOS μeye cameras (UI-3060CP-M-GL Rev.2, IDS) were connected via USB 3.0 to Windows 7 PCs (PC hardware for *d*STORM measurements: Dell Latitude E5540, Intel i3-4030U CPU, 8GB memory, 64 bit OS) and run using Micro Manager version 1.4. The sCMOS (Hamamatsu Orca Flash 4) camera was run using Micro Manager version 1.4 on a Windows 7 Desktop PC (Intel Xeon CPU W3680, 24 GB memory, 64 bit OS) with the default device adapter included with MicroManager.

Illumination path

A 40 mW laser with 639 nm vacuum wavelength (Coherent) for fluorescence excitation was optionally expanded by a telescope ($f = -30$ mm and $f = 160$ mm, Qioptiq). The beam was filtered through an excitation filter (639DF9, Omega

Optics) before focusing by a $f = 200\,\text{mm}$ lens (Qioptiq) to the back focal plane of the TIRF objective lens (60× NA 1.49 ApoN, Olympus). Before transmission through the focusing lens, the fluorescence excitation beam was combined with the beam from a 50 mW laser with 405 nm vacuum wavelength (OBIS, Coherent) for photoswitching. Mounting on a translation stage allowed for shifting the beam position at the back-focal-plane of the objective lens to switch from epi to TIRF illumination.

Imaging path

A dichroic mirror (F63-T01, AHF) was used for spectral separation between excitation and emission. The fluorescence emission was additionally filtered (Razor Edge Long Pass 647, Semrock, and HQ 685/70, Chroma) and focused onto the camera chips. In case of the CMOS camera, we used a tube lens of $f = 160\,\text{mm}$ nominal focal length (Qioptiq), resulting in measured backprojected pixel widths and heights of 109.7 nm. For direct comparison measurements to the sCMOS camera, the fluorescence emission beam was split by a 50/50 beamsplitter cube (G335520000, Qioptiq) to both cameras. In case of the sCMOS camera, we used a tube lens with $f = 180\,\text{mm}$ (Qioptiq) to achieve comparable values for the backprojected pixel widths and heights which we measured as 107.5 nm. The tube lenses were aligned by placing the $f = 160\,\text{mm}$ lens such that spherical aberrations were minimized in the signal for the CMOS camera. Afterward, the $f = 180\,\text{mm}$ lens was positioned such that both cameras shared the same focal plane on the sample.

A.1.5. Cost-efficient multi-color imaging

Illumination path

A fiber-coupled laser with a vacuum wavelength of 647 nm (Coherent) was collimated and combined with the beam emitted from a laser of 488 nm vacuum wavelength (Coherent) using a dichroic mirror (FF-499-Di01-25x36, Semrock). The lasers were filtered by clean-up filters (LL01-647-12.5, Semrock and LL01-488-12.5, Semrock). The beam diameter was adjusted using a 4f-telescope of two focusing lenses (Thorlabs) before being focused by a $f = 200\,\text{mm}$ lens (G063205000, Qioptiq) onto the back-focal-plane of 60×/ NA 1.49 TIRF objective lens (60× NA 1.49 ApoN, Olympus). The illumination unit was mounted on a translatable stage (PT1B/M, Thorlabs) to allow for switching from epi to HILO and TIRF illumination. The microscope stage (KT 90-D56-MP, OWIS) was mounted to a dynamically

damped post (DP14A/M). The entire setup was built on a solid aluminum breadboard (MB6090/M, Thorlabs) that rested on a bicycle inner tubing on a granite table.

Detection path

Fluorescence emission was separated from the excitation via a dichroic beamsplitter (Di03-R405/488/532/635-t11-25x36, Semrock) and separated by wavelength via a further dichroic beamsplitter (FF640-FDi01-25x36, Semrock) before being focused by two separate tube lenses of $f = 160\,\mathrm{mm}$ (G063204000, Qioptiq) onto the CMOS cameras (UI-3060CP-M-GL Rev.2, IDS). The fluoresence excitation was additionally filtered in the deep-red channel (BLP01-647R-25, Semrock and F47-700, AHF) and in the green channel (FF03-525/50-25, Semrock and FF01-550/88-25, Semrock).

A.2. Sample preparation

A.2.1. Waveguide imaging

PDMS chambers

To serve as a vessel for the sample and the imaging buffer as well as to prevent light from coupling into the coverslip, custom made Polydimethylsiloxane (PDMS) (Sylgard) chambers of 120 µm height were mounted on top of the chips to lift the coverglass (# 1.5) (Thermo Fisher Scientific Gerhard Menzel). It was verified that only light guided by the waveguide excites fluorescence.

The chambers were prepared by mixing PDMS and the curing agent at a ratio of 10:1. In a standard plastic petry dish, 1.7 g of this solution were placed in the center. The dish was spun for about 20 s at 900 rpm, accelerated at 70 rpm/s. The layers were cured for more than 2 h at 50 °C. Chambers were cut ad libitum from the PDMS layers.

LSECs

Samples of rat sinusoidal endothelial liver cells shown in Figures 3.5a-d, 3.8, 3.9d, 3.10, 3.12, 3.14d,e, 3.16 were isolated, seeded onto the waveguides, fixed, and stained by Cristina I. Øie. The LSECs were isolated and purified as described

in [189]. Cleaned waveguide chips were coated with human fibronectin (50 µg/ml) for 10 min at room temperature. Isolated LSECs in RPMI 1640 were seeded on the fibronectin coated waveguide chips and incubated for 1 h at 37 °C, followed by a washing step to remove non-attached cells and debris and allowed to spread their cytoplasm for another 2 h. The cells were then washed with phosphate buffered saline (PBS) and fixed with 4% paraformaldehyde (PFA) in PBS and 0.02 M sucrose, pH 7.2 for 30 minutes. Following fixation, the cell membranes were permeabilized with 0.1% Triton X in PBS for 10 min at RT. Actin was stained with Atto 488-phalloidin (Sigma Aldrich), 1:400 dilution in PBS by 20 min incubation at RT. Membranes were stained with CellMask Deep Red (Life Technologies), 1:1000 dilution in PBS by 10 min incubation at RT. Tubulin was either stained with 1:400 alpha-tubulin antibody, Alexa Fluor 488 (ThermoFisher Scientific), at 1:400 dilution in PBS containing 5% BSA, fraction V (AppliChem) by 20 min incubation at RT or with mouse anti-beta-tubulin (Sigma Aldrich), at 1:400 dilution in PBS/BSA for 1 h at RT, followed by goat anti-mouse Alexa Fluor 647 (ThermoFisher Scientific) at the same concentration as the primary antibody, for 1 h at RT.

MCC13

MCC13 cells shown in Figure 3.7 were cultured and stained by Deanna L. Wolfson and Rajwinder Singh. The cells were seeded onto the clean waveguides and incubated for about 12 h at 37 °C. Directly before imaging, they were stained for 30 min with 0.1 M Mito Tracker Deep Red (Thermo Fisher Scientific) and imaged in Live Cell Imaging Solution (Thermo Fisher Scientific).

U2OS

Human bone osteosarcoma (U2OS) cells shown in Figure 3.5e were cultured by Matthias Simonis. Cells were grown in Dulbecco's Modified Eagle Medium (DMEM) (Sigma Aldrich) supplemented with 10% fetal bovine serum (FBS). A humidified CO_2 atmosphere at 37 °C was used for cultivation on the waveguide chips for about 20 h before fixation. For fixation, the medium was aspirated and the cells were fixed for 12 minutes in 0.5% glutaraldehyde (Sigma Aldrich) in cytoskeleton stabilizing buffer pre-warmed to 37 °C that consisted of 80 mM PIPES (Sigma Aldrich), 1 mM Magnesium Chloride (Roth), 5 mM Ethylenediaminetetraacetic acid (EDTA) (Sigma Aldrich) in double-distilled water (ddH_2O) with pH adjusted to 6.9 using an aqueous solution of potassium hydroxide (KOH) (Roth). Cells were washed by extensive rinsing with PBS and permeabilized with 0.1% Triton X-100 (Fluka) in

PBS for 10 minutes at RT. After fixation and permeabilization, cells were washed by extensive rinsing with PBS and autofluorescence was quenched by incubating for 7 minutes with 0.2% w/v sodium borohydride (NaBH4) (Sigma Aldrich) in PBS, rinsed with PBS, incubated for 7 minutes with 1 M Tris-HCl pH 8 (Roth) in ddH_2O, and rinsed again with PBS. Samples were blocked with 5% w/v bovine serum albumin (Sigma Aldrich) in PBS for 45 minutes. Immunostaining was done with primary antibodies against alpha-tubulin raised in mouse (Mouse anti-alpha-tubulin Alexa Fluor 488 (B-5-1-2), Invitrogen) diluted 1:150 from the stock in PBS supplemented with 1.3% BSA, and 0.033% Triton X-100 for approximately 90 minutes. After rinsing with PBS, samples were incubated with Alexa 647-labeled secondary antibodies against mouse raised in goat (Alexa Fluor 647 F(ab') 2 fragment of goat anti-mouse IgG (H+L), Invitrogen) diluted 1:200 from the stock in PBS supplemented with 1% BSA, and 0.025% Triton X-100 and subsequently excessively rinsed with PBS. The cells were additionally post-fixed with 1% v/v formaldehyde (ThermoFisher Scientific) in PBS for 15 minutes and again washed with PBS. Prepared cells were stored in PBS at 4 °C until imaging.

Different preparations

Dye surfaces were prepared by submerging approximately 50 nM Alexa 647 in 0.05% Poly-L-lysine (Sigma Aldrich) and incubating it for approximately 20 min on the waveguide chip.

Multi-colored beads (Invitrogen) were diluted from the stock and prepared on the waveguide chips.

E. coli were grown at 37 °C over night on agar plates before being fixed with 4% PFA and stored in PBS at 4 °C until imaging.

For evanescent field measurements, biotin-coated polystyrene beads of 8.18 µm nominal diameter (Bangs Laboratories) were incubated with streptavidin-conjugated Atto 488, Alexa 488, or Alexa 647 (IBS), washed and pipetted onto the waveguide chips.

Nanorulers

Alexa 647-labeled R50 nanorulers (Gattaquant) were prepared on the waveguide by subsequently placing a PDMS chamber on the surface, washing it thrice with PBS, incubating it with 0. mg/ml BSA-biotin (Sigma Aldrich) in PBS for 5 min, incubating it with 0.5 mg/ml Neutravidin (VWR) in PBS for 5 min, and incubating

it with 0.5 µl R50 stock solution in 10 µl 60 mM Magnesium chloride in PBS for 5 min. Each step beginning from the BSA-biotin incubation was followed by two or three times washing with 60 mM Magnesium chloride ($MgCl_2$) in PBS.

A.2.2. Inverted setup EM-CCD imaging

Nanorulers

Alexa 647-labeled R50 nanorulers (Gattaquant) were prepared on a coverglass (# 1.5) (Thermo Fisher Scientific Gerhard Menzel) by placing a PDMS chamber on the surface, washing it thrice with PBS, incubating it with 5 mg/ml BSA-biotin (Sigma Aldrich) in PBS for 5 min, washing it thrice with in PBS, incubating it with 0.5 mg/ml Neutravidin (Thermo Fisher Scientific) in PBS for 10 min, and incubating it with 2.5 µl R50 stock solution in 25 µl 10 mM Magnesium chloride in PBS for 1 h. Each step beginning from the Neutravidin incubation was followed by three times washing with 10 mM Magnesium chloride in PBS.

Fluorescent beads

For measurements of the achievable localization precision using high and low NA objective lenses on the inverted conventional setup, 200 nm TetraSpeck Microspheres (Thermo Fisher Scientific) were diluted at approximately 1:50 in Vectashield H-1000 (Vector Laboratories).

A.2.3. Optically trapped sampled imaging

Microspheres

The streptavidin-coated surface of superparamagnetic microspheres (CM01N, Bangs Laboratories) with a nominal mean diameter of 8.18 µm was labeled with Alexa 647 bound to a single-stranded, 10 nucleobases long DNA strand functionalized with biotin (IBA). 4 µL of bead stock solution and 8 µL of 10^{-6} M solution of the labels were added to 400 µL ddH_2O containing 0.01% (v/v) Tween20 and vortexed at approximately 1000 rpm at room temperature for approximately 30 minutes. Subsequently, the beads were pulled to the bottom of the reaction tube by a permanent magnet and washed three times with ddH_2O containing 0.01% (v/v) Tween20 to remove unwanted residuals. After the last washing step the tube was filled with 170 µL of PBS supplemented with 0.15% (w/v) BSA (Sigma Aldrich).

Of this, 40 µL were mixed with 55 µL imaging buffer, and 60 µL of the final solution were applied to a sealed chamber and used for the experiments.

E. coli

E. coli samples were prepared by Christoph Spahn. The *E. coli* strain MG1655 was inoculated from glycerol stocks and grown over night (ON) in LB medium (Sigma) at 32 °C while shaking at 200 rpm. Working cultures were inoculated 1:200 in LB medium from ON. 10 µM EdU (Baseclick) were added for 40 minutes at an OD_{600} of about 0.25 to cover the time needed for one complete replication round. After fixation with 1% formaldehyde in phosphate buffer, cells were centrifuged at 5000 × g for 5 minutes and washed twice in 100 mM phosphate buffer of pH 7.4. The click-reaction was performed as described in [192]. Cells were washed thrice with PBS (Sigma), centrifuged, and kept as stock solution. A volume of 20 µL of 20% (v/v) of the *E. coli* stock solution in PBS was was mixed with 55 µL imaging buffer, and 60 µL of the final solution were applied to a sealed chamber and used for the experiments.

A.2.4. Inverted setup (s)CMOS imaging

Fluorescent beads

Sub-diffraction sized fluorescent Tetraspeck beads of 100 nm (ThermoFisher Scientific) were diluted at 1:40000 from the stock into phosphate buffered saline (PBS) (Sigma Aldrich) and dried at room temperature (RT) in a Nunc Lab-Tek II chambered # 1.5 coverslip (ThermoFisher Scientific). Before imaging, the chamber was filled with ddH_2O.

U2OS

U2OS cells were cultured by Matthias Simonis. Cells were grown in DMEM (Sigma Aldrich) supplemented with 10% FBS. A humidified CO_2 atmosphere at 37 °C was used for cultivation on Nunc Lab-Tek II chambered # 1.5 coverslips for about 24 h before fixation. For fixation, the medium was aspirated and the cells were fixed for 20 minutes in 0.5% glutaraldehyde (Sigma Aldrich) in cytoskeleton stabilizing buffer pre-warmed to 37 °C that consisted of 80 mM PIPES (Sigma Aldrich), 1 mM Magnesium Chloride (Roth), 5 mM EDTA (Sigma Aldrich) in ddH_2O with pH adjusted to 6.9 using an aqueous solution of KOH (Roth). Cells were washed 3 times

with PBS and permeabilized with 0.1% Triton X-100 (Fluka) in PBS for 10 minutes at RT. After fixation and permeabilization, cells were washed three times with PBS and autofluorescence was quenched by incubating for 7 minutes with 0.2% w/v NaBH4 (Sigma Aldrich) in ddH_2O, washed three times with PBS, incubated for 7 minutes with 50 mM Tris-HCl pH 8 (Roth) in ddH_2O, and washed again three times with PBS. Samples were blocked with 5% w/v bovine serum albumin (BSA) (Sigma Aldrich) in PBS for 45 minutes. Immunostaining was done with primary antibodies against alpha-tubulin raised in mouse (Mouse anti-alpha-tubulin Alexa Fluor 488 (B-5-1-2), Invitrogen) diluted 1:200 from the stock in PBS supplemented with 1% BSA, and 0.025% Triton X-100 for approximately 100 minutes. After washing three times with PBS, samples were incubated with Alexa 647-labeled secondary antibodies against mouse raised in goat (Alexa Fluor 647 F(ab') 2 fragment of goat anti-mouse IgG (H+L), Invitrogen) diluted 1:200 from the stock in PBS supplemented with 1% BSA, and 0.025% Triton X-100 for approximately 100 minutes and subsequently excessively washed with PBS. The cells were additionally post-fixed with 1% v/v formaldehyde (ThermoFisher Scientific) in PBS for 5 minutes and again washed with PBS. Prepared cells were stored in PBS at 4 °C until imaging.

LSEC

The LSEC samples imaged with the cost-efficient multi-color setup were prepared by Hong Mao in collaboration with Glen Lockwood. The LSECs were isolated and purified from Sprague Dawley male rats as described in [189] and plated on fibronectin-coated coverslips for 3 h in RPMI-1640. Fixation was done with 4% PFA in PBS supplemented with 0.02 M sucrose, pH 7.2 for 15 min. Cells were washed and stained with DiD diluted 1:200 from the stock.

A.3. Imaging buffer

A.3.1. Enzymatic oxygen removal via GODCAT

For most experiments, an enzymatic system based on glucose oxidase and catalase (GODCAT) was applied for oxygen depletion [57]. An enzyme stock solution (ES) was prepared at 0.1 kU/mL glucose oxidase (Sigma Aldrich), 1.2 kU/mL catalase (Sigma Aldrich), 4 mM tris(2-carboxyethyl)phosphine (TCEP) (Sigma Aldrich), 25 mM potassium chloride (KCl) (Acros Organics), 20 mM Tris-HCl pH 7.5, and

50% v/v glycerol (Riedel-de Haen) in ddH_2O or D_2O. A glucose stock solution (GS) was prepared at 10% w/v glucose (Sigma Aldrich), and 10% glycerol in ddH_2O or D_2O. ES and GS were stored in aliquots at −20 °C.

If enzymatic oxygen via GODCAT was desired, the imaging buffer contained 40% GS and 5% ES.

A.3.2. Waveguide imaging

dSTORM and ESI

Imaging buffer for *d*STORM experiments was prepared from H_2O-based GODCAT components and PBS. The buffer was supplemented with 2 mM cyclooctatetraene (COT) (Sigma Aldrich) in case of Alexa 647 imaging and with different concentrations of Mercaptoethylamine (MEA) (Sigma Aldrich). An MEA concentration of 95 mM was used in case of CellMask Deep Red and Atto 488 imaging. In case of all Alexa 647 imaging experiments on the waveguide, the MEA concentration was 20 mM. Sub-diffraction sized, fluorescent 100 nm TetraSpeck Microspheres (Life Technologies) at a low concentration (approximately 1:5000 from stock) optionally aided algorithmic drift correction of the super-resolved images.

Diffraction limited imaging

For diffraction limited imaging, a reducing and oxidizing buffer system (ROXS) was used [209]. The buffer comprised of ddH_2O-based 40% GS, ddH_2O-based 5% ES in ddH_2O supplemented with 50 mM Tris-HCl pH 8, 50 mM NaCl, 2 mM ascorbic acid (Fluka), and 2 mM methyl viologen (Sigma Aldrich).

Objective-based TIRF dSTORM imaging

The buffer for Alexa 647-labeled DNA nanorulers on the conventional inverted microscope was prepared from D_2O-based GODCAT components, supplemented with 45 mM Tris, and contained MEA at a concentration of 10 mM. Sub-diffraction sized, fluorescent 100 nm TetraSpeck Microspheres (Life Technologies) at a low concentration (approximately 1:5000 from stock) aided algorithmic drift correction of the nanoruler images.

A.3.3. Optically trapped samples dSTORM imaging

The buffer for the *d*STORM experiments was prepared from ddH_2O-based GODCAT components in PBS supplemented with 100 mM MEA.

A.3.4. Inverted setup (s)CMOS dSTORM imaging

The buffer for the *d*STORM experiments on U2OS cells was prepared from ddH_2O-based GODCAT components in ddH_2O-based supplemented with 50 mM Tris-HCl pH 8, 50 mM NaCl, 2 mM COT, and 143 mM or 100 mM MEA.

A.4. Image acquisition and data analysis

A.4.1. Waveguide imaging

Image data acquisition

Several hundred frames were acquired at relatively low power at the input facet for waveguide-based imaging. During acquisition, the coupling objective lens was oscillated along the input facet. These image stacks were used as input for the ESI reconstruction. Alternatively, averaging over the acquired frames yields a diffraction-limited image of the sample. Single frame exposure times for dSTORM ranged from 10 ms to 160.84 ms.

Objective-based TIRF dSTORM for comparison

*d*STORM imaging of nanorulers was performed in TIRF mode on the inverted microscope equipped with an EM-CCD camera. The excitation intensity using the 647 nm laser line was approximately 5.5 $\frac{\mathrm{kW}}{\mathrm{cm}^2}$ and the 488 nm laser line was used for photoswitching. The single frame exposure time was 50 ms, the detector temperature was −70 °C, and the EM-CCD gain setting was 200.

Image data reconstruction and analysis

Image processing and analysis was carried out using Fiji and Matlab (Mathworks). ESI reconstruction and postprocessing was performed using the Fiji plugin ESI [222]. Reconstructions were run in two iterations at second ESI order with an intermediate gamma correction step using a gamma factor of 0.5 to compensate for non-linear

intensity amplification. For *d*STORM reconstruction and postprocessing the Fiji plugin ThunderSTORM [149] was used. Localizations were filtered for unphysical values of fitted FWHM width and localization precision. Non-linear drift correction was performed via cross-correlation of substacks. *d*STORM images were rendered using the "Average shifted histograms"-option and convolved with a 2D Gaussian kernel of 10 nm to 68.5 nm in some cases. The look up tables and intensity values for shown figures were adjusted to achieve appropriate contrast including gamma correction, however all quantifications were made on linearly scaled images. Custom written Matlab code was used for localization precision measurements by the nearest neighbors approach. FRC analysis was carried out using the Fiji plugin FRC [143]. Diffraction limited images were computed by averaging over all acquired frames recorded prior to *d*STORM imaging or the raw data also used as input for the ESI reconstruction.

Evanescent field intensities

Evanescent field intensities on the waveguide were measured to estimate the sample excitation intensity as well as the coupling efficiency. Single fluorescent, subdiffraction sized 100 µm TetraSpeck Microspheres (Life Technologies) served as intensity sensors. A reference measurement was conducted by imaging the microspheres on a conventional inverted setup in epi-illumination mode. The photon response as a function of the illumination intensity was recorded and corrected for multiple factors including laser power, camera quantum efficiency, single-frame exposure time, the Gaussian-like beam profile in epi-illumination, and the waveguide width in waveguide illumination. Similar measurements were carried out on the waveguide to find the photon response as a function of the power at the input facet of the waveguide and estimate the corresponding evanescent field intensity. Though several factors have been corrected for, these numbers should only be taken as a rough estimation as the efficiency of coupling light into the waveguide differs between different chips.

Evanescent field decay

The height-dependent evanescent field intensity was measured following the approach of [133, 194]. Custom written Matlab code was used to find the center of the beads, perform a transformation to polar coordinates around the center and average over all angles. The height over the waveguide was calculated from the

radial coordinate assumed a perfect sphere and the resulting data was fit by an exponentially decaying curve.

A.4.2. Optically trapped samples imaging

dSTORM imaging

*d*STORM imaging of optically trapped samples was performed in HILO mode, resulting in laser excitation intensities of approximately 5 $\frac{\mathrm{kW}}{\mathrm{cm}^2}$ at the sample. The 647 nm laser line was used for the excitation Alexa 647, while the 488 nm laser line was used for reversible photoswitching by recovery of the fluorescent singlet state.

For the microsphere imaging, approximately 1 500 frames to 12 000 frames were acquired at an exposure time of 29.55 ms per frame, with a detector temperature of −70 °C and an EM-CCD gain setting of 200. Because many measurements of the same sample were conducted in short succession, the number of frames necessary to achieve a sufficient number of localizations increased for later acquired data due to photobleaching. Hence, the acquisition time for these images ranges from approximately 50 s to 400 s.

In the *E. coli* measurements, 8 000 frames to 66 000 frames frames were acquired with an exposure time of 4.64 ms to 8.24 ms, a detector temperature of −70 °C, and an EM-CCD gain setting of 200. Again, successive measurements of the same sample result in an increased number of frames for the second acquisition. The according acquisition times range from about 90 s for the parallel alignment relative to the focal plane and up to 650 s for the orthogonal alignment. For data acquisition, the software (Solis, Version 4.18, Andor) provided by the camera manufacturer was used.

White light imaging

White light image stacks were recorded before or after *d*STORM data acquisition, illuminating with the IX-71 white light source. These consist of approximately 1, 500 frames to 10, 000 frames with a camera exposure time of 4.64 ms to 29.55 ms per frame. In order to achieve a higher contrast for the automated position detection used to determine the PDF, the bacteria were slightly displaced (approximately 700 nm) along the axial direction relative to the imaging plane by adjusting the axial position of the optical traps. The positions of the traps relative to each other were not changed and no significant changes in the movement of the bacteria were

observed. For data acquisition, the software (Solis, Version 4.18, Andor) provided by the camera manufacturer was used.

dSTORM data reconstruction and analysis

The software *rapid*STORM [219](Version 3.2 and Version 3.3) was used for single emitter fitting of the raw *d*STORM data. The output files containing the detected emitters' coordinates were used as inputs for a custom-written MATLAB program to generate image files with adjustable pixel size and pixel values directly proportional to the number of detected single emitters by using linear interpolation. All reconstructions of *E. coli* cells used a pixel size of 25 nm × 25 nm, while all *d*STORM reconstructions of microspheres used a pixel size of 50 nm × 50 nm.

Further analysis and processing was done either directly in MATLAB (Mathworks) or in the open-source software Fiji. The color tables for displaying the images were chosen such that appropriate contrast was achieved and all color bars were linearly scaled in terms of localization density, i.e. localizations per pixel. In the case of *E. coli* bacteria attached to the coverslip, MATLAB code custom written by Alex Weiß was used for automated drift correction [136].

To automatically measure the average FWHM of the edges of the trapped beads, custom-written MATLAB code was used: The center of the bead was first determined algorithmically, followed by a transformation to polar coordinates around the center and an averaging step over all angles. The FWHM of the edge was computed by fitting a Gaussian function to the average radial profile of the individual emitter localizations.

PDF generation and image deconvolution

To obtain the position distribution function of a trapped object, the position was detected in multiple transmitted light image frames using a custom-written MATLAB script based on a center of mass algorithm [26]: Thresholding was applied to slightly smoothed images to create a filtering mask, which was overlaid with the raw image data. The center of mass of the region inside the mask was computed according either to the pixel values in a normalized, background-subtracted image or a binary image to obtain the object's position. A two-dimensional histogram was generated from all detected positions in one image stack. An elliptical, two-dimensional Gaussian function was fitted to this deviation. The function was normalized and stored in an image file as PDF. The PDF pixel size was chosen to

match the pixel size of the *d*STORM image for which it was used during the subsequent deconvolution process, which was performed using the Richardson-Lucy algorithm implementation of the ImageJ/Fiji plug-in DeconvolutionLab [211].

Estimation of optical trap power

The power of the individual optical traps was controlled in two ways: The global power provided by the SLM was determined by adjusting the neutral density filter wheel and measuring the power reflected from the active SLM area. Additionally, the 0^{th} diffraction order (i.e. the unmodulated part of the beam) was used as a power sink to effectively decrease the power of the holographic traps that were always created in locations different from the 0^{th} diffraction order.

To estimate the individual trap powers, a reference measurement was conducted by placing a small aperture in the focal plane behind the first lens of the 4f-telescope which was conjugate to the sample plane. This aperture was adjusted to block all IR laser light from the SLM except for one optical trap. The corresponding optical power of this single optical trap was measured by placing the sensor of a power meter at the position of the objective lens. Measurements were conducted for 45 different values of the relative sink power of the 0^{th} diffraction order in combination with an overall number of one, two, three, or four holographically created optical traps, as no more than four optical traps were simultaneously used throughout this work. From this table of 45 measured trap power values for each overall number of either one, two, three, or four of the holographic optical traps, a cubic spline interpolation was used to estimate the effective single optical trap power for the sink power settings used in the according experiments.

A.4.3. (s)CMOS camera characterization and imaging

Chip characteristics

The camera chip characterization was performed following the approach of Huang et al. [99] for a ROI of 512 × 512 pixels. For dark pixel offset and read noise measurements, it was ensured that the chip was in darkness during the acquisition of 4 000 frames to 8 192 frames. From this data, the baseline for each pixel was determined by the mean value and the read noise by the standard deviation over all frames. A sequence of 15 to 20 (CMOS 1: 15, CMOS 2: 16, CMOS 3: 17, sCMOS: 20) similar measurements with illumination on the chip at different light levels up to approximately 1 000 counts per pixel and per 25 ms exposure time

allowed to determine the variance per mean signal for each pixel. This was calculated via linear regression on the variance as a function of the mean signal. For temperature dependent baseline and noise measurements, the temperature of the camera metal housing was measured in intervals of 40 s and the mean pixel values as well as noise were calculated from 200 frames taken in this period.

dSTORM data acquisition

*d*STORM raw data of U2OS cells was acquired at 4.5 $\frac{\text{kW}}{\text{cm}^2}$ to 6.3 $\frac{\text{kW}}{\text{cm}^2}$ or 33 $\frac{\text{kW}}{\text{cm}^2}$ to 180 $\frac{\text{kW}}{\text{cm}^2}$ illumination intensity using the 639 nm laser for fluorescence excitation in TIRF mode. In some cases, the 405 nm laser was used for additional photoactivation in TIRF mode while the intensity was manually adjusted for each measurement but peak intensities did not exceed 0.02 $\frac{\text{kW}}{\text{cm}^2}$. Diffraction limited images were acquired prior to *d*STORM acquisition. Raw frames were recorded at frame rates of 40 fps or 894 fps, corresponding to single frame exposure times of approximately 25 ms and 1 ms, respectively.

*d*STORM raw data of LSEC cells was acquired on the cost-efficient multicolor setup by Hong Mao. The illumination intensity was about 0.08 $\frac{\text{kW}}{\text{cm}^2}$ from the 647 nm laser in TIRF mode and 40,000 raw frames were recorded.

dSTORM data reconstruction and analysis

The raw data was imported into Fiji and *d*STORM reconstructions were run using ThunderSTORM [149] on its default settings. The localizations were filtered and the super-resolved reconstruction of the tubulin images was rendered at pixel sizes of approximately 5.5 nm width and height using the "Normalized Gaussian"-option, i.e. each localization was smoothed individually with a Gaussian function of which the standard deviation corresponded to the localization precision as estimated by ThunderSTORM based on the signal statistics. For the comparisons between the CMOS and the sCMOS camera, the same post-processing steps were used. The data was filtered for localization precision values less than 15 nm and the drift was corrected via the build in cross-correlation function on substacks [136] with 5 temporal bins.

For reconstruction of raw data of tubulin in U2OS cells recorded with the CMOS camera only, the initial point spread function sigma value was set to 1.2 pixels, different from the default setting of 1.6 pixels. In this case, postprocessing consisted of filtering for localization precision values less than 10 nm or 15 nm, cor-

recting drift as described above with 4 temporal bins, filtering for localizations that featured at least 100 neighbors within a spatial radius of 40 nm or 100 nm and optional merging of localizations in subsequent frames within a spatial radius of 20 nm while a temporal delay of 1 frame was allowed. Image analysis was carried out using basic Fiji functions, custom written Matlab code for nearest neighbor analysis, and the FRC plugin [143] for Fiji.

The LSEC data was reconstructed using ThunderSTORM with the initial point spread function sigma value set to 1.2 pixels. Postprocessing consisted of filtering for PSF sigma values less than 160 nm, localization precision values greater than 6 nm and less than 20 nm, and drift correction as described above with 10 temporal bins. The "Average shifted histograms" option was used for rendering at pixel widths and heights of approximately 16 nm and the reconstruction was additionally convolved with a Gaussian kernel with a sigma value of 10 nm.

B. Acronyms

ADU	Analog-to-digital units
AOTF	Acousto-optical tunable filter
BME	β-mercaptoethanol
BP	Band-pass
BSA	Bovine serum albumin
CCD	Charge coupled device
CMOS	Complementary metal-oxide semiconductor
COT	Cyclooctatetraene
CPU	Central processing unit
DNA	Deoxyribonucleic acid
***d*STORM**	*direct* stochastic optical reconstruction microscopy
EM-CCD	Electron multiplying charge coupled device
ES	Enzyme stock
ESI	Entropy-based super-resolution imaging
FOV	Field-of-view
FRC	Fourier ring correlation
FWHM	Full-width-at-half-maximum
GODCAT	Glucose oxidase/catalase
GPU	Graphics processing unit
GS	Glucose stock
HIDE	High-density, environment sensitive
HILO	Highly inclined and laminated optical sheet
HIV	Human immunodeficiency virus
HOMO	Highest occupied molecular orbital
IR	Infrared
LC	Liquid crystal
LP	Long-pass
LSEC	Liver sinusoidal endothelial cell
LUMO	Lowest unoccupied molecular orbital
MEA	β-mercaptoethylamine

NA	Numerical aperture
ND	Neutral density
OTF	Optical transfer function
PAINT	Points accumulation for imaging in nanoscale topography
PALM	Photo-activated localization microscopy
PBS	Phosphate-buffered saline
PDF	Position distribution function
PDMS	Polydimethylsiloxane
PPD	Probability distribution on pair-wise distances
PSF	Point spread function
RESOLFT	Reversible saturable/switchable optical linear fluorescence transitions
ROI	Region of interest
sCMOS	Scientific-grade complementary metal-oxide semiconductor
SIM	Structured illumination microscopy
SLM	Spatial light modulator
SMLM	Single molecule localization microscopy
SNR	Signal-to-noise ratio
SOFI	Super-resolution optical fluctuation imaging
STED	Stimulated emission depletion
STORM	Stochastic optical reconstruction microscopy
TIRF	Total internal reflection fluorescence
UV	Ultraviolet

C. Publications

This work is based in major parts on the following peer-reviewed publications:

R. Diekmann, D.L. Wolfson, C. Spahn, M. Heilemann, M. Schüttpelz, and T. Huser. Nanoscopy of bacterial cells immobilized by holographic optical tweezers. *Nature Communications*, **7**:13711, 2016.

Author contributions: R.D. and D.L.W. built the setup. R.D. performed the experiments. R.D. and M.Sch. analyzed data. 3D-SIM imaging and data analysis was done by D.L.W. C.S. and M.H. developed the bacterial cell samples. R.D., M.Sch. and T.H. conceived the concept, designed the experiments and wrote the paper.

R. Diekmann*, Ø.I. Helle*, C.I. Øie, P. McCourt, T. Huser, M. Schüttpelz, and B.S. Ahluwalia. Chip-based wide field-of-view nanoscopy. *Nature Photonics*, **11**(5):322–328, 2017.

(* equal contribution)

Author contributions: B.S.A. and M.Sch. conceived the project. All authors designed the research. C.I.Ø. isolated the cells, and stained and prepared the biological samples. R.D. and Ø.I.H. built the setup, prepared the non-biological samples, performed the experiments, performed the simulations, reconstructed the images, analyzed the data, and created the figures. R.D., Ø.I.H., M.Sch., and B.S.A. mainly wrote the paper. All authors reviewed the manuscript.

R. Diekmann, K. Till, M. Müller, M. Simonis, M. Schüttpelz, and T. Huser. Characterization of an industry-grade CMOS camera well suited for single molecule localization microscopy – high performance super-resolution at low cost. *Scientific Reports*, in print, 2017.

Author contributions: R.D., M.Sch. and T.H. designed the research. R.D. and K.T. built the optical setup, prepared the samples, conducted the experiments and prepared the figures. M.M. adapted the camera device adapter for Micro Manager. M.Si. cultured the cells. R.D. analyzed the data and wrote the manuscript. All authors reviewed the manuscript.

D. Acknowledgements

This work would not have been possible without so many people supporting me over the last years.

First of all, I would like to thank my supervisor Prof. Thomas Huser for giving me the opportunity to work in the exciting field of Biomolecular Photonics and for always leaving me the freedom to follow my own ideas.

Many thanks to Prof. Andreas Hütten for taking over the part of the second referee and also to Prof. Dario Anselmetti and Prof. Nicolas Borghini for completing the PhD committee.

Mark Schüttpelz, you have been a great support since my tentative steps in the optics lab back in 2012. Together, we have not only been constant visitors in the land of the midnight sun, but also been the major drivers in establishing waveguide-based microscopy in Bielefeld.

Of course, the waveguide project would not have been possible without Team Tromsø. For the great collaboration and countless nights in the lab, I would like to express my gratitude to Øystein Helle. Blobby Volley and Eurodance music have helped us through many imaging sessions of which some finally made it into this thesis.

Further thanks to Balpreet Singh Ahluwalia for being a great collaborator in this project and giving me the opportunity to work in the artic for several months.

Cristina Øie has prepared a lot of samples on the waveguides and together with Peter McCourt contributed the biology that made the waveguide project a success.

A lot of thanks to Deanna Wolfson for working on holographic optical trapping together and later continuing our collaboration as a part of the Tromsø group.

I owe thanks to Peter for inviting me to Sydney and together with Gunbjørg for being great hosts in Petersham as well as to Victoria Cogger and David Le Couteur for hosting us at the ANZAC institute.

For the hard work on the multi-color setup, for sharing his LSEC *d*STORM data, and for the interchange of knowledge about liver cells, *d*STORM, and also less work-related stuff, I thank Hong Mao.

Katharina Till has been a great colleague in general and in particular in the camera project, to which also Marcel Müller and Matthias Simonis have contributed their parts. Thanks to all of you.

For additional cell preparations in different projects, I thank Rajwinder Singh, Ida Opstad, Deanna Wolfson, Alice Wilking, and Gabriel Wang.

Christoph Spahn and Mike Heilemann have kindly contributed the bacteria to the optical trapping project.

Thanks to Arash Ahmadi for bringing another great application of the optical trapping setup to Bielefeld, and for many looong imaging sessions waiting for the proteins to arrive.

For the advice on SLM-related topics and programming the great software for the holographic optical tweezers, I thank Mattias Goksör, Martin Persson and Michael Steck.

Thanks to Anders Engdahl for joining me in the later stage of the waveguide project and realizing the speckler.

Kevin Diekmann, Mark Schüttpelz and Stephan Bergmann have suffered lots of typos and more when proofreading this thesis.

One of the most important persons on the science-related list is Gerd Wiebusch. Thank you for the patient support on all optics related problems.

For the help with organizational matters and further support, I thank Reinhild, Wolfgang and Stephan.

Working in science would not be that fun without great coworkers. For the fun in the lab and on other occasions I thank everyone in Bielefeld, Tromsø and Sydney.

Moving to different offices from time to time, Marcel, Michi, Bo, Bone, Alice and Stephan have given me comfortable company. Further thanks for the nice time in Bielefeld and interesting discussions on various topics to my current and former colleagues Caro, Lena, Anders, Kathi, Paule, Alex, Sebastian, Steffen, Gabriel, Mario, Henning, Christian, Christian, Elina, Simon, Idir and Fabian.

For many science-related activities at UiT and even more non-science-related activities at Sivertsens, I thank the players of Team Tromsø: Øystein, Marcel (you have made it to both lists!), Deanna, Jean-Claude, Firehun, Rajwinder, Ida, David, Martin, Cristina, Peter, Jana, Olaf and, of course, Balpreet.

Hong and Sebastian – we have survived Concord 75.

My final thanks go to my family and Kristina for the neverending support and encouragement during the stressful times of this work and beyond. Thank you!